Decay of electronic excitations at metal surfaces

P.M. Echenique[a,b,*], R. Berndt[c], E.V. Chulkov[a,b], Th. Fauster[d],
A. Goldmann[e], U. Höfer[f]

[a]*Departamento de Física de Materiales and Centro Mixto CSIC-UPV/EHU, Facultad de Ciencias Químicas,
UPV/EHU, Apdo. 1072, 20080 San Sebastián/Donostia, Basque Country, Spain*
[b]*Donostia International Physics Center (DIPC), Paseo de Manuel Lardizabal 4,
20018 San Sebastián/Donostia, Basque Country, Spain*
[c]*Institut für Experimentelle und Angewandte Physik, Christian-Albrechts-Universität zu Kiel,
Olshausenstrasse 40, D-24098 Kiel, Germany*
[d]*Lehrstuhl für Festkörperphysik, Friedrich-Alexander-Universität Erlangen-Nürnberg,
Staudtstrasse 7, D-91058 Erlangen, Germany*
[e]*Experimentalphysik II, Fachbereich Physik, Universität Kassel, Heinrich-Plett-Strasse 40, D-34132 Kassel, Germany*
[f]*Fachbereich Physik und Zentrum für Materialwissenschaften, Philipps-Universität,
Renthof 5, D-35032 Marburg, Germany*

Abstract

Recent experimental work has reached an accurate determination of surface-state linewidth by scanning tunneling spectroscopy, photoemission and directly in the time domain by two-photon photoemission. The concomitant progress in the theoretical description of surface-state decay has led to an excellent agreement between theory and experiment for low-index noble-metal surfaces. The understanding of the behavior of s–p-like surface states and image-potential states on these surfaces constitutes the basis for the application to more complicated systems.
© 2004 Elsevier B.V. All rights reserved.

Contents

* Corresponding author. Tel.: +34-943-01-59-63; fax: +34-943-01-56-00.
E-mail address: wapetlap@sq.ehu.es (P.M. Echenique).

1. Introduction

Excited electrons play an essential role in many processes, e.g. in the conversion of light to chemical energy in photosynthesis or to electrical energy in a solar cell. These processes rely on a sufficiently long lifetime of the electronic excitation, so the charge can be transferred and used for the intended purpose. Scattering of the excited electron by other electrons, vibrations (phonons) or defects may cause a loss of energy or a change of direction. The desired charge transfer then will not occur and the primary excitation energy will be dissipated as heat.

Due to the high density of valence electrons the lifetime of electronic excitations in metals is very short, i.e. in the femtosecond range, and useful applications seem out of reach. At metal interfaces the situation is different, because the transfer of the excited electron across the interface, e.g. to or from a molecular or semiconductor layer is of interest for photochemistry and for chemical reactions in general as well as for electronic devices [1–3]. From a fundamental point of view, it is therefore worthwhile to study the decay of electronic excitations at metal surfaces. The dynamical behavior of surface states at single-crystal metal surfaces deserves particular attention. Tremendous progress has been made in recent years in this field using a variety of theoretical and experimental methods. The achieved results are the topic of this review.

The excited particle, which might be an electron or hole in a surface state, may undergo three different types of scattering processes:

- *Electron–electron scattering*. This is the most important process for energy relaxation leading to decay into bulk or surface states at lower energy with the simultaneous creation of an electron–hole pair.
- *Electron–phonon scattering*. Phonons provide mainly momentum and little energy. This scattering process therefore changes mainly the direction of the electron motion, which includes scattering to bulk bands as well as scattering within the surface state band.
- *Electron–defect scattering*. Real surfaces are not perfect and contain always a non-negligible amount of defects, such as steps or impurity atoms. The associated electron–defect scattering changes the electron momentum and is predominantly elastic. In some aspects it resembles electron–phonon scattering, if we regard a phonon as a distortion of the ideal lattice. The situation may be modified, if the defect provides additional electronic states serving as new electron–electron scattering channels or the possibility to loose energy to molecular vibrations.

The latter two processes may be identified experimentally by a systematic variation of the number of phonons through temperature or the concentration of defects through sample preparation. Extrapolation to zero temperature and to zero defect concentration allows to estimate the remaining many-particle effect of electron–electron scattering.

At metal surfaces there exist in addition to bulk bands specific electronic states which can be classified as intrinsic surface states and image-potential states. The latter arise for an additional electron in front of the surface. The screening of the charge by the metal electrons gives rise to the long-range image potential which leads—similar to the case of the hydrogen atom—to an infinite series (numbered by n) of bound states in the presence of a band gap in the projected bulk band structure [4–8]. The maximum of the probability density for the first image-potential state is several Angstroms away from the surface and increases quadratically with the quantum number n. Intrinsic surface states on the other hand have their maximum close to the surface and are often classified according to the authors of the respective original models as Tamm [9,10] and Shockley [11] states. Even though the distinction is not clear in all cases, more localized surface states are usually called Tamm states, whereas Shockley states show a strong free-electron-like dispersion [12]. The different types of surface states allow to study the effect of weak or strong coupling to the underlying bulk bands. Surface and image-potential states are modified by adlayers (of metals, noble gases or molecules) on the surface leading to overlayer or quantum well states. New adsorbate states may also be introduced by the adsorbate layers, but these will only be mentioned briefly in this review.

Fig. 1 illustrates intrinsic surface states and image-potential states in the gap of the projected bulk band structure for Cu(1 1 1) and Cu(1 0 0). The relevant scattering processes are indicated for an electron in the image-potential state and for a hole in the surface state. Note that in the electron–electron scattering process an electron–hole pair is created which takes up energy and momentum. In electron–phonon or electron–defect scattering the phonon or defect, respectively, provides the momentum (and energy). As can be seen in Fig. 1 all scattering processes are possible for holes as well as electrons. Looking at the electron scattered into the hole, we retain the notation of electron scattering for simplicity.

A successful study of the decay of electronic excitations in surface states at metals requires appropriate theoretical and experimental methods. The theoretical calculations use different models depending on the interactions relevant for the scattering processes. The decay rate due to inelastic electron–electron scattering is calculated using the GW approximation for the self energy [13–16]. For the electron–phonon interaction the Eliashberg function is used [17–19]. The scattering by defects has
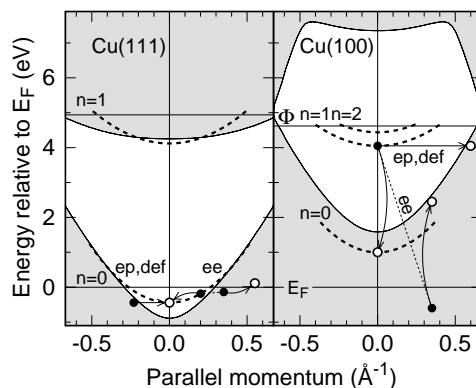

Fig. 1. Schematic projected bulk band structure (shaded areas) for the Cu(1 1 1) and Cu(1 0 0) surfaces with intrinsic surface-state bands ($n = 0$) and image-potential bands ($n \geq 1$). Arrows indicate possible electron–electron (ee), electron–phonon (ep) and defect (def) scattering processes.

been treated only for the elastic case by a wave-packet-propagation method [20–23]. Three different experimental techniques have been employed to study the decay of the electronic states at metal surfaces. Photoelectron spectroscopy (PES) [24–26] accesses the decay rate through the spectral lineshape and linewidth [27]. It is limited to occupied states below the Fermi energy. The complementary method of inverse photoemission permits the spectroscopy of unoccupied surface states and image-potential states [28,29]. However, its limited energy resolution does not allow to extract useful information on linewidths except in favorable cases [30]. Scanning tunneling microscopy (STM) and in particular scanning tunneling spectroscopy (STS) [31–33] obtains detailed information on the decay properties of surface and image-potential states. The topographical images monitor simultaneously the quality and structures of the surface area under investigation. Two-photon photoemission (2PPE) [4,34] in the time-resolved mode is the only technique which is able to study the decay in the time domain [35,36]. By combining this information with spectroscopic measurements a very detailed picture of the electron dynamics emerges.

Table 1 lists the different scattering processes, quasiparticles and types of surface states which can be studied by the various techniques. Each of the techniques has its weaknesses and strengths in addressing specific questions about the electron dynamics at metal surfaces. Photoelectron spectroscopy can access only occupied states and is therefore restricted to the hole decay. Two-photon photoemission is most successful for measuring image-potential states and the application to other states is limited. The scanning tunneling methods work particularly well for Shockley-type surface states. There is no closed theoretical description of all scattering processes, but for each problem appropriate models have been worked out successfully. As illustrated in Table 1 the various methods can tackle almost all the involved problems. It is the aim of this review to combine the available results into a consistent and rather complete picture of the decay of electronic excitations at metal surfaces.

At first we will outline the theoretical ingredients to describe the electron–electron and electron–phonon scattering processes. Electron–defect scattering has been addressed only recently with a wave-packet-propagation method. This will be mentioned briefly in the discussion and we refer the reader to the literature [20–23,37]. The analysis and the results of the experimental methods are the subject of the following chapters. Photoelectron spectroscopy is the most mature technique and the current state of the art with respect to the lineshape analysis of surface states is presented in Section 3. Scanning tunneling

Table 1
Scattering processes, quasiparticles and surface states which can be studied with the various methods (PES: photoelectron spectroscopy, STM: scanning tunneling microscopy, 2PPE: two-photon photoemission) presented in this review

	Theory	PES	STM	2PPE
Scattering processes				
Electron–electron	X	X	X	X
Electron–phonon	X	X	X	X
Electron–defect	X	X	X	X
Quasiparticles				
Electrons	X	–	X	X
Holes	X	X	X	X
Surface states				
Intrinsic	X	X	X	X
Image-potential	X	–	X	X
Quantum well	X	X	X	X

microscopy and spectroscopy (Section 4) provides a perspective of surface states on areas at the atomic scale. The decay of electronic states can be studied on the femtosecond timescale by two-photon photoemission. The results presented in Section 5 concentrate on image-potential states. Section 6 brings the information of the theoretical and experimental chapters together. It presents an impressive agreement between the results of the different techniques and provides a deep insight into the decay of electronic excitations at metal surfaces.

2. Theoretical description

2.1. Introduction

The physics of electron dynamics in image-potential and surface states (as well as in bulk states) can be qualitatively understood in terms of a few key ingredients such as initial and final states, density of final states as well as electron–electron and electron–phonon screened interaction. In particular, the linewidth gets wider with: (i) a larger overlap between initial and final states, (ii) more states at the energy of the final states (density of states (DOS) factor), (iii) a larger imaginary part of the screened interaction and the associated weaker screening and (iv) an increased electron–phonon coupling.

The use of 3D wave functions in evaluations of the electron (hole) decay leads to time-consuming 3D calculations of the electron–electron coupling matrix elements of the screened electron–electron interaction. In addition, in calculations involving image-potential states a calculation scheme is needed that, in principle, reproduces the image-potential tail at the surface.

The classical image potential is the interaction energy of a distinguishable test charge located in the neighborhood of a surface with the polarization charge it induces at the surface. It assumes a local response function and therefore that the induced charge density is located at the surface plane itself. More sophisticated models for the response of the surface have been proposed leading to a spread of the induced charge density and to an asymptotic form of the image potential [38]:

$$V(z) = -\frac{1}{4(z - z_{im})}, \tag{1}$$

where z_{im} is the static image-plane position. Dynamical corrections to the image potential were found to be small for the range of momenta that are relevant to this review [39,40]. The fact that the electron creating the image potential is localized by the image potential itself has been studied within the self-energy formalism [41,42].

When the test charge is an electron it is necessary to take also into account exchange and correlation interactions. White et al. [43] showed that for an electron trapped in an image-potential state the image potential is created by long-range correlation interactions. They did a self-energy calculation within the GW approximation [13] for very thin (five atomic layers) Al(1 1 1) films separated by a narrow (eight interlayer spacings) vacuum region. This vacuum space is good enough for evaluations of surface states (provided that a thicker film is employed) and probably for the first image-potential resonance. However, this vacuum region is not wide enough for the description of image-potential states located in an energy gap [44,45]. The fully first-principles GW calculations are very time consuming and they become even more problematic for systems consisting of a bigger number of atomic layers and wider vacuum space and for systems with more complicated electronic structure (noble and transition metals).

A calculation of the electron dynamics in real metals using such a potential is not feasible at the moment. A less complicated scheme that has the correct image-potential-like behavior for the exchange-correlation potential has been proposed recently by García-González et al. [46]. Possible influence of the spatio-temporal evolution of an electron–hole pair optically created in the 3D band at a metal surface on electron lifetimes in image-potential states was discussed by Gumhalter [47,48]. Some aspects of electron dynamics in image-potential states were also discussed by Sakaue et al. [49–51] using Green function method and very simple approximations for potentials and dielectric response function.

2.2. One-electron model potential

Because of the reasons quoted above and the large complexity of fully 3D GW calculations with all the ingredients of the electron dynamics at surfaces, Chulkov et al. [44,45] suggested a simplified model that allows for realistic calculations while retaining at the same time the essential physics of electron (and hole) dynamics at surfaces. They assumed that the charge density and one-electron potential is constant in the (x, y)-plane parallel to the surface and varies only in the z-direction perpendicular to the surface. This assumption is valid for image-potential states since their wave functions lie mainly at the vacuum side of the surface and the electron moves, therefore, in a region with little potential variation in a plane parallel to the surface. Moreover, this assumption is still reasonably good for the clear s–p_z surface states on clean metal surfaces [52–56] and surfaces covered with alkali-metal adlayers [57], because these states do not show either a strong variation in the direction parallel to the surface region [58–66].

By construction this (1D) model potential has physically well-motivated behavior everywhere in space. In particular, in the bulk region it is described by a cosine function which opens the energy gap on the surface of interest [67], the position and amplitude of this function is chosen to reproduce the experimentally observed (or obtained from first-principles calculations) energy gap. In the solid–vacuum interface the model potential is represented by a smooth cosine-like function that reproduces the experimental energy of the s–p_z surface state. In the vacuum region this function merges into the long-range image potential in such a way that it describes the experimental binding energy of the first image-potential state. The position of an image plane which is an important characteristic of the image potential is automatically obtained from the defining potential equations [44,45]. The model potential has been constructed for many metal surfaces [45,68] and is used for calculating the hole and electron dynamics in surface and image-potential states (see Section 6). The model potential for the Cu(1 1 1) surface is shown in Fig. 2 together with the squares of the wave functions of the intrinsic surface state ($n = 0$) and the first image-potential state ($n = 1$) at $\bar{\Gamma}(\boldsymbol{k}_\parallel = 0)$.

2.3. Electron–electron interaction

In the framework of many-body theory the damping rate Γ, i.e. inverse lifetime, of an electron with energy $\epsilon_i > E_{\mathrm{F}}$ is obtained on the energy-shell approximation in terms of the imaginary part of the complex non-local self-energy operator [13,16]:

$$\Gamma = \tau^{-1} = -2 \int \mathrm{d}\boldsymbol{r} \int \mathrm{d}\boldsymbol{r}' \phi_i^*(\boldsymbol{r}) \operatorname{Im} \Sigma(\boldsymbol{r}, \boldsymbol{r}', \epsilon_i) \phi_i(\boldsymbol{r}'), \tag{2}$$

where ϕ_i and ϵ_i are the eigenfunctions and eigenvalues of the one-body Hamiltonian.
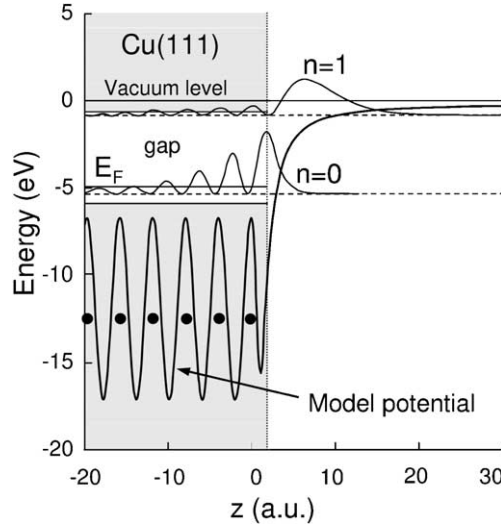
Fig. 2. 1D model potential and probability density for the intrinsic surface state ($n = 0$) and the first image-potential state ($n = 1$) at the Cu(1 1 1) surface at $\bar{\Gamma}$. The shaded areas indicate the projected bulk bands bounded by the image plane. The dots give the positions of the atomic planes.

The imaginary part of the self energy is evaluated in the so-called GW approximation, in terms of the screened interaction and the allowed final states for the decay process:

$$\mathrm{Im}\,\Sigma(\boldsymbol{r},\boldsymbol{r}',\epsilon_i > E_{\mathrm{F}}) = \sum_f {}' \phi_f^*(\boldsymbol{r}')\,\mathrm{Im}\,W(\boldsymbol{r},\boldsymbol{r}',\omega)\phi_f(\boldsymbol{r}). \tag{3}$$

Here $\omega = \epsilon_i - \epsilon_f$ and the prime in the summation indicates that the final-state energies lie between the initial state and the Fermi level. For the holes these energies are below the Fermi level.

The final expression for the inverse lifetime then becomes

$$\tau^{-1} = 2\sum_f {}' \int \mathrm{d}\boldsymbol{r} \int \mathrm{d}\boldsymbol{r}'\, \phi_i^*(\boldsymbol{r})\phi_f^*(\boldsymbol{r})\,\mathrm{Im}[-W(\boldsymbol{r},\boldsymbol{r}',\omega)]\phi_i(\boldsymbol{r}')\phi_f(\boldsymbol{r}). \tag{4}$$

The screened interaction W is given by

$$W(\boldsymbol{r},\boldsymbol{r}',\omega) = V(\boldsymbol{r} - \boldsymbol{r}') + \int \mathrm{d}\boldsymbol{r}_1 \int \mathrm{d}\boldsymbol{r}_2 [V(\boldsymbol{r} - \boldsymbol{r}_1) + K^{xc}(\boldsymbol{r},\boldsymbol{r}_1)]\chi(\boldsymbol{r}_1,\boldsymbol{r}_2,\omega)V(\boldsymbol{r}_2 - \boldsymbol{r}'), \tag{5}$$

or in short notation

$$W = V + (V + K^{xc})\chi V. \tag{6}$$

Here V is the bare Coulomb interaction and χ the linear density–density response function, which is given by the following integral equation:

$$\chi = \chi^0 + \chi^0(V + K^{xc})\chi. \tag{7}$$

χ^0 is the density–density response function of the non-interacting electron system:

$$\chi^0(\boldsymbol{r}, \boldsymbol{r}', \omega) = 2 \sum_{i,j} \frac{\theta(E_{\mathrm{F}} - \epsilon_i) - \theta(E_{\mathrm{F}} - \epsilon_j)}{\epsilon_i - \epsilon_j + (\omega + \mathrm{i}\eta)} \phi_i(\boldsymbol{r}) \phi_j^*(\boldsymbol{r}) \phi_j(\boldsymbol{r}') \phi_i^*(\boldsymbol{r}'). \tag{8}$$

In this equation η is an infinitesimally small positive constant. The kernel K^{xc} entering Eqs. (6) and (7) accounts for the reduction of the electron–electron interaction due to the existence of short-range exchange and correlation effects associated with the probe electron (Eq. (6)) and with screening electrons (Eq. (7)). Most calculations that have been performed to date of the lifetimes of electrons and holes at surface and image-potential states use the so-called random phase approximation (RPA). In this approximation, the exchange and correlation kernel K^{xc} is omitted from both Eqs. (6) and (7).

Inclusion of exchange and correlation effects in the screened interaction (Eq. (6)) and in the screening (Eq. (7)) act in opposite directions as the evaluation of the lifetimes is concerned. This is easy to understand by considering the physics involved. Inclusion of exchange and correlation effects in the screening results in a reduced screening effect and therefore reduces the lifetime of a hot electron. When the exchange and correlation kernel is included in W (Eq. (6)), we shall refer [14] to it as WΓ while when it is included in χ (Eq. (7)) as TDLDA, so four different GW combinations are possible: GW–RPA, GWΓ–RPA, GW–TDLDA and GWΓ–TDLDA. Unless stated otherwise all calculations presented here have been made within the GW–RPA.

In the case of a homogeneous electron gas for the energies involved in surface and image-potential states and for the case of an electron density equal to that of Cu ($4s^1$) valence electrons the GW–TDLDA result for the lifetime is ∼20% less than that of GW–RPA [16]. For this particular case, this reduction is slightly more than compensated by the reduction in the interaction originated by taking into account exchange and correlation effects between the probe electron and the electron gas (GWΓ–TDLDA). As a consequence the final result differs from the GW–RPA result by an increase of about 5%. Similar quantitative results were obtained for the case of image-potential states at Cu surfaces [69]. No study of this effect in surface states is available yet [70].

2.3.1. Homogeneous electron gas

To facilitate comparison with earlier calculations we show here the results of the general theory described above when applied to the degenerate electron gas model. In the case of a uniform electron gas the single-particle wave functions are simply plane waves. The damping rate τ^{-1} of an excited bulk state of momentum $\boldsymbol{k}_i$ and energy $E = (1/2)k_i^2$ is given by [71,72]:

$$\Gamma_{k_i} = \tau_{k_i}^{-1} = \frac{1}{2\pi^2 k_i} \int_0^{2k_i} \mathrm{d}q \int_0^{\omega_{\max}} \mathrm{Im}[-W(q, \omega)] \, \mathrm{d}\omega, \tag{9}$$

where $\omega_{\max} = \min(\epsilon_i - E_{\mathrm{F}}, k_i q - q^2/2)$. $W(q, \omega)$ is the screened interaction in Fourier space:

$$W(q, \omega) = \frac{V_q}{\epsilon(q, \omega)} \tag{10}$$

with $V_q = 4\pi/q^2$. $\epsilon(q, \omega)$ is the dielectric response function of the homogeneous electron gas.

For energies very close to the Fermi level and in the high-density limit, substitution of the RPA response function of the homogeneous electron gas [73] in Eq. (9) gives the well known Quinn and

Ferrell [71] formula for the lifetime:

$$\tau_{QF} = \frac{263}{r_s^{5/2}(E - E_F)^2}.$$ (11)

Here r_s is the density parameter of the electron gas of density $n_0 = 3/4\pi r_s^3$. r_s is given in units of the Bohr radii (a.u.). The lifetime is given in fs when the energy difference from the Fermi energy is given in eV.

2.3.2. d-Screening in a homogeneous electron gas

A model to include the screening by d-electrons was suggested by Quinn [74]. In this model the homogeneous electron gas is immersed in a polarizable background of d-electrons characterized by a local dielectric function $\epsilon_d(\omega)$. The single-particle wave functions are plane waves, but the screened interaction in Fourier space is modified to

$$W'(q, \omega) = \frac{V_q}{\epsilon(q, \omega) + \epsilon_d(\omega) - 1}.$$ (12)

With this screened interaction and under the same approximations leading to Eq. (11) the lifetime is given by

$$\tau = \tau_{QF}\sqrt{\epsilon_d}.$$ (13)

The values of $\epsilon_d = \epsilon_d(\omega \to 0)$ for Ag, Au and Cu are 4, 6.6 and 5.6, respectively [52,75].

García-Lekue et al. [75] have analyzed the impact of d-electron screening and concluded that, in the long-wavelength limit ($q \to 0$) the increase of the lifetimes is negligible. That this is the case can easily be understood by looking at the small ω expansion [72,76] of the imaginary part of the bulk RPA response function. In this approximation the real (ϵ_1) and imaginary (ϵ_2) parts of the dielectric function are given by

$$\epsilon_1 = 1 + \frac{q_{TF}^2}{q^2} \quad \text{and} \quad \epsilon_2 = \frac{2\omega}{q^3}.$$ (14)

Here q_{TF} is the Thomas–Fermi value $q_{TF} = 1.56/\sqrt{r_s}$. Then the imaginary part of the screened interaction $W'(q, \omega)$ which enters Eq. (9) defining the lifetime is (for very small ω, $\epsilon_d(\omega)$ has only a real part):

$$\text{Im}[W'(q, \omega)] \simeq \frac{8\omega}{q(q_{TF}^2 + q^2\epsilon_d)^2}.$$ (15)

Small momentum transfers $q \ll q_{TF}/\sqrt{\epsilon_d}$ do not contribute to the reduction of the screened interaction and thus to the reduction of the decay rate, due to screening by the d-band.

2.3.3. Bounded electron gas

In the case of a bounded electron gas that is translationally invariant in the plane of the surface, such as the jellium model [77] or the model potential described above (see Section 2.2), single-particle wave functions are of the form:

$$\phi_{k_\parallel i}(r) = \frac{1}{\sqrt{A}} e^{ik_\parallel \cdot r_\parallel} \phi_i(z).$$ (16)

Here $\boldsymbol{r} = (\boldsymbol{r}_{\|}, z)$ and the wave functions $\phi_i(z)$ describe the motion normal to the surface. $\boldsymbol{k}_{\|}$ is a wave vector parallel to the surface and A is the normalization area.

In this case, the expression for the damping rate of an electron in a state $\phi_{\boldsymbol{k}_{\|i}}(\boldsymbol{r})$ with energy $\epsilon_{\boldsymbol{k}_{\|i}}$ and momentum parallel to the surface $\boldsymbol{k}_{\|i}$ is given by

$$\Gamma = \tau^{-1} = -2 \int \mathrm{d}z \int \mathrm{d}z' \phi_i^*(z) \operatorname{Im} \Sigma(z, z', \boldsymbol{k}_{\|i}, \epsilon_{k_{\|i}}) \phi_i(z') \tag{17}$$

and

$$\Sigma(z, z', \boldsymbol{k}_{\|i}, \epsilon_{k_{\|i}}) = \sum_{\epsilon_f, \boldsymbol{k}_{\|f}} {}'\phi_f^*(z') \operatorname{Im} W(z, z', \boldsymbol{k}_{\|i} - \boldsymbol{k}_{\|f}, \omega) \phi_f(z), \tag{18}$$

or equivalently

$$\Gamma = \tau^{-1} = -2 \sum_f {}' \int \mathrm{d}z \int \mathrm{d}z' \int \frac{\mathrm{d}\boldsymbol{q}_{\|}}{(2\pi)^2} \phi_i^*(z)\phi_f^*(z') \operatorname{Im} W(z, z', \boldsymbol{q}_{\|}, \omega) \phi_f(z)\phi_i(z'). \tag{19}$$

Here $\Sigma(z, z', \boldsymbol{k}_{\|i}, \omega)$ and $\operatorname{Im} W(z, z', \boldsymbol{q}_{\|}, \omega)$ are the 2D Fourier transforms of the electron self-energy $\Sigma(\boldsymbol{r}, \boldsymbol{r}', \omega)$ and the screened interaction $W(\boldsymbol{r}, \boldsymbol{r}', \omega)$, respectively. The energy and parallel-momentum transfer in the decay process are $\omega = \epsilon_{\boldsymbol{k}_{\|i}} - \epsilon_{\boldsymbol{k}_{\|f}}$ and $\boldsymbol{q}_{\|} = \boldsymbol{k}_{\|i} - \boldsymbol{k}_{\|f}$, respectively.

2.3.4. d-Screening in a bounded electron gas

An extension of the s–d-polarization model first proposed by Liebsch [77] for a jellium model to the model potential described above (see Section 2.2) [45] has been made recently by López-Bastidas et al. [78] and García-Lekue et al. [75,79]. In this case, the electron states are taken to be described by the eigenvalues and eigenfunctions of the model Hamiltonian and this bounded assembly of electrons is then immersed in a polarizable background of d-electrons which extends from deep into the solid up to a certain plane $z = z_\mathrm{d}$. Within this model there is translational invariance in the plane of the surface. The decay rate is obtained from Eqs. (17)–(19), but the bare Coulomb interaction V is substituted by $V'(\boldsymbol{r}, \boldsymbol{r}', \omega)$ with a 2D Fourier transform given by

$$V'(z, z', q_{\|}, \omega) = \frac{2\pi}{q_{\|}\epsilon_\mathrm{d}(z', \omega)} [\mathrm{e}^{-q_{\|}|z-z'|} + \operatorname{sgn}(z_\mathrm{d} - z')\sigma_\mathrm{d}(\omega)\,\mathrm{e}^{-q_{\|}|z-z_\mathrm{d}|}\,\mathrm{e}^{-q_{\|}|z_\mathrm{d}-z'|}], \tag{20}$$

where

$$q_{\|} = |\boldsymbol{q}_{\|}|, \tag{21}$$

$$\epsilon_\mathrm{d}(z, \omega) = \begin{cases} \epsilon_\mathrm{d}(\omega), & z < z_\mathrm{d}, \\ 1, & z > z_\mathrm{d} \end{cases} \tag{22}$$

and

$$\sigma_\mathrm{d}(\omega) = \frac{\epsilon_\mathrm{d}(\omega) - 1}{\epsilon_\mathrm{d}(\omega) + 1}. \tag{23}$$

The first term in Eq. (20) is simply the bare Coulomb interaction $V'(z, z', q_{\|})$ screened, as in the case of bulk states, by the polarization charges induced within the polarizable background. The second term

stems from polarization charges at the boundary of the dielectric medium. $\text{sgn}(x)$ indicates the sign of x.

2.3.5. First-principles calculations

When the full band structure is taken into account in the evaluation of the screened interaction the damping rate of an electron or hole in the state $\psi_{v\varkappa_{\parallel}}(\boldsymbol{r})$ with energy $E_{v\varkappa_{\parallel}}$ and band index v is given by

$$\Gamma(E_{v\varkappa_{\parallel}}) = -2 \sum_{n,k_{\parallel},q_{\parallel}} {}' \sum_{G,G'} B_{v\varkappa_{\parallel},nk_{\parallel}}(\boldsymbol{q}_{\parallel}+\boldsymbol{G}) \, \text{Im} \, W_{\boldsymbol{G},\boldsymbol{G}'}(\boldsymbol{q}_{\parallel}, |E_{v\varkappa_{\parallel}}-E_{nk_{\parallel}}|) B_{v\varkappa_{\parallel},nk_{\parallel}}^{*}(\boldsymbol{q}_{\parallel}+\boldsymbol{G}'). \tag{24}$$

Here $\varkappa_{\parallel}$, $\boldsymbol{k}_{\parallel}$ and $\boldsymbol{q}_{\parallel}$ belong to the first 2D Brillouin zone, $\boldsymbol{G}$ and $\boldsymbol{G}'$ the reciprocal lattice vectors. Since first-principles calculations are performed within the superlattice model with a supercell [80] consisting of a reasonably thick film and vacuum space the $\boldsymbol{G}$ vectors contain all G_x, G_y and G_z components. $W_{GG'}(\boldsymbol{q}_{\parallel}, \omega)$ is the 3D Fourier transform of the screened interaction $W(\boldsymbol{r}, \boldsymbol{r}', \omega)$:

$$W(\boldsymbol{r}, \boldsymbol{r}', \omega) = \sum_{\boldsymbol{q}_{\parallel}, G, G'} e^{i(\boldsymbol{q}_{\parallel}+\boldsymbol{G})\boldsymbol{r}} W_{\boldsymbol{G},\boldsymbol{G}'}(\boldsymbol{q}_{\parallel}, \omega) e^{-i(\boldsymbol{q}_{\parallel}+\boldsymbol{G}')\boldsymbol{r}'}. \tag{25}$$

Coefficients $B_{v\varkappa_{\parallel},nk_{\parallel}}(\boldsymbol{q}_{\parallel}+\boldsymbol{G})$ are

$$B_{v\varkappa_{\parallel},nk_{\parallel}}(\boldsymbol{q}_{\parallel}+\boldsymbol{G}) = \int \psi_{v\varkappa_{\parallel}}^{*}(\boldsymbol{r}) \, e^{i(\boldsymbol{q}_{\parallel}+\boldsymbol{G})\boldsymbol{r}} \psi_{nk_{\parallel}}(\boldsymbol{r}) \, d\boldsymbol{r}. \tag{26}$$

The imaginary part of the screened interaction matrix $W_{\boldsymbol{G},\boldsymbol{G}'}(\boldsymbol{q}_{\parallel}, \omega)$ can be represented as

$$W_{\boldsymbol{G},\boldsymbol{G}'}(\boldsymbol{q}_{\parallel}, \omega) = \text{Im} \, \epsilon_{\boldsymbol{G}\boldsymbol{G}'}^{-1}(\boldsymbol{q}_{\parallel}, \omega) V(\boldsymbol{q}_{\parallel}+\boldsymbol{G}), \tag{27}$$

where $\epsilon_{\boldsymbol{G}\boldsymbol{G}'}^{-1}(\boldsymbol{q}_{\parallel}, \omega)$ are the Fourier coefficients of the inverse dielectric function and $V(\boldsymbol{q}_{\parallel}+\boldsymbol{G})$ are the Fourier coefficients of the bare Coulomb potential:

$$V(\boldsymbol{q}_{\parallel}+\boldsymbol{G}) = \frac{4\pi}{|\boldsymbol{q}_{\parallel}+\boldsymbol{G}|^2}. \tag{28}$$

Within RPA the dielectric function becomes

$$\epsilon_{\boldsymbol{G}\boldsymbol{G}'}(\boldsymbol{q}_{\parallel}, \omega) = \delta_{\boldsymbol{G}\boldsymbol{G}'} - \chi_{\boldsymbol{G}\boldsymbol{G}'}^{0}(\boldsymbol{q}_{\parallel}, \omega) V(\boldsymbol{q}_{\parallel}+\boldsymbol{G}'). \tag{29}$$

Here $\chi_{\boldsymbol{G}\boldsymbol{G}'}^{0}(\boldsymbol{q}_{\parallel}, \omega)$ is the density–density response function of a non-interacting electron system (see Eq. (8)).

2.4. Ingredients of the calculation

2.4.1. Screened interaction in reciprocal space

The Fourier transforms of the screened interaction are very useful entities to understand the physics of electron (hole) dynamics at surfaces. For future comparisons we begin with the case of a homogeneous electron gas. The screened interaction in Fourier space is given by Eq. (10), which in turn gives for $W(\boldsymbol{r}, \boldsymbol{r}', \omega)$:

$$W(\boldsymbol{r}, \boldsymbol{r}', \omega) = \frac{1}{(2\pi)^2} \int W(z, z', \boldsymbol{q}_{\parallel}, \omega) \, e^{i\boldsymbol{q}_{\parallel}(\boldsymbol{r}_{\parallel}-\boldsymbol{r}_{\parallel}')} \, d\boldsymbol{q}_{\parallel}, \tag{30}$$

where

$$W(z, z', \boldsymbol{q}_\parallel, \omega) = \frac{1}{2\pi} \int W(q, \omega) \, e^{iq_z(z-z')} \, dq_z. \tag{31}$$

Here $q^2 = q_\parallel^2 + q_z^2$.

In the static limit and for the case of a Thomas–Fermi dielectric function [81], we find

$$W(z, z', q_\parallel) = \frac{2\pi}{\sqrt{q_\parallel^2 + q_{\mathrm{TF}}^2}} e^{-\sqrt{q_\parallel^2 + q_{\mathrm{TF}}^2}|z-z'|}. \tag{32}$$

The imaginary part of the screened interaction is given by

$$\mathrm{Im}[-W(z, z', q_\parallel, \omega)] = \frac{1}{2\pi} \int \frac{4\pi}{q_\parallel^2 + q_z^2} \frac{\epsilon_2}{\epsilon_1^2 + \epsilon_2^2} \, e^{iq_z(z-z')} \, dq_z. \tag{33}$$

A simpler approximation appropriate for the case of low excitation energies, can be obtained from the low-ω expansion (Eq. (14)) of the imaginary part of the bulk RPA response function [73].

The case $z = z'$ can be of guidance as the bulk limit of more complicated surface calculations. The diagonal part of the imaginary part of the screened interaction is then given by

$$\mathrm{Im}[-W(z = z', q_\parallel, \omega)] = 8\omega \int_0^\infty \frac{dq_z}{\sqrt{q_\parallel^2 + q_z^2}(q_\parallel^2 + q_z^2 + q_{\mathrm{TF}}^2)^2}. \tag{34}$$

As a function of the variable $q_\parallel' = q_\parallel/q_{\mathrm{TF}}$, $\mathrm{Im}\,W$ given by Eq. (34) scales as r_s^2.

In the bulk the maximum of $\mathrm{Im}[-W(z, z', q_\parallel, \omega)]$ occurs at $z = z'$ and is independent of the actual value of z. Fig. 3 shows this quantity as a function of ω for $q_\parallel = 0.2$ a.u., for a homogeneous electron gas of density equal to the 4s valence density of Cu ($r_s = 2.67$), obtained from Eq. (33) with the

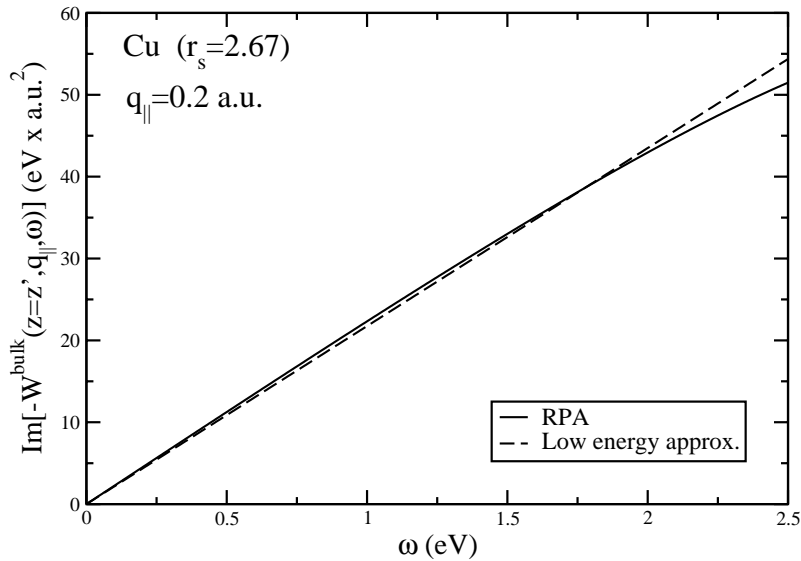

Fig. 3. $\mathrm{Im}[-W]$ of the bulk screened interaction as a function of ω for two different models of bulk homogeneous-electron-gas dielectric functions. The RPA and the approximation to it given in Eq. (14).
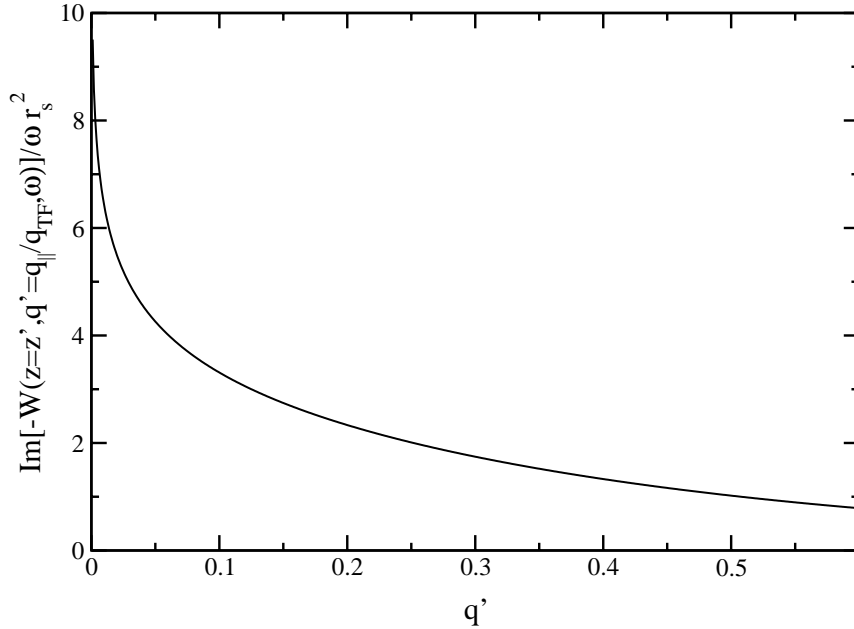
Fig. 4. $\mathrm{Im}[-W(z = z', q_{\parallel}/q_{\mathrm{TF}}, \omega)]/\omega\, r_s^2$ for the case of a homogeneous electron gas as a function of the reduced $q' = q_{\parallel}/q_{\mathrm{TF}}$ is a universal function independent of energy ω and density parameter r_s.

Lindhard RPA dielectric function [73] and the approximated low-energy form of Eq. (14). For the momentum and energy transfers of interest, the approximated form of Eq. (14) yields a screened interaction which is close to that obtained with use of the Lindhard dielectric function. The linear dependence holds for almost the whole range of energy transfers that are relevant to the dynamics of surface and image-potential states.

In Fig. 4, we show the diagonal part of the scaled imaginary part of the screened interaction as a function of the reduced momentum $q_{\parallel}/q_{\mathrm{TF}}$. When scaled by the energy ω and the square of the density parameter r_s^2 the diagonal part of the imaginary part of the screened interaction is a universal function of the reduced variable $q_{\parallel}/q_{\mathrm{TF}}$.

In Fig. 5, we show the diagonal part ($z = z'$) of the imaginary part of the screened interaction for the case of a bounded electron gas as a function of z calculated using a jellium model to describe the response of the medium for three different densities. The figure shows clearly how the breakup of symmetry at the surface and the corresponding tails of the wave functions into the vacuum result in a higher value of $\mathrm{Im}[-W]$ at the surface. Far from the crystal into the vacuum, the imaginary part of the screened interaction is well below that in bulk and near the surface. The same result is obtained in a calculation using the specular reflection model of Ritchie and Marusak [82,83] to treat the response of the medium. In this approximation, the electrons of the medium are specularly reflected at the surface and therefore are not allowed to penetrate into the vacuum, leading to a smaller maximum and a faster decay into the vacuum than in the case of the full quantum-mechanical calculation of Fig. 5, but still enhanced at the surface with respect to the bulk value.

In Fig. 6, we show the diagonal part of the screened interaction for Cu(1 1 1) calculated using the one-electron model potential described above. The result of neglecting the surface state in the
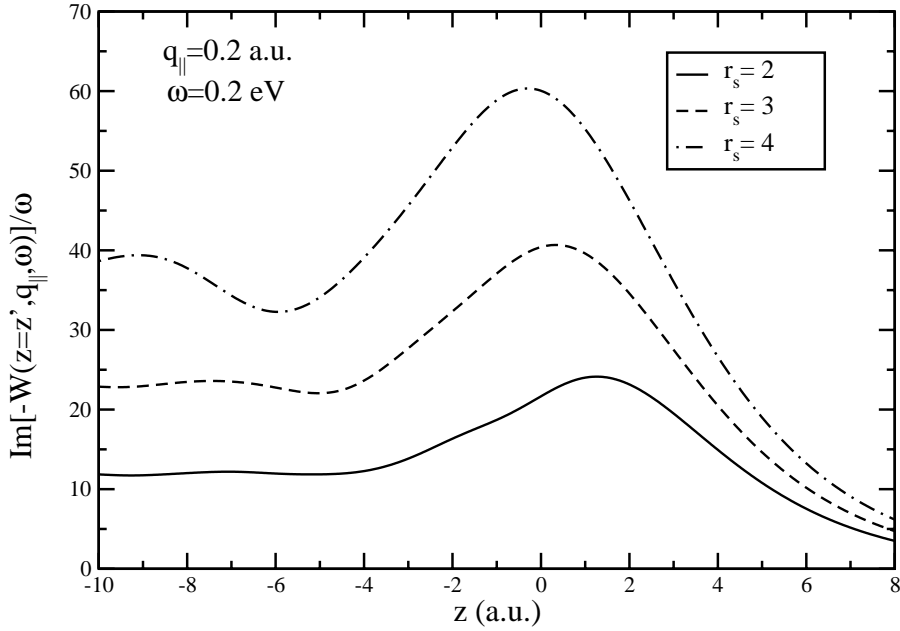
Fig. 5. Diagonal part ($z = z'$) of the imaginary part of the screened interaction $\mathrm{Im}[-W]$ calculated for $q_\parallel = 0.2$ a.u. and $\omega = 0.2$ eV, as a function of z calculated using the jellium model.

calculation of the response function is also shown, together with what would be obtained describing the system with a jellium model of density equivalent to that of the 4s valence of Cu ($r_s = 2.67$).

In Fig. 7, we show for the Cu and Au (1 1 1) surfaces the energy-scaled imaginary part of the screened interaction $\mathrm{Im}[-W]/\omega$, as a function of z going from bulk ($z < 0$) to vacuum ($z > 0$), for $q_\parallel = 0.2$ a.u. and for various values of ω. We find that at the surface $\mathrm{Im}[-W]/\omega$ is enhanced with respect to the bulk, the more so the larger the ω. For larger ω (i.e. $\omega = 0.5$ eV), but still small energies as far as the linear bulk dependence is concerned, the linear dependence with ω is no longer true at the surface. While at the bulk side the Cu values are smaller than those of Au due to the different electronic densities, at the surface side the trend is reversed due to the larger work function of Au that reduces the penetration of the tails of the wave functions into the vacuum and therefore the enhancement of the screened interaction at the surface.

Fig. 8 displays the diagonal part $\mathrm{Im}[-W]/\omega$ as a function of z, for $\omega = 0.2$ eV and for various values of $q_\parallel$. While $\mathrm{Im}[-W]/\omega$ is enhanced at the surface, for the smallest values of $q_\parallel$, by factors of 3 or 4, this enhancement is strongly reduced for the larger values of $q_\parallel$.

In Fig. 9, we show the imaginary part of the screened interaction for two different surfaces, for $q_\parallel = 0.03$ a.u., one monolayer Na/Cu(1 1 1) and clean Cu(1 1 1), showing the strong enhancement produced by the overlayer [57].

2.4.2. Electron self-energy

The imaginary part of the self-energy involves a sum over final states of the screened interaction weighted by the final-states wave functions (Eq. (18)). Figs. 10 and 11 show the results of calculations of the imaginary part of the self-energy $\mathrm{Im}[-\Sigma(z, z', k_\parallel = 0, E_n)]$ for the $n = 0$ surface-state hole and
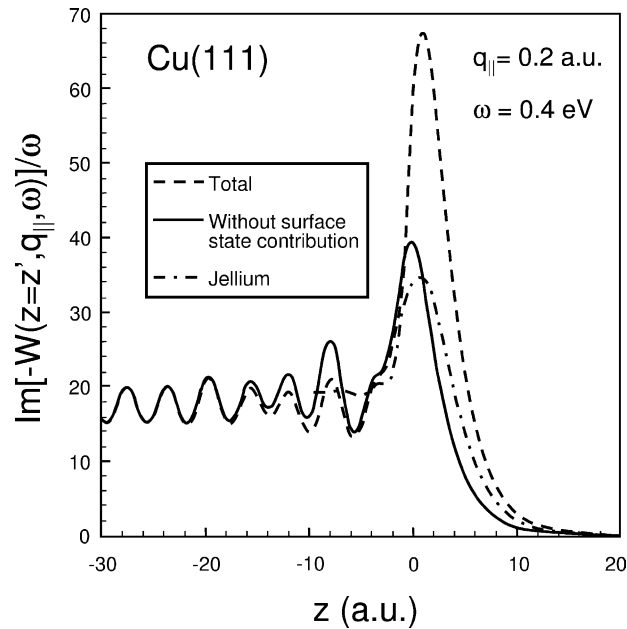
Fig. 6. Diagonal part of the imaginary part of the screened interaction for the case of a Cu(1 1 1) surface, described by the model potential. The results obtained omitting the surface state in the calculation of the response function and for a jellium model with density parameter $r_s = 2.67$ are also shown. $z = 0$ is the jellium edge.

the $n = 1$ image-potential state at the (1 1 1) surface of Cu. The imaginary part of the self-energy is represented in these figures as a function of z and for a fixed value of z'. In the bottom panels, z' is fixed at a few atomic layers within the bulk, showing that $\text{Im}(-\Sigma)$ has a maximum at $z = z'$, as in the case of a homogeneous electron gas. When z' is fixed at the crystal edge ($z' \sim 0$), as shown in the middle panels of Figs. 10 and 11, we find that $\text{Im}[-\Sigma]$ is still maximum at $z = z'$, but the magnitude of this maximum is now enhanced with respect to the bulk value. The top panels of Figs. 10 and 11 correspond to z' being fixed far from the surface into the vacuum. In this case, the maximum magnitude of $\text{Im}[-\Sigma]$ occurs at $z' \sim 0$ rather than for $z = z'$, as occurs in the case of the imaginary part of the screened interaction. As the phase space available for real transitions from the $n = 1$ image-potential state is larger than that from the excited hole at the edge of the $n = 0$ surface state $[E_1 - E_F > E_F - E_0]$, the imaginary part of the self-energy of the $n = 1$ image-potential state is larger than in the case of the $n = 0$ surface-state hole. Dotted lines in Fig. 10 represent the contribution to the imaginary part of the $n = 0$ surface-state-hole self-energy from transitions to the $n = 0$ surface state itself, the so-called intraband transitions. One sees that at the vacuum side of the surface, intraband transitions dominate, while within the bulk they represent a minor contribution.

In Figs. 12 and 13, separate contributions to the magnitude of the maximum of $\text{Im}[-\Sigma]$ for the $n = 0$ and $n = 1$ surface states are plotted, according to whether only transitions to the $n = 0$ intrinsic surface state (dotted line) or all available transitions (solid line) are included.

2.4.3. Electron–electron contribution to the decay

The model potential constructed in Refs. [44,45] and described in Section 2.2 takes explicitly into account band structure effects in the direction perpendicular to the surface. However, it assumes
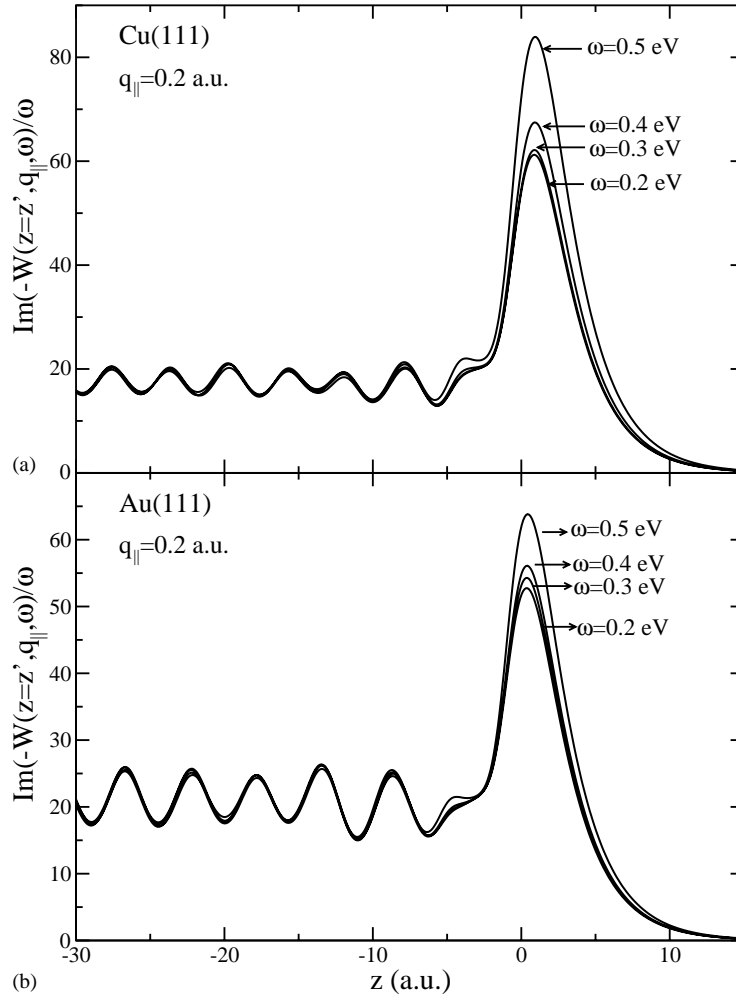
Fig. 7. Diagonal part of $\mathrm{Im}[-W]/\omega$ as a function of z for: (a) Cu(1 1 1), (b) Au(1 1 1), for $q_{\parallel} = 0.2$ a.u. and $\omega = 0.2, 0.3, 0.4, 0.5$ eV. $z = 0$ is the jellium edge. From Refs. [56,84].

free-electron motion in the plane parallel to the surface. Surface states, due to their location in the surface region, experience surface corrugation to a greater extent than image-potential states.

In the calculation of the screened interaction the electrons are taken to be free in the parallel direction. Since the screened interaction is an integrated quantity that averages over many transitions this is expected to be a reasonable approximation. In the evaluation of matrix elements between initial and final states the energy dispersion can be included by means of the effective masses. Although the model potential is constructed with data at the $\bar{\Gamma}$ point an approximation to the wave-function variation along the dispersion line, $k_{\parallel}$-corrected wave functions $\phi_s(z)$, can be obtained by applying the same procedure as for $\bar{\Gamma}$ at each $\bar{k}_{\parallel}$, using experimental data or values from first-principles calculations for the gaps and binding energy for each value of the momentum parallel to the surface.

Calculations of the decay of surface holes at the $\bar{\Gamma}$ point using the wave functions at $\bar{\Gamma}$ for all values of the parallel momentum yield rates approximately 20% higher than the ones obtained using the
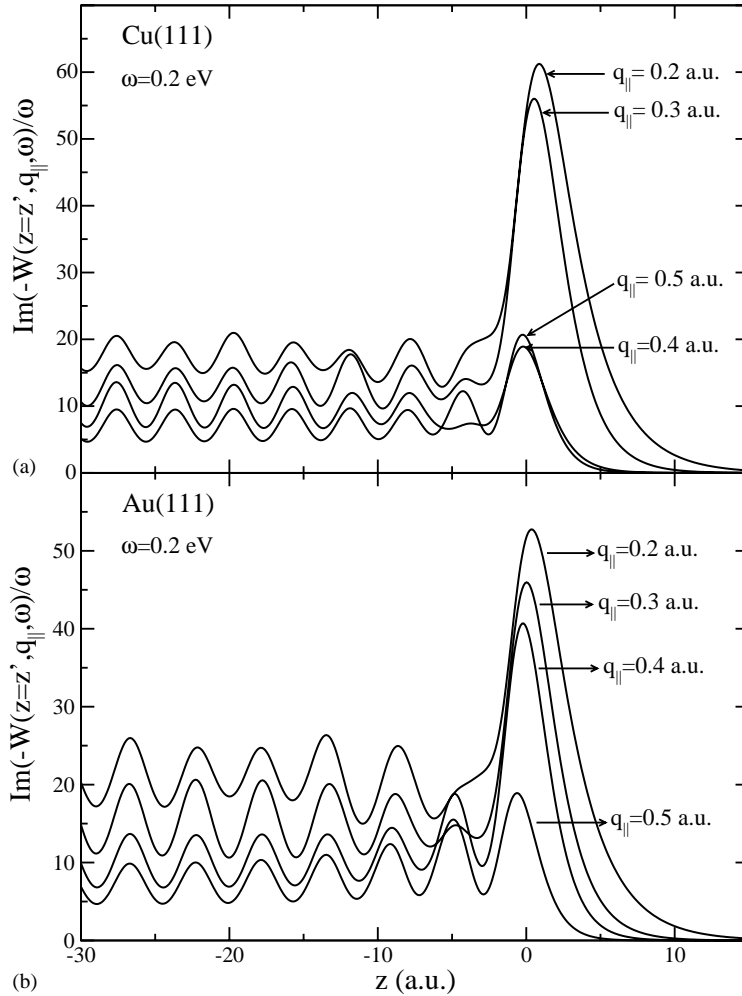
Fig. 8.   Im$[-W]/\omega$ as a function of z for: (a) Cu(1 1 1), (b) Au(1 1 1), for $\omega = 0.2$ eV and $q_\parallel = 0.2, 0.3, 0.4, 0.5$ a.u.; $z = 0$ is the jellium edge. From Refs.[55,56].

$k_\parallel$-corrected wave functions [53,55,85]. Unless stated otherwise the $k_\parallel$-corrected wave functions are the ones that have been used in the calculations presented here.

Separate contributions from intraband (within the surface state itself) and interband (between bulk states and the surface state) transitions to the decay of Shockley surface-state holes at the $\bar{\Gamma}$ point of the projected bulk band gap of the (1 1 1) surfaces of Cu, Ag and Au are displayed in Table 2. We also show the decay rate evaluated within a 3D electron-gas model (EGM) for a hole with energy at the bottom of the surface-state band. The comparison of the calculated decay rates shows that the EGM gives decay rates values which are significantly smaller than those obtained using the model potential. The EGM takes into account only 3D transitions and neglects both band structure and surface effects. The results of the calculations displayed in Table 2 show that these effects are crucial for the hole lifetimes in surface states. In particular, intraband transitions within the surface-state band itself
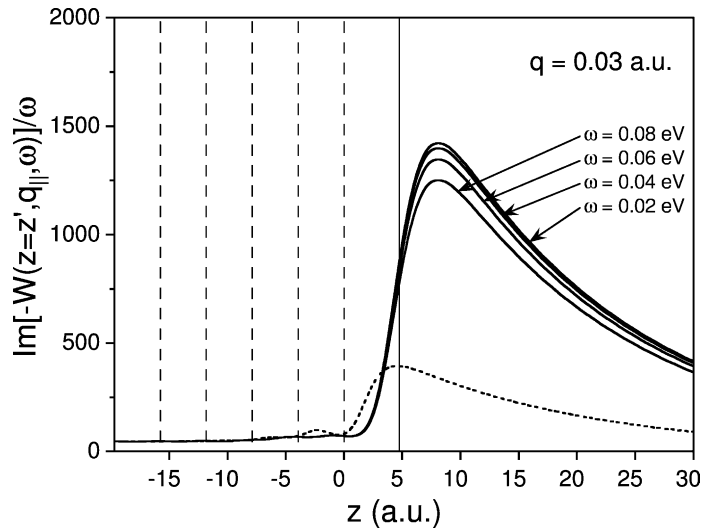
Fig. 9. $Im[−W]/\omega$ for $q_{\parallel} = 0.03$ a.u. and different values of ω, for Cu(1 1 1) + Na (solid lines) and Cu(1 1 1) (short-dashed line). Vertical solid line indicates the position of the sodium adlayer and vertical dashed lines represent the copper atomic layers positions.

(2D → 2D transitions) contribute ∼80% of the total electron–electron decay rate. These transitions are more efficient in filling the hole than those arising from bulk states 3D → 2D (interband) transitions because of the greater overlap of the initial- and final-state wave functions which exists in the region where the imaginary part of the screened interaction is larger than in the bulk (see Figs. 6–8 and 14).

Differences between the full interband calculations using the model potential and those obtained from the electron-gas model arise from: (i) the enhancement of $Im[−W]$ at the surface, which increases the decay rate, (ii) localization of the surface-state wave function in the direction perpendicular to the surface and (iii) the restriction that only bulk states with energy lying outside the projected band gap are allowed (see also Fig. 14). Both localization of the surface-state wave function and the presence of the band gap reduce the decay rate, and therefore they tend to compensate the enhancement of $Im[−W]$ at the surface. In the case of Cu(1 1 1) this compensation is almost complete, thereby yielding an interband decay rate that nearly coincides with the 3D decay of free holes. However, as can be seen from Table 2, this is not necessarily the case for other materials such as Ag or Au and depends in particular on the surface band structure. In the case of the hole at the $\bar{\Gamma}$ point at Be(0 0 0 1) the model-potential interband value is 40 meV while the 3D electron gas result is 90 meV [53].

Table 2
Decay rates in meV of the Shockley surface-state hole at the $\bar{\Gamma}$ point of the noble-metal (1 1 1) surfaces

Surface	Energy (eV)	Γ_{EGM}	Γ_{inter}	Γ_{intra}	Γ_{ee}
Cu(1 1 1)	−0.445	5.9	6	19	25
Ag(1 1 1)	−0.067	0.18	0.3	2.7	3
Au(1 1 1)	−0.505	10	8	21	29

The total decay rate Γ_{ee} is decomposed into interband (Γ_{inter}) and intraband (Γ_{intra}) contributions. Decay rates in a 3D electron gas model (Γ_{EGM}) of holes with the energy of the Shockley surface-state at $\bar{\Gamma}$ are also displayed. From Ref. [56].
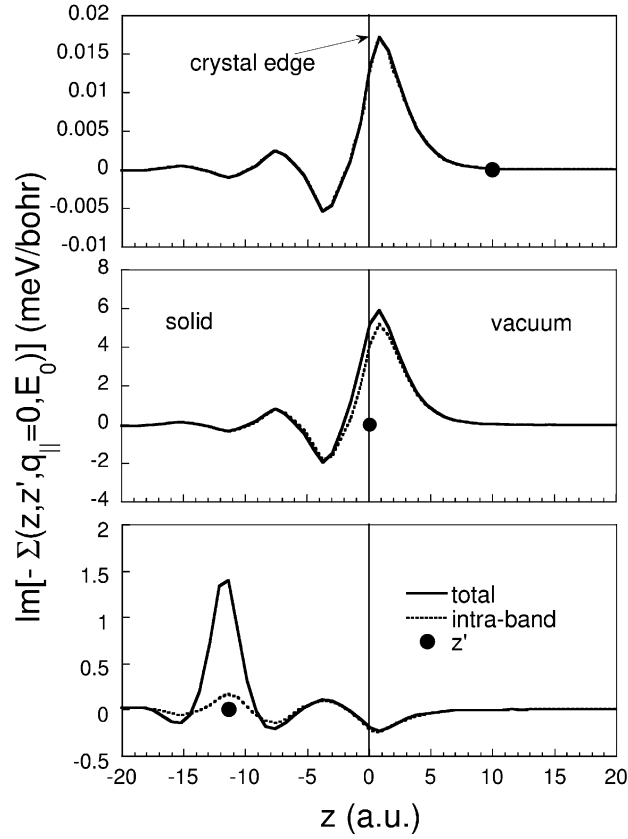
Fig. 10. Imaginary part of the self-energy at an energy of the $n = 0$ surface-state hole, $\text{Im}[-\Sigma(z, z', q_\parallel = 0, E_0)]$, vs. z, in the vicinity of the (1 1 1) surface of Cu, with the use of the model potential. z' is fixed at -11.3 (bottom), 0 (middle) and 10 a.u. (top). Dotted lines represent the contribution from transitions to the $n = 0$ surface state itself. From Ref. [85].

The impact of the enhanced $\text{Im}[-W]$ at the surface on both interband and intraband contributions to the Shockley surface-state hole decay at the $\bar{\Gamma}$ point in Cu(1 1 1) is illustrated in Fig. 15. In this figure, the results of the calculations of the interband and intraband contributions to the total inelastic decay rate (full circles) are compared to the results obtained using wave functions derived from the model potential but replacing the screened interaction with the homogeneous electron gas result of Eq. (14) (full triangles). 3D free-electron-gas calculation is represented by an open square. The impact of the surface anisotropy on $\text{Im}[-W]$ (difference between full circles and triangles) is to strongly increase both interband and intraband contributions to the decay. Fig. 15 clearly shows that the agreement, in the case of Cu(1 1 1), between our interband decay rate (full circle) and that obtained from the 3D free-electron gas calculation (open square) is due to a fortuitous cancellation between both localization of the surface-state wave function and the presence of the band gap, on the one hand, and the enhancement of $\text{Im}[-W]$ at the surface, on the other hand. We also note from this figure that a large contribution from intraband transitions, strongly screened by the underlying 3D bulk electron system, is responsible for the large differences between the 3D free-electron gas prediction and the experimental results (represented by open triangles), as discussed in Ref. [52].
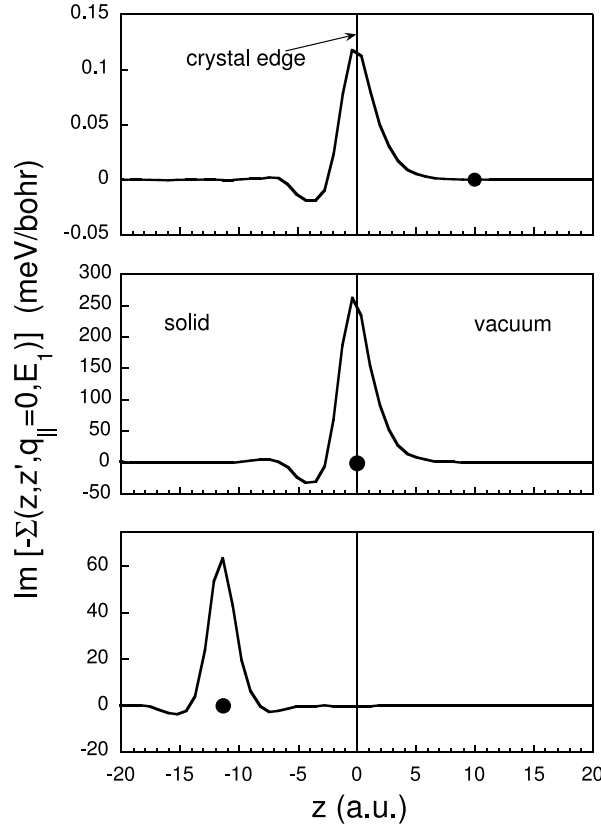
Fig. 11. Imaginary part of the self-energy at an energy of the $n = 1$ image-potential state, $\mathrm{Im}[-\Sigma(z, z', q_\parallel = 0, E_1)]$, vs. z, in the vicinity of the (1 1 1) surface of Cu, with the use of the model potential. z' is fixed at -11.3 (bottom), 0 (middle) and 10 a.u. (top). From Ref. [85].

Calculations based on a pure 2D electron-gas model to describe the surface state give results that are much larger than the model-potential intraband contribution to the decay rate by factors of ~ 7 for the state at the $\bar{\Gamma}$ point in Cu(1 1 1) and by a factor of ~ 2.5 in Be(0 0 0 1). These large discrepancies are due to the fact that electron–electron interactions within the actual 2D Shockley surface-state band are strongly screened by the underlying 3D bulk electron system, thereby reducing the scattering probability. The relative importance of the 3D screening with respect to the total screening increases with decreasing binding energy of the surface states. In Ag(1 1 1) the screening is practically only 3D, while in Be(0 0 0 1) the surface-state band contributes significantly to the total screening.

2.5. Electron–phonon interaction

The phonon-induced linewidth broadening Γ_{ep} of surface states of energy E and parallel momentum $\boldsymbol{k}_{\parallel i}$ that takes into account both the phonon absorption and emission processes can be written as [87]:

$$\Gamma_{\mathrm{ep}}(\boldsymbol{k}_{\parallel i}, E) = 2\pi \int_0^{\omega_{\mathrm{m}}} \alpha^2 F_{\boldsymbol{k}_{\parallel i}}(\omega)[1 + 2n(\omega) + f(E + \omega) - f(E - \omega)]\, \mathrm{d}\omega, \tag{35}$$
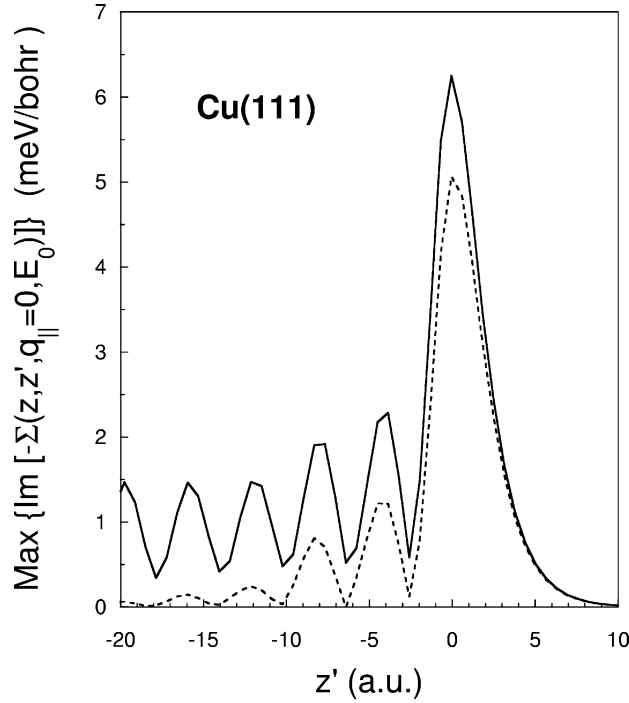
Fig. 12. Maximum of the imaginary part of the self-energy at an energy of the $n = 0$ surface-state, $\text{Im}[-\Sigma(z, z', q_{\parallel} = 0, E_0)]$, vs. z', in the vicinity of the (1 1 1) surface of Cu. Dotted lines represent the contribution from transitions to the $n = 0$ surface state itself. From Ref. [85].

where f and n are the electron and phonon distribution functions, respectively, and ω_{m} the maximum phonon frequency. The Eliashberg function $\alpha^2 F(\omega)$ which is the phonon density of states weighted by the electron–phonon coupling function g, can be written in a quasielastic approximation as

$$\alpha^2 F_{\boldsymbol{k}_{\parallel i}}(\omega) = \sum_{v, \boldsymbol{q}_{\parallel}, f} |g_{i,f}^v(\boldsymbol{q}_{\parallel})|^2 \delta(\omega - \omega_v(\boldsymbol{q}_{\parallel}))\delta(\epsilon_f - \epsilon_{\boldsymbol{k}_{\parallel i}}), \tag{36}$$

where $\omega_v(\boldsymbol{q}_{\parallel})$ is the phonon frequency, v the phonon index and the last δ-function indicates that we consider the quasielastic approximation [19], neglecting the change of the energy of the scattered electron due to absorption or emission of a phonon. The electron–phonon coupling function includes the matrix element between the initial (i) and final (f) electron band states. For a translationally invariant system (see Eq. (16)) the matrix element involves a z-integration only

$$g_{i,f}^v(\boldsymbol{q}_{\parallel}) = \frac{1}{\sqrt{2MN\omega_v(\boldsymbol{q}_{\parallel})}} \left\langle f \left| \sum_{\mu} \epsilon_{\boldsymbol{q}_{\parallel} v}(\boldsymbol{R}_{\mu}) \cdot \boldsymbol{\nabla}_{\boldsymbol{R}_{\mu}} \tilde{V}_{\boldsymbol{q}_{\parallel}}^{\mu} \right| i \right\rangle. \tag{37}$$

In this expression i and f refer to the z-dependent wave functions $\phi(z)$ in Eq. (19). The static screening of the electron-ion potential is used and thus one neglects the frequency dependence of the coupling function $g_{i,f}^v(\boldsymbol{q}_{\parallel})$. The coupling function in Eq. (37) is the result of the standard first-order expansion of the screened electron-ion potential $\tilde{V}_{\boldsymbol{q}_{\parallel}}^{\mu}$ with respect to the vibrational coordinate $\boldsymbol{R}_{\mu}$. N is the number of
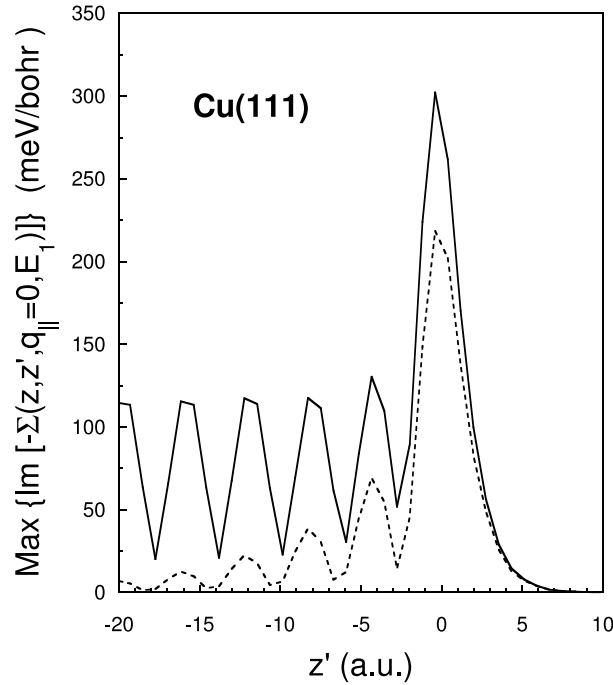
Fig. 13. Maximum of the imaginary part of the self-energy at an energy of the $n = 1$ image-potential state, $\mathrm{Im}[-\Sigma(z, z', q_{\parallel} = 0, E_1)]$, vs. z', in the vicinity of the (1 1 1) surface of Cu. Dotted lines represent the contribution from transitions to the $n = 0$ surface state. From Ref. [85].
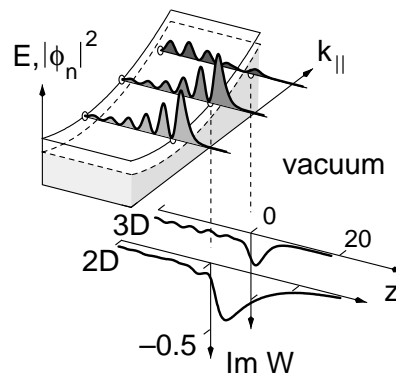
Fig. 14. There is only a gradual evolution in the wave functions $\phi_n(z)$ of states through the occupied portion of the surface-state band, leading to large overlap with the hole wave function ϕ_0 at the band minimum. In contrast, wave functions associated with levels within the continuum of bulk states exhibit a different spatial distribution near the surface, leading to smaller overlap and making interband transitions less important than intraband transitions in filling the hole. The screened interaction is significantly enhanced near the surface (in the low part of the figure $\mathrm{Im}\, W(z, z)$ is shown, in atomic units), both for 2D intraband and 3D interband transitions, coinciding with where the hole state is concentrated. This results in a hole-decay rate that is much larger than that of bulk states at a similar energy. From Ref. [52].

Fig. 15. Band-edge ($k_\parallel = 0$) Shockley surface-state hole-decay rates in Cu(1 1 1). Full circles: separate interband and intraband contributions to the total inelastic decay, as obtained from Eq. (19) with a surface calculation of $W(z, z', \boldsymbol{q}, |E_i - E_f|)$. Full triangles: separate interband and intraband contributions to the total inelastic decay, as obtained from Eq. (19) with $W(z, z',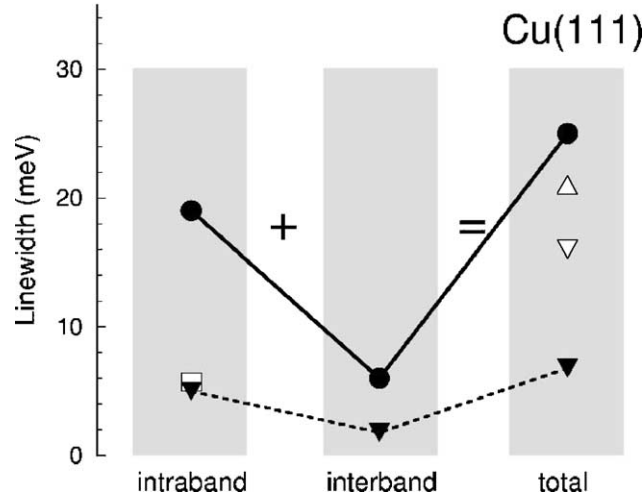 \boldsymbol{q}, |E_i - E_f|)$ replaced by that of Eq. (14). Open square: 3D free-electron-gas calculation of intraband decay rate. The experimentally determined inelastic decay rates of Refs. [86] (after extrapolation of the PES linewidth to zero defect density) and [52] (after subtraction of an estimated electron–phonon linewidth of 8 meV) are represented by the open triangle and the inverted open triangle, respectively. Adapted from Ref. [56].

ions in each atomic layer, M is the ion mass, μ is the layer index and $\epsilon_{\boldsymbol{q}_\parallel v}(\boldsymbol{R}_\mu)$ are the phonon polarization vectors. From Eq. (35) we easily obtain the $T = 0$ result ($n(\omega) = 0$) for Γ_{ep}:

$$\Gamma_{\text{ep}}(\boldsymbol{k}_{\parallel i}, E) = 2\pi \int_0^{|E|} \alpha^2 F_{\boldsymbol{k}_{\parallel i}}(\omega) \, \mathrm{d}\omega. \tag{38}$$

For binding energies $|E| > \omega_{\text{m}}$ the upper limit for the integration should be the maximum phonon frequency ω_{m}.

From the knowledge of the Eliashberg function [17,18], the electron–phonon coupling parameter λ can be calculated as the first reciprocal moment of the Eliashberg function:

$$\lambda(\boldsymbol{k}_{\parallel i}) = 2 \int_0^{\omega_{\text{m}}} \frac{\alpha^2 F_{\boldsymbol{k}_{\parallel i}}(\omega)}{\omega} \, \mathrm{d}\omega. \tag{39}$$

If the high temperature limit ($k_{\text{B}} T \gg \omega_{\text{m}}$, here k_{B} is the Boltzmann constant) of Eq. (35) is considered, Grimvall [19] has pointed out a very useful result which enables an experimental determination of the mass enhancement parameter:

$$\Gamma_{\text{ep}}(\boldsymbol{k}_{\parallel i}, E) = 2\pi \lambda(\boldsymbol{k}_{\parallel i}) k_{\text{B}} T. \tag{40}$$

The above equations show that the Eliashberg function $\alpha^2 F$ is a basic function to calculate. Given this function most of the interesting quantities can be calculated, such as the temperature and also energy dependence of the linewidth broadening and the electron–phonon coupling parameter. However, this is

not a simple task, as all the physics connected to the electron–phonon interaction is buried in $\alpha^2 F$, the phonon-dispersion relation, phonon polarization vectors, one-electron wave functions and the gradient of the screened electron-ion potential—the deformation potential. All these quantities, and finally $\alpha^2 F$ for bulk metal electron states, can be obtained from first-principles calculations [88], whereas for electron states on metal surfaces these evaluations are very time consuming [89]. Some approximations are needed to make these computations feasible for surfaces.

In particular, the phonon-dispersion relations and polarization vectors can be calculated with reasonable accuracy using force-constant models [90] or the embedded-atom method [91–93]. In recent calculations of Γ_{ep} and λ for surface states, one-electron wave functions obtained by using the one-electron model potential [44,45] have been used. For the description of the deformation potential the screened electron-ion potential as determined by the static dielectric function and the bare pseudopotential is used, $\tilde{V}_{q_{\parallel}}^{\mu}(z) = \int dz' \tilde{\epsilon}^{-1}(z, z', q_{\parallel}) \tilde{V}_{bare}^{\mu}(z', q_{\parallel})$, where $q_{\parallel}$ is the modulus of the phonon momentum wave vector parallel to the surface and $\tilde{V}_{bare}^{\mu}$ the 2D Fourier transform parallel to the surface of the bare electron-ion pseudopotential [94]. The effect of the screening was investigated using two dielectric functions, namely the bulk Thomas–Fermi and an RPA dielectric function, constructed from the wave functions and eigenvalues of a 31-layer slab calculation using the model potential [95–97]. The difference between the results of the two calculations is about 1% for both λ and Γ_{ep} due to a compensating effect. Referring to the surface layer, Thomas–Fermi screening is symmetric while RPA yields a screening slightly stronger below and slightly weaker above.

A drastic simplification is obtained by taking $g_{i,f}^{\nu}(q_{\parallel})$ to be constant. In this case the Eliashberg function is proportional to the product of the phonon and electron densities of states. Assuming a free-electron-gas model for the one-electron states one can obtain simple analytical expressions for the Eliashberg function and for the phonon contribution to the linewidth broadening Γ_{ep} within the Debye and Einstein models for vibrational spectra in terms of the energy-dependent electron–phonon coupling parameter and the characteristic Debye (Einstein) energy ω_D (ω_E). They are listed in Table 3.

Until very recently, the phonon contribution to the decay of surface states was usually estimated using the 3D Debye phonon model with λ obtained from measurements or theoretical calculations of bulk properties [19]. However, it is not obvious that this approach should be adequate for surface-state

Table 3
Eliashberg function and phonon contribution to decay for Einstein and Debye models with characteristic frequencies ω_E and ω_D, respectively

References	$\alpha^2 F(\omega)$	Γ_{ep}
Einstein [19]	$\frac{1}{2}\lambda\omega_E\delta(\omega - \omega_E)$	$\pi\lambda\omega_E,\ E > \omega_E$
		$0,\ E < \omega_E$
Debye 3D [19]	$\frac{\lambda\omega^2}{\omega_D^2},\ \omega < \omega_D$	$\frac{2}{3}\pi\lambda\omega_D,\ E > \omega_D$
	$0,\ \omega > \omega_D$	$\frac{2}{3}\pi\lambda\omega_D(\omega/\omega_D)^3,\ E < \omega_D$
Debye 2D [98]	$\frac{(\lambda/\pi)\omega}{(\omega_D^2 - \omega^2)^{1/2}},\ \omega < \omega_D$	$2\lambda\omega_D,\ E > \omega_D$
	$0,\ \omega > \omega_D$	$2\lambda\omega_D\left(1 - \sqrt{1 - \left(\frac{\omega}{\omega_D}\right)^2}\right),\ E < \omega_D$

E is the electron surface-state energy and λ is the electron–phonon coupling parameter.

electrons or holes because the surface state itself, as well as the surface phonon modes, are not taken into account. A more rigorous treatment of the electron–phonon contribution is needed especially for surface states close to the Fermi level, because for these states the electron–electron contribution is small and the electron–phonon interaction becomes dominant even at low temperatures.

A more refined theoretical analysis of the electron–phonon contribution to the linewidth broadening of surface states taking into account all electron and phonon states involved in the electron–phonon scattering process is required. The theoretical analysis of Eiguren et al. [95,96], based on a calculation of the full Eliashberg spectral function, is a step forward in this direction. In this approach the contributions from different phonon modes, in particular the Rayleigh surface mode as well as bulk phonons and the general temperature dependence are taken into account. They also obtain the high temperature behavior represented by λ. Their approach is based on: (i) Thomas–Fermi screened Ashcroft electron-ion potentials, (ii) one-electron states obtained from the model potential, and (iii) a simple force-constant phonon model calculation that gives results for the phonon spectrum in good agreement with recently published experimental data [52,86,99,100].

In Fig. 16, the calculated phonon dispersion and the Eliashberg function at the $\bar{\Gamma}$ point calculated by Eiguren et al. [95,96] is presented for the Cu(1 1 1) surface. The Rayleigh surface mode is split off from the bulk phonon band, which gives a lower energy peak in the Eliashberg function of the hole state at the $\bar{\Gamma}$ point of about $\sim$13 meV in Cu(1 1 1). The oscillations in the Eliashberg function reflect the finite number of layers of the model-potential calculation (31 layers) of electron wave functions and thus have no physical significance [95].
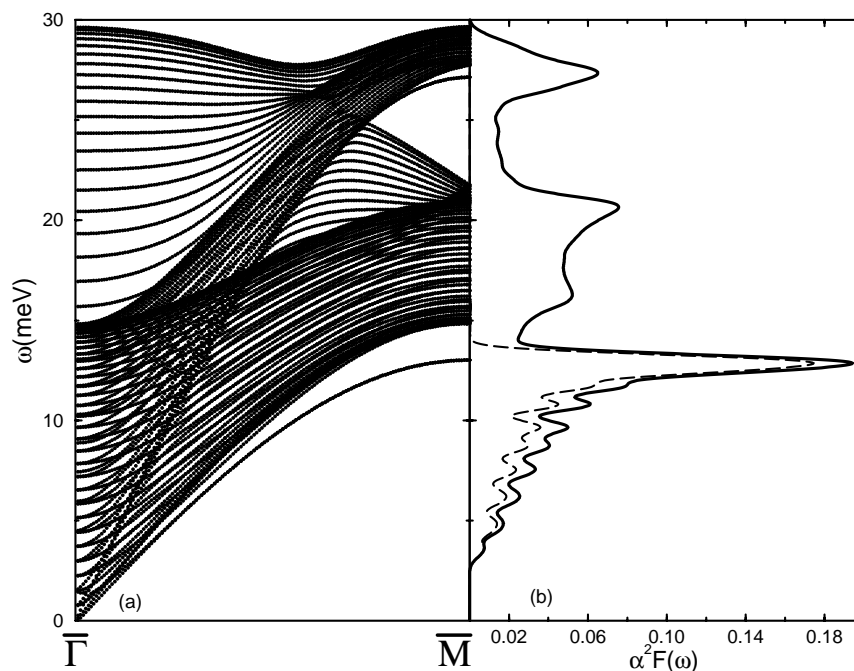

Fig. 16. (a) The phonon dispersion from a 31-layer slab calculation in the $\overline{\Gamma M}$-direction of the surface Brillouin zone. (b) The Eliashberg function of the hole state in the $\bar{\Gamma}$ point for Cu(1 1 1) (solid line) and the contribution from the Rayleigh mode to the Eliashberg function (dashed line). From Ref. [95].
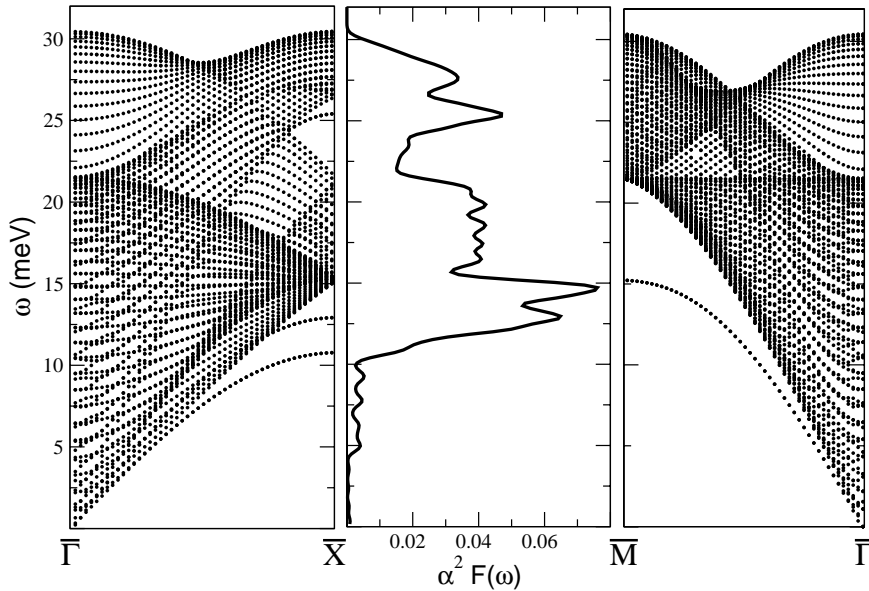
Fig. 17. One force constant phonon dispersion and Eliashberg function $\alpha^2 F(\omega)$ for the Cu(1 0 0) surface. In the case of the Ag(1 0 0) surface, dispersion is qualitatively very similar.

In Fig. 17, we show the results of the calculations by Eiguren et al. [101] of the phonon dispersion and the Eliashberg functions of the image-potential state at the $\bar{\Gamma}$ point for Cu(1 0 0). The Rayleigh mode contribution dominates in the energy range 12–15 meV. The feature around 25 meV corresponds to the longitudinal surface mode. Note the lower values of the Eliashberg function of the $n = 1$ state in Cu(1 0 0) with respect to the surface state in Cu(1 1 1) arising from the different penetration of the wave function into the bulk (75% for the surface state and 5% for the image-potential state).

The use of the 3D and 2D Debye models in the evaluations of Γ_{ep} for holes in surface states on the (1 1 1) surface of noble metals [52] and Al(1 0 0) normally leads to a fairly good agreement with the results of more sophisticated calculations [87,95,96].

3. Photoelectron spectroscopy

During the last three decades angle-resolved photoelectron spectroscopy [24,25] has matured to an important tool for the study of occupied surface states. From the kinematic constraints of energy- and momentum-conservation the energy versus 2D wave-vector relation $E(\boldsymbol{k}_{\parallel})$ can now be determined routinely provided a high-quality single-crystal and a worked-out recipe to prepare a well-ordered and stoichiometrically correct surface are available [24,25]. Band mapping, however, represents only the lower level of photoelectron spectroscopy. The higher level is to derive the dynamical information from the interpretation of lineshapes, linewidths and peak intensities. The present section is written to illuminate the influence of various physical processes on the lineshape, to give a short history of experimental progress made over the years and to summarize the present state of the art.

3.1. Photoemission lineshape analysis

In the one-electron description of photoemission an electron interacts with the electromagnetic field $A(r, t)$. Neglecting spin-orbit coupling the non-relativistic interaction Hamiltonian in the Schrödinger equation is written [27] as

$$H_{\text{int}}\psi = \frac{1}{2m}\left[-2\frac{e\hbar}{ic}A \cdot \nabla - \frac{e\hbar}{ic}(\nabla \cdot A) + \frac{e^2}{c^2}|A|^2\right]\psi, \tag{41}$$

where ψ is the wave function of the electron. In the standard angle-resolved experiment, using laboratory photon sources or monochromatized synchrotron radiation to excite photoemission, the last term can be neglected in the emitted electron current. The term with $\nabla \cdot A$ induces "surface emission" which in some cases has been identified experimentally by its interference with bulk direct transitions and a concomitant and considerable lineshape asymmetry [102–104]. Consequently the $\nabla \cdot A$ term does not contribute to the lineshape of photoemission from surface states. With the remaining interaction operator the transition rate between an initial state $|i\rangle$ and a final state $|f\rangle$ is given by Fermi's golden rule as proportional to the matrix element M_{fi} expressed as

$$|M_{fi}|^2 \propto |A \cdot \langle f|p|i\rangle|^2 = |A \cdot P_{fi}|^2, \tag{42}$$

where P_{fi} is the "momentum matrix element" for an electric dipole transition [24,25,27]. Surface-state energies depend only on the wave vector parallel to the surface:

$$|k_{\parallel}| = k_{\parallel} = \sqrt{\left(\frac{2m}{\hbar^2}\right) \cdot E_{\text{kin}}} \cdot \sin\theta, \tag{43}$$

where θ is the electron emission angle referred to the surface normal, and $k_{\parallel}$ is conserved (modulo surface reciprocal lattice vectors $g_{\parallel}$) in the photoemission process. Including energy and $k_{\parallel}$-resolution by δ-functions, the detected angle-resolved photocurrent is given by

$$I \propto |M_{fi}|^2\delta(E_f - E_i - \hbar\omega) \cdot \delta(k_{\parallel f} - k_{\parallel i} - g_{\parallel}), \tag{44}$$

where the final-state energy E_f is connected with the measured kinetic energy by $E_{\text{kin}} = E_f - \Phi$, and Φ is the work function. As is evident from Eq. (44) the unavoidable finite experimental resolution with respect to $E_{\text{kin}}, \hbar\omega$, and $k_{\parallel}(\theta)$ will replace the δ-functions by spectral distribution functions with finite width. This will be discussed further below in the historical context. Note that also a certain degree of sample perfection is required to define and to conserve $k_{\parallel}$.

While Eqs. (41)–(44) describe the kinematic constraints used to map $E(k_{\parallel})$ any measurement of dynamical information requires to probe the low-energy quasiparticle excitations as discussed in Section 2. It has been realized already early in the history of photoemission that both the screened and decaying hole left behind with a certain lifetime τ_{h} and the finite escape depth of the photoelectron (resulting in an uncertainty of the electron wave vector $k_{\perp}$ perpendicular to the surface) contribute significantly to the experimentally observed lineshape [105–108]. In fact, bulk direct-transition linewidths are in most cases dominated by the final-state damping, see e.g. Refs. [109–111] and both quantitative experimental data (see e.g. Refs. [112,113]) and theoretical understanding [16] are

available. However, surface states do not depend on $k_\perp$ and therefore the dynamical lineshape contribution is only given by the hole decay. Assuming an exponential decay in time the spectral function of the hole is given by [24,25,27]:

$$A_h = \frac{1}{\pi} \frac{\Gamma_h/2}{(E_f - E_i - \hbar\omega)^2 + (\Gamma_h/2)^2}. \tag{45}$$

In this equation $\Gamma_h/2 = |\text{Im} \Sigma|$ is the imaginary part of the quasiparticle self-energy and E_i the experimental photoelectron initial-state energy including the real part of Σ. From the full width at half maximum (FWHM) of the experimental spectral function, Γ_h and the lifetime of the hole $\tau_h = \hbar/\Gamma_h$ can be obtained. All electronic correlation effects are lumped into the self-energy. However, besides electron–electron (ee) scattering, also electron scattering with phonons (ep) and defects (def) contribute to Γ_h. If these processes occur independent of each other the contributions are additive and

$$\Gamma_h = \Gamma_{ee} + \Gamma_{ep} + \Gamma_{def}. \tag{46}$$

In what follows we discuss how these contributions can be distinguished and determined separately.

3.2. Shockley states on noble-metal surfaces

The investigation of electronic surface states has a long history. Their existence was postulated from theoretical analysis of simple quantum-mechanical models already seven decades ago [9,11]. Only in the last three decades, however, the development of angle-resolved photoemission allowed to study both their existence and their properties in sufficient detail. A recent collection of references to the earlier literature can be found in Refs. [24,25,27]. In particular with respect to linewidth studies, and their interpretation in terms of hole lifetimes, the low-index noble-metal surfaces played an important prototypical role [27]. This is due to the fact that their surfaces can be prepared with sufficient quality, the substrate bulk bands are well understood, energy gaps are available to support ''model'' surface states and, in particular, these states produce well-defined and narrow photoemission peaks. For many years their linewidths have been equated to electronic state lifetimes. This, however, may be substantially incorrect in general. We will therefore discuss some examples in detail.

The Shockley states existing near E_F in the ΓL projected bulk band gap of the (1 1 1) surfaces of Cu, Ag and Au have been investigated all over the history of photoemission, with ever improving experimental resolution and physical understanding. In particular the state around $\bar{\Gamma}$ on Cu(1 1 1) has attracted considerable interest. Slagsvold et al. [107] stated in 1983 that ''the problems of sample preparation, instrumental resolution and interpretation of spectra turn the reliable measurement of lifetimes into a demanding endeavor''. With the resolution parameters then available, they resolved the peak at $\bar{\Gamma}(k_\parallel = 0)$ with an FWHM of 250 meV on the annealed Cu(1 1 1) sample. After ion bombardment the width increased to 400 meV. This increase in width, connected with increasing asymmetry into the direction of the $k_\parallel$-dispersion of the state, was interpreted as a disorder-induced relaxation of the sharpness of $k_\parallel$ [107].

With highly improved resolution both in energy and angle Kevan [114] studied the same state. At $\bar{\Gamma}$ he obtained a measured width of 70 meV, which extrapolates to 55 meV if the experimental resolution is taken into account. This is clearly much smaller than previously reported by several groups. Surprisingly, however, the peak width increased on approaching E_F. This clearly contradicts the

expectation based on Fermi-liquid theory that $\Gamma_h \to 0$ with $E_i \to E_F$ due to vanishing phase space for scattering. Tersoff and Kevan [115] gave an interpretation in terms of weakened $k_\parallel$-conservation and attributed this effect to a finite mean free path for elastic electron scattering from a small number of defects or impurities present at the surface.

The influence of weakened $k_\parallel$-conservation is similar to the effect of the finite angular resolution $\Delta\theta$ which results in a finite resolution $\Delta k_\parallel$, compare Eq. (43). This is explained more clearly in Fig. 18 [27]. Fig. 18a reproduces the experimental band structure $E(k_\parallel)$ around $\bar{\Gamma}$, showing a parabolic dispersion with a constant effective mass up to E_F at $E_i = 0$. Contributions to the linewidth of the emission peak at a nominal value $k_\parallel = 0$ are indicated for different angular resolution $\Delta\theta$ between $\pm 0.4°$ and $\pm 3°$ by the
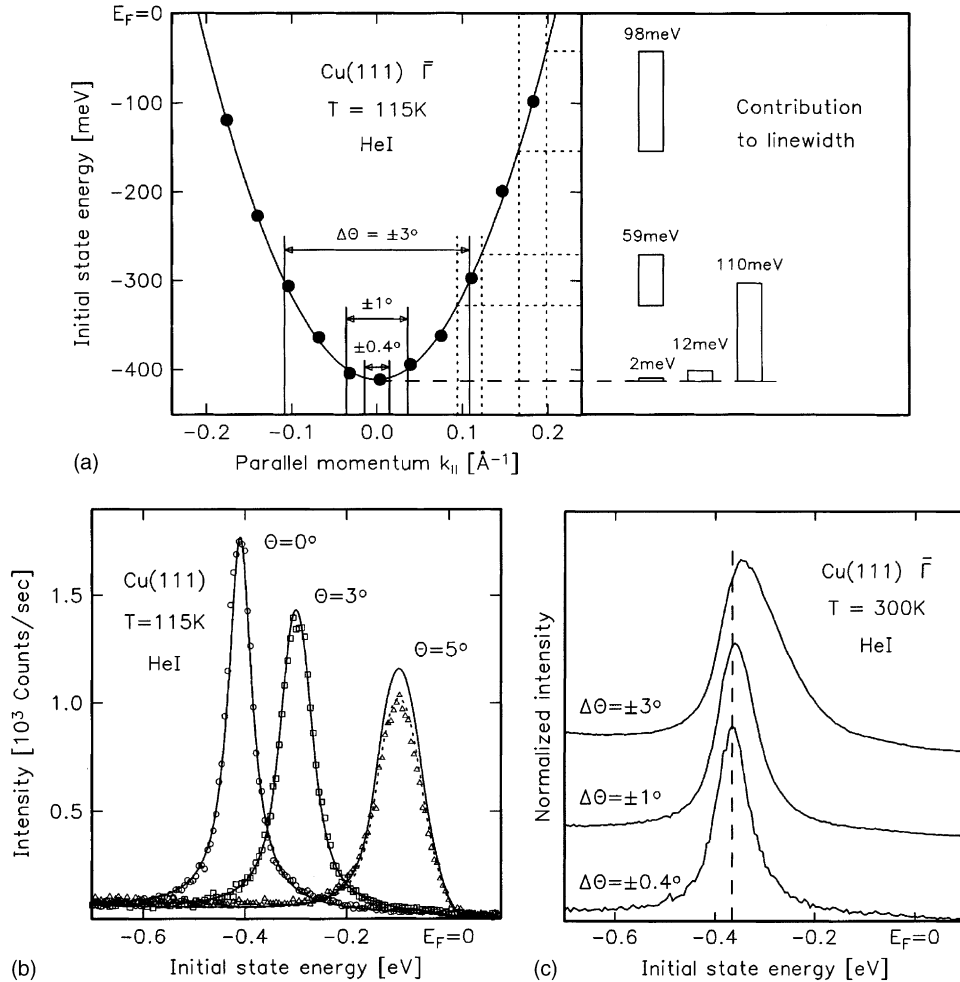
Fig. 18. (a) Parabolic dispersion $E_i(k_\parallel)$ of the Cu(1 1 1) surface state around $\bar{\Gamma}$, the center of the surface Brillouin zone. Vertical solid lines indicate the contribution of different angular resolution $\Delta\theta$ on the observed linewidth of spectra taken at $\theta = 0 (k_\parallel = 0)$. Dotted lines show the increase of broadening with increasing $k_\parallel$ due to the dispersion, at constant $\Delta\theta$. (b) Spectra taken at different θ with fixed $\Delta\theta$. Solid lines are results of a k-space integration, with the experimental dispersion from (a) and a fixed $\Delta\theta = \pm 0.4°$. (c) Spectra taken at normal emission with different $\Delta\theta$ as indicated. All data collected at $\hbar\omega = 21.2$ eV. From Ref. [27].

vertical solid lines. As is evident, with increasing $\Delta\theta$ the experiment integrates over increasing areas of the dispersion curve, with the resulting energy broadening of the emission peak shown by boxes on the right. Similarly data taken at constant $\Delta\theta = \pm 0.4°$ lead to a significant increase of the linewidth with increasing $|k_\parallel|$. This is shown by vertical dotted lines and corresponding boxes on the right. Experimental verification is reproduced in Fig. 18b which shows data points taken at three different emission angles and calculated peak shapes (solid lines) [27] based on the assumption that $\Delta\theta$ is the dominant source of broadening. Similarly Fig. 18c shows normal emission spectra (solid lines) taken at different experimental resolution. The effect of angular integration is clearly seen. Besides a shift of the resulting peak maximum at $\Delta\theta = \pm 3°$, we clearly observe an asymmetric broadening even at $\Delta\theta = \pm 0.4°$. We conclude that the resolution is still insufficient to identify the hole linewidth directly with the experimental FWHM. Similar studies have been reported for the $\bar{\Gamma}$ surface state on Ag(1 1 1) in Ref. [116] showing the substantial influence of $\Delta\theta$ on peak widths from rapidly dispersing surface states. The effect of a finite energy resolution can be controlled similarly by an experimental variation of ΔE.

To improve the angular resolution McDougall et al. [99] used very narrow entrance slits, which limit $\Delta\theta$ in direction of the surface-state dispersion to $\Delta\theta = \pm 0.06°$. Their normal emission results are reproduced in Fig. 19 for different sample temperatures. At $T = 137$ K the Shockley state emission is observed near 0.4 eV below E_F, the doublet structure (additional peak near 0.6 eV) results from the doublet line of the photon source ($\hbar\omega = 11.83$ and 11.62 eV from an ArI discharge). In the off-normal spectra (not shown) the width at fixed T increases by less than 5 meV. This indicates that the linewidth is not significantly influenced by $\Delta\theta$. This fact is also reflected in the absence of a significant peak asymmetry. The authors conclude that the experimental contribution of both $\Delta\theta$ and ΔE to the observed linewidth is ≤ 5 meV [99]. However, Fig. 19 shows a very clear dependence of measured width Γ on temperature. Γ increases linearly with T between 30 K ($\Gamma = 33$ meV) and 625 K ($\Gamma = 75$ meV). Simultaneously the peak maximum, i.e. the bottom energy of the parabola, also shifts almost linearly with T closer to E_F. The latter effect is also observed for the Shockley-states at $\bar{\Gamma}$ on Ag(1 1 1) and Au(1 1 1) and can be traced back quantitatively to the temperature-dependent shift (due to the lattice expansion) of the relevant bulk band gaps which support these surface states [116]. The observed increase in linewidth results from the contribution of Γ_{ep}, see Eq. (46). Except near $T \to 0$ this broadening can be described approximately [99] by Eq. (40) $\Gamma_{ep} = 2\pi\lambda k_B T$, with an experimental value $\lambda = 0.14 \pm 0.02$ for the electron–phonon mass enhancement parameter. For a theoretical treatment see the discussion in Section 2.5. The authors also report a substantial (≈ 10 meV) variation of widths as a function of position (of the light spot focused to 150 μm) on the sample. This is a clear indication that also the sample imperfections may contribute at "unfavorable" spots on the surface. From $\Gamma = 30$ meV at 30 K the data of McDougall et al. can be extrapolated to 0 K in order to exclude the unavoidable phonon excitation at $T = 0$. This results in (as usual in photoemission an upper limit estimate of) $\Gamma_{ee} \leq 22$ meV.

Another approach to study Γ_{def}, i.e. the influence of defects on linewidth, has been reported by Theilmann et al. [86]. By combination of high-resolution photoemission data and linewidth analysis of low-energy electron diffraction spots a semiquantitative understanding of how disorder broadens photoemission peaks could be obtained. In this case disorder was induced by argon-ion bombardment and subsequent insufficient annealing and a linear correlation was observed between the photoemission peak width and the FWHM of the LEED spots. This allows an extrapolation to "perfectly" ordered surfaces. Moreover, experimental evidence was found that the disorder-induced broadening is dominated by defect scattering of the photohole and is inversely proportional to the effective mass of
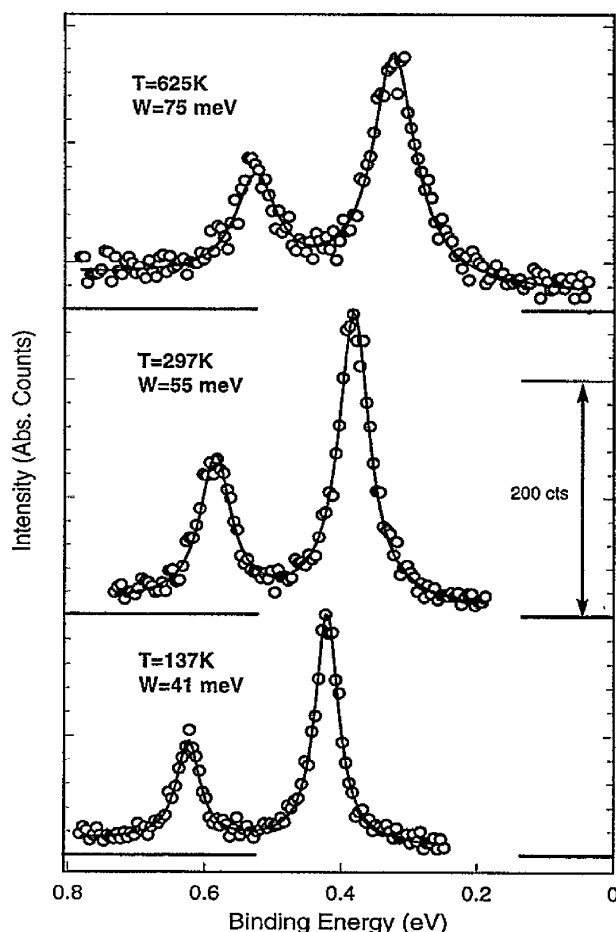
Fig. 19. Normal emission photoelectron spectra of Cu(1 1 1) obtained at different temperatures after excitation with the doublet line ($\hbar\omega = 11.83$, 11.62 eV) of an ArI discharge lamp. The spectra clearly reveal an energy shift (due to lattice expansion) and a linewidth broadening (due to electron–phonon contributions). From Ref. [99].

the surface state [86]. Extrapolation to minimal disorder and $T \rightarrow 0$ results in $\Gamma_{ee} \leq (21 \pm 5)$ meV at $\bar{\Gamma}$ on Cu(1 1 1). Surface morphology changes may also be induced by homoepitaxial growth of Cu on Cu(1 1 1), see Refs. [117,118]. A model of electron localization on terraces successfully explains energy shift and linewidth broadening [117]. Asymmetric peak broadening in photoemission of surface states resulting from lateral electron confinement has also been calculated by Beckmann et al. [119,120] for Cu(1 1 1).

The most recent results for the $\bar{\Gamma}$ states on the noble metals have been obtained with unprecedented resolution and quality by Hüfner and co-workers [100,121,122]. The breakthrough is due to the advent of "third-generation" electron energy analyzers, which allow ultra-high-resolution photoelectron spectroscopy with resolution parameters $\Delta E = 2.5$ meV and $\Delta\theta = \pm 0.15°$ as verified experimentally after excitation with monochromatized HeI radiation ($\hbar\omega = 21.22$ eV). Simultaneously photon flux and spectrometer sensitivity are sufficient to take relevant data within a few minutes with the sample at temperatures around 20 K [100,121].
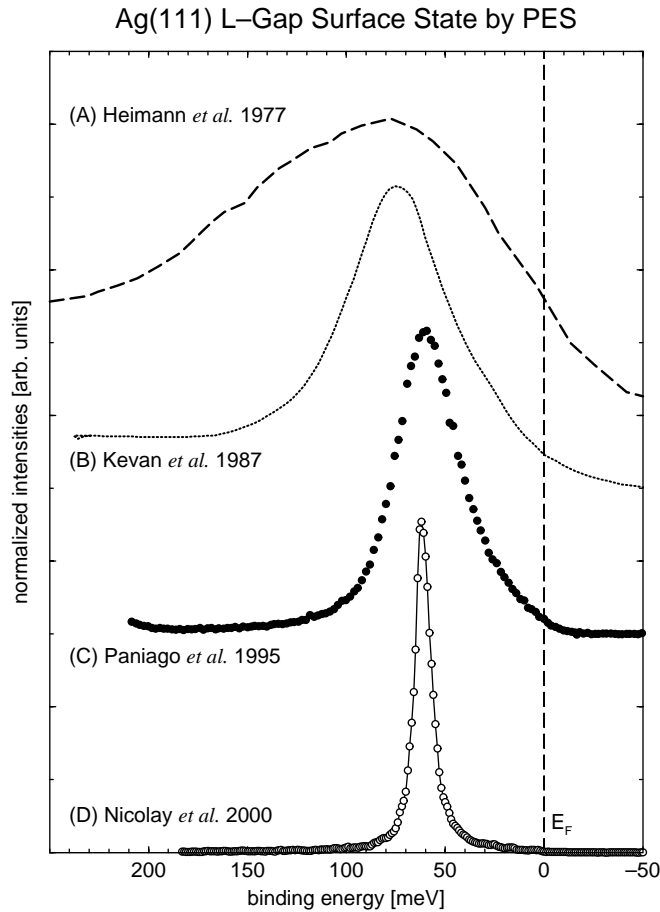
Ag(111) L–Gap Surface State by PES

Fig. 20. Photoelectron spectra taken at $\bar{\Gamma}$ from Ag(1 1 1) by different groups. The data clearly demonstrate how the relevant resolution parameters ΔE and $\Delta \theta$ improved with time in the development of photoemission. From Ref. [100].

The progress made during the last 25 years is nicely summarized in Fig. 20 as taken from Ref. [100]. It shows published normal emission spectra of the $\bar{\Gamma}$ surface state on Ag(1 1 1). The resolution parameters clearly improve from top to bottom. Spectrum A [123] was measured at room temperature with $\hbar\omega = 11.8$ eV (ArI). Spectrum B was obtained also at 300 K, but with an improved spectrometer operated at $\Delta E = 60$ meV, $\Delta \theta = 1°$ and $\hbar\omega = 13$ eV [124]. Trace C was taken at $T = 56$ K, $\Delta E = 21$ meV and $\Delta \theta = \pm 0.9°$ also after excitation with ArI radiation [116]. For this peak a careful lineshape analysis resulted in the upper-limit estimate of $\Gamma_h < 20$ meV at $T = 56$ K for the inverse lifetime of the photohole [116]. The recent progress made by Reinert et al. [100] is clearly evident in Fig. 20. From an experimentally obtained FWHM of 9 meV at 30 K the full width of the intrinsic Lorentzian $\Gamma_h = 6.2$ meV was obtained after correction for the experimental resolution function [100]. This is presently the sharpest photoemission peak observed from a metal surface. Moreover, it is in excellent agreement with the STS and STM results of Kliewer et al. [52] and Pivetta et al. [125]. The linewidth obtained with the same spectrometer for the $\bar{\Gamma}$ surface state on Cu(1 1 1) is 25.5 meV at 30 K [100]. The reason for the concomitant shortened lifetime of the photohole is due to the fact that the

binding energies at $\bar{\Gamma}$ differ drastically from $E_0 = (63 \pm 1)$ meV for Ag(1 1 1) to $E_0 = (435 \pm 1)$ meV on Cu(1 1 1). In consequence the intraband transitions filling the photohole at $\bar{\Gamma}$ are much more efficient on Cu(1 1 1) and shorten the lifetime τ_h as compared to Ag(1 1 1). This is discussed in great detail in the Section 6.1.

It is interesting to compare the most recent result for Cu(1 1 1), $\Gamma_h = (23 \pm 1)$ meV from Ref. [100], with the earlier extrapolations to optimum resolution, lowest T and "defect-free" surfaces. While $\Gamma_{ee} \leq 22$ meV is obtained from the data of McDougall et al. [99], Theilmann et al. [86] find $\Gamma_{ee} \leq (21 \pm 5)$ meV. Recent ultra-high-resolution data [95] as function of temperature allow to separate Γ_{ee} and Γ_{ep} (compare Eq. (46)). After correction for the (still) finite resolution $\Gamma_{ee} \approx 14$ meV is obtained for Cu(1 1 1) (see also Fig. 61). The earlier data extrapolated from spectra taken at worse resolution are thus consistent with the most recent results. We conclude that in particular the earlier extrapolation to "perfectly ordered" surfaces accounts for most of the defect-induced broadening. The remaining difference of about 30% might be due to single-atom defects diffusing across the terraces. This particular source for electron–defect scattering is frozen out at $T = 30$ K in the data of Ref. [100]. However, any speculation requires experimental verification.

Several years ago LaShell et al. [126] detected a particular splitting of the Shockley state around $\bar{\Gamma}$ on Au(1 1 1), which they interpreted as due to the spin-orbit interaction. Recent ultra-high-resolution data of this state [100,122] are reproduced in Fig. 21. The top panel gives the 2D Fermi surface map. The bottom panel shows a gray scale plot of the dispersion $E(k_\parallel)$ along the $\overline{\Gamma M}$-direction of the surface Brillouin zone, including (thin lines) the theoretical result from a fully relativistic density-functional calculation [122]. The observed splitting is a consequence of the lack of inversion symmetry at the surface and should therefore also be expected on Ag(1 1 1) and Cu(1 1 1). However, the calculation [122] shows the effects to be too small to be detected despite the available resolution in ΔE and $\Delta \theta$. The middle panel in Fig. 21 reproduces the momentum distribution curve at E_F, equivalent to a cut of the Fermi surface map at $k_y = 0$. It highlights again the superb resolution and allows to determine accurately the linewidth (0.38° corresponds to 0.014 Å^{-1} FWHM) at E_F.

Shockley states are also observed within the ΓL gap projected around $\bar{Y}$ on the (1 1 0) noble-metal surfaces. Only for Cu(1 1 0) a linewidth analysis has been reported [127], resulting in an upper limit for the imaginary part of the self-energy Im $\Sigma = \Gamma_h/2 \leq (16 \pm 3)$ meV. This corresponds to a photohole lifetime $\tau \geq (21 \pm 5)$ fs at $\bar{Y}$ and $T \to 0$. This has been interpreted by inelastic electron–hole interactions, with about 50% contributions each from intra-surface-band (in-plane) and 3D (coupling to substrate) decay channels [127].

In summarizing our very much shortened history of photoemission from noble-metal Shockley states we recognize the considerable development of this spectroscopy. Presently available resolution and understanding allow to separate the basic dynamical quantities Γ_{ee}, Γ_{ep} and (in favorable cases) Γ_{def} and to study their dependence on E_i, T and (in future work) on sample morphology. Any attempt to design tailored materials on the nanoscale requires a detailed understanding of Γ_{def}, since obviously not only the basic quantities Γ_{ee} and Γ_{ep} contribute to the surface dynamics, but also electron–defect scattering processes of various kinds will be unavoidable in the real world.

3.3. Tamm states on noble-metal surfaces

Tamm states split-off from d-like bulk bands exist at the $\bar{M}$ points of the surface Brillouin zone for both Cu(1 0 0) and Cu(1 1 1). For earlier studies we refer to the comprehensive data collection
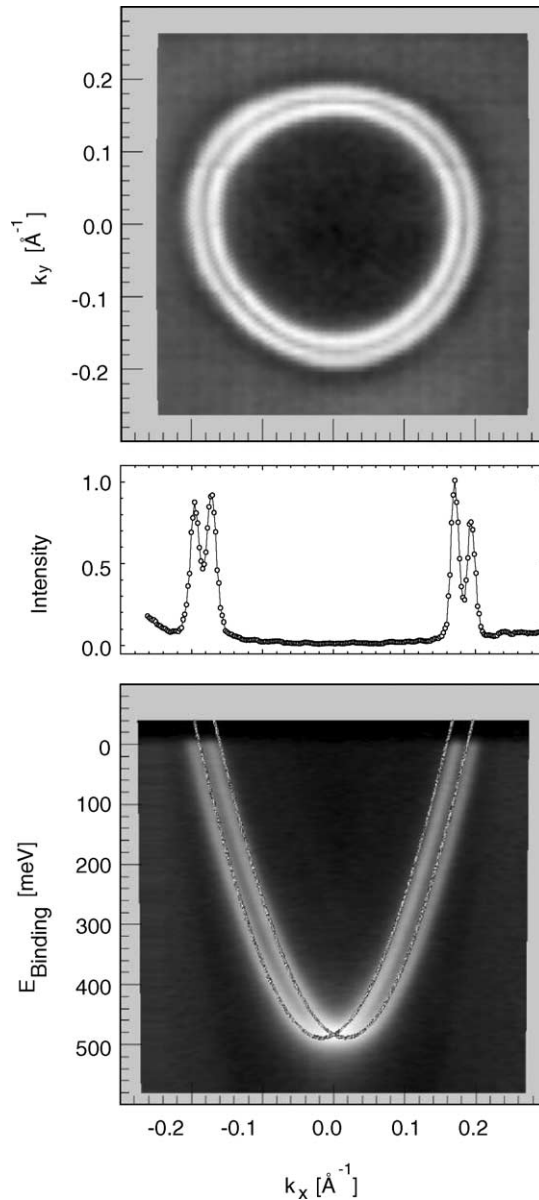
Fig. 21. Experimental results for the Shockley state around $\bar{\Gamma}(k_x = k_y = 0)$ on Au(1 1 1), taken at 30 K with monochromatized HeI radiation. Upper panel: Fermi surface map. Bottom panel: dispersion $E_i(k_x)$ along $\overline{\Gamma M}$, where the gray scale plot represents the experimental data and the thin solid lines are from a band-structure calculation for a 23-layer slab of Au(1 1 1). The middle panel shows a momentum-resolved cut through the upper panel at $k_y = 0$, clearly indicating the spin-orbit splitting and the excellent resolution. From Ref. [122].

presented in Ref. [128]. Only few recent investigations focus on linewidths and we give a short summary on available results. Theilmann et al. [86] report a linear correlation between the observed photoemission linewidth at $\bar{M}$ and the width of low-energy electron diffraction peaks. This enables the

Fig. 22. Left: photoemission peak width of the Tamm-type surface state observed at $\bar{M}$ on Cu(1 0 0) in its dependence on surface disorder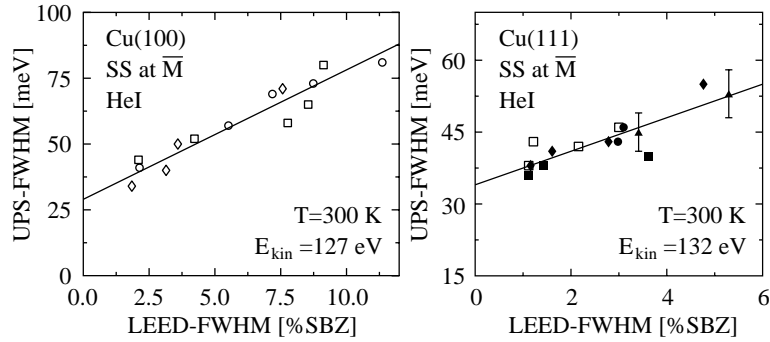 as monitored by the width of the corresponding LEED spots. Right: as left but for the Tamm state at $\bar{M}$ on Cu(1 1 1). From Ref. [86].

authors to extrapolate Γ_h to the limiting case of "perfectly" ordered surfaces. Results obtained at 300 K on both Cu(1 0 0) and Cu(1 1 1) are reproduced in Fig. 22. As is obvious, the two Tamm states respond quantitatively similar to disorder, the slope of both curves is of comparable magnitude. In contrast, the slope of the corresponding plot for the s–p-like $\bar{\Gamma}$ state on Cu(1 1 1), not shown here, is larger by a factor 6.9 ± 0.7 [86] which agrees perfectly with the effective mass ratio $m^*(\bar{\Gamma})/m^*(\bar{M}) = 7.0 \pm 0.5$ [86]. These data therefore give an independent confirmation of the result presented earlier that $k_\parallel$-integration is the dominant effect of disorder with respect to the photoemission linewidth. A more detailed understanding is expected from time-resolved two-photon photoemission (see Section 5), because this spectroscopy can distinguish in favorable cases between energy- and phase-relaxation processes. In contrast, one-photon photoemission measures squared amplitudes and the phase-information is lost in general.

The temperature dependence of the linewidth for photoemission from d-like surface states has also been studied by Matzdorf et al. [129]. Observed mass enhancement factors are $\lambda = 0.09 \pm 0.02$ at $\bar{M}$ on Cu(1 0 0) and $\lambda = 0.085 \pm 0.015$ at $\bar{M}$ on Cu(1 1 1). The latter value may be compared with $\lambda = 0.14 \pm 0.02$ [99] and $\lambda = 0.137 \pm 0.015$ [129], respectively, measured for the Shockley state at $\bar{\Gamma}$ on Cu(1 1 1). All values are of comparable magnitude and indicate that the surface states at $\bar{\Gamma}$ and $\bar{M}$, despite their different orbital character and the corresponding different localization, respond similarly in their electron–phonon interaction. From the possibility to extrapolate to "zero-disorder" and to $T \rightarrow 0$ upper inverse lifetime limits were determined [86] as $\Gamma_h \leq (20 \pm 3)$ meV at $\bar{M}$ on Cu(1 1 1) and $\Gamma_h \leq (13 \pm 4)$ meV at $\bar{M}$ on Cu(1 0 0).

The $\bar{M}$ Tamm state on Cu(1 0 0) has also been investigated using ultra-high-resolution spectroscopy by Purdie et al. [130]. The result measured at 10 K with resolution parameters $\Delta E = 5$ meV and $\Delta \theta = \pm 0.5°$ is reproduced in Fig. 23. The peak has been fitted to a Lorentzian function convoluted with a Gaussian to represent ΔE. The slight asymmetry to the left and the deviation from the fit curve around -1.82 eV most probably result from the combined action of still insufficient $\Delta \theta$ and electron–defect scattering. This is due to the negative effective mass of the Tamm state, i.e. the dispersion is from $\bar{M}$ to the left in Fig. 23. One cannot exclude, however, other interpretations. For example the assumption of Lorentzian lineshape may be incorrect, if lineshape modifications due to the many-body screening of the hole are significant. The FWHM of the Lorentzian extracted from the fit (Fig. 23) is $\Gamma_h = 7$ meV,
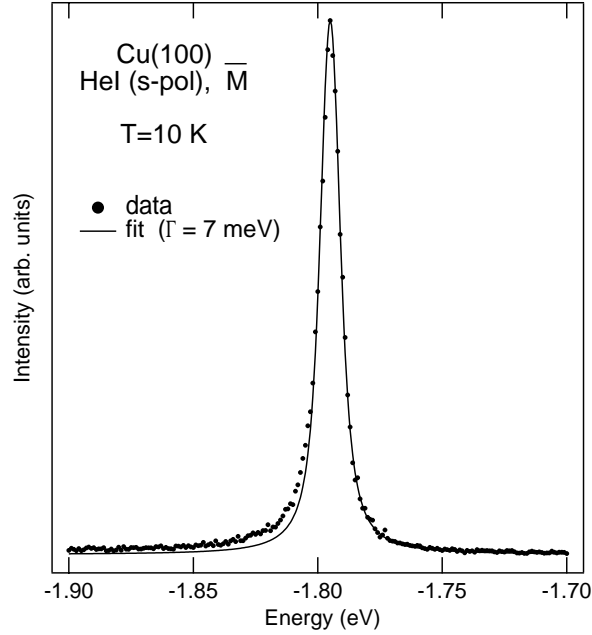
Fig. 23. Tamm state at $\bar{M}$ measured at 10 K with an energy resolution $\Delta E = 5$ meV. The fit to the data gives a Lorentzian peak of 7 meV FWHM. From Ref. [130].

corresponding to $\tau_h = 94$ fs at an initial state energy $E_i = -1.8$ eV. A similarly low value $\Gamma_h = 13$ meV was obtained by Luh et al. [131] for a d-like quantum well state resolved for atomically uniform Ag films grown on Fe(1 0 0) at about 4 eV below the Fermi level. We note that values $\Gamma_h \lesssim 20$–30 meV have also been observed at the upper edges of the bulk d-band structure, i.e. at the X-point of the corresponding Brillouin zone, both for Cu [132–134] at $E_i = -2.0$ eV and Ag [135] at $E_i = -3.7$ eV. The resulting hole lifetimes are large as compared to the Fermi-gas predictions [134–137]. This fact is explained by many-body quasiparticle GW calculations of electron–electron inelastic lifetimes of d-holes [136,137] and demonstrates clearly the important role that band-structure effects play in the hole-decay mechanism.

3.4. Other materials

Many-body and electron–electron correlation effects have also been resolved clearly for a Mo(1 1 0) surface state (see Fig. 24). Valla et al. [138] studied a d-like surface state which disperses rapidly with polar angle θ to E_F. The important observations in our context are that: (i) the photoemission peak clearly sharpens up on going towards the Fermi level and (ii) there is a small but clearly resolved change in band velocity near E_F, see the insert in Fig. 24. From peak fits of spectra, taken (a) at fixed T but varying initial state energy E_i, (b) at fixed E_i but varying T and (c) at fixed E_i and fixed T but controlled contamination with adsorbed hydrogen, the authors were able to separate the contributions from electron–electron scattering Γ_{ee}, electron scattering with phonons Γ_{ep} and electron scattering with defects Γ_{def} in their dependence of initial state energy ($E_i = E - E_F$ in Fig. 24). The most important results are summarized in Fig. 24. The experimental linewidth $\Gamma_h = 2|\text{Im }\Sigma|$ shows a minimum at E_F, a
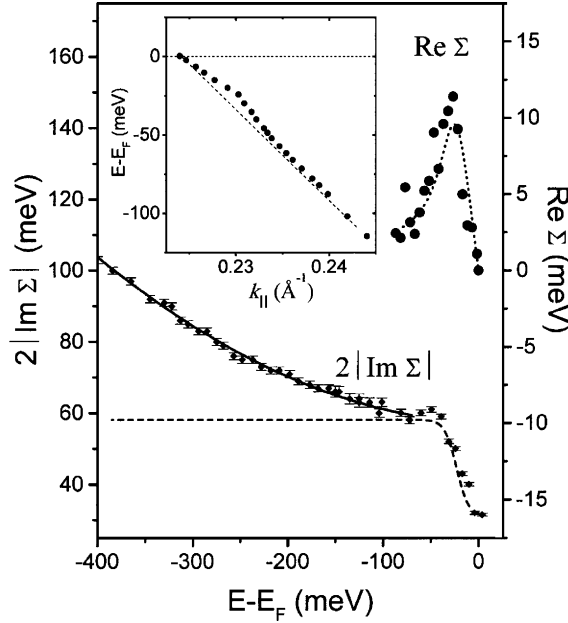
Fig. 24. Photohole self-energy for a d-like surface state on Mo(1 1 0) as a function of initial state energy ($E - E_F$) at 70 K. For details see text. From Ref. [138].

rapid increase up to $E_i \approx -40$ meV and a slower increase further away from E_F. Also shown is the real part of the quasiparticle self-energy Re Σ, which is obtained by subtracting a straight line from the experimental dispersion curve shown in the insert. This procedure gives the electron–phonon term for the real part of the self-energy [138]. The solid line through $2|\mathrm{Im}\,\Sigma|$ in Fig. 24 is a fit with quadratic energy dependence to the data between $E_i = E - E_F = -400$ meV and $E_i = -80$ meV. The dotted (dashed) line through Re Σ ($2|\mathrm{Im}\,\Sigma|$) shows the corresponding calculated electron–phonon contribution to Σ. However, to obtain agreement with the experimental data for $2|\mathrm{Im}\,\Sigma|$ the calculated (dashed) curve had to be shifted upward by a constant value of 26 meV. This difference is attributed to impurity scattering [138]. Obviously the contribution from Γ_{def} is independent of initial state energy in the present case, in agreement with the results discussed in Section 2.1. Also there is no indication that defect scattering sensitively depends on temperature. The quadratic increase of the Γ_{ee} contribution in $2|\mathrm{Im}\,\Sigma|$ with $E - E_F$ suggests a coupling of the photohole to bulk s–p-like bands. However, the analysis of the results shows the electron–electron contribution to be an order of magnitude higher than expected for s–p-derived states [138]. This observation requires further theoretical analysis with regard to intra-surface-state decay channels and possible strong coupling to the bulk s–p-bands existing nearby.

The surface states on the noble metals show weak many-particle interactions and their analysis could be performed within the quasiparticle picture, with a parabolic dispersion when crossing E_F, an essentially Lorentzian lineshape, and the corresponding inverse-lifetime width Γ of the photohole. In contrast the Mo(1 1 0) data reproduced in Fig. 24 clearly exhibit some resolved deviation from the parabolic dispersion near E_F. This is not unexpected. According to the Debye model [19] the renormalization changes the quasiparticle band mass by a factor $(1 + \lambda)$ and increases Re Σ also with increasing Debye energy (maximum phonon energy) $\hbar\omega_{\mathrm{m}}$. The relevant parameters amount to $\lambda = 0.12$

and $\hbar\omega_m = 27$ meV for Cu, but $\lambda = 0.42$ and $\hbar\omega_m = 30$ meV for Mo. Moreover, the calculations predict that ReΣ is zero at E_F, shows first a linear energy increase with a slope proportional to λ and decreases to zero again at energies further than $\hbar\omega_m$ from E_F. This is clearly observed in Fig. 24. Similar data have been reported recently for Pb(1 1 0) [139]. For more details on theory and the interpretation of Im Σ concerning the $\bar{\Gamma}$ surface states on noble metals see Section 6.1. An even larger contribution of Σ is to be expected for the surfaces of Be, where $\hbar\omega_m = 70$ meV and the coupling parameter λ on Be(0 0 0 1) is estimated between 0.7 ± 0.1 [126], 1.15 [140] and 1.18 [141,142]. Strong contribution to Γ_{ep} is indeed observed and will be discussed in the following.

The existence of a surface state around $\bar{\Gamma}$ on Be(0 0 0 1) was reported already very early in the history of photoemission. Karlsson et al. [144] observed a binding energy of 2.8 eV at $\bar{\Gamma}$ and even symmetry with respect to the mirror operation of the hexagonal surface. This state was studied in more detail by Bartynski et al. [145] and has meanwhile attracted considerable attention concerning the expected strong electron–phonon contribution near E_F. In close analogy to Cu(1 1 1) at $\bar{\Gamma}$, the surface state is located inside a wide energy gap. It is therefore not surprising that the contribution of intraband decay to the photohole inverse lifetime at $\bar{\Gamma}$ is the dominant factor and gives about 80% of the calculated total value $\Gamma_{ee} = 265$ meV [143]. The temperature-dependent experimental linewidth at $\bar{\Gamma}$ is shown in Fig. 25 [143]. The solid line is the Debye model fit and the inset shows experimental spectra exhibiting Lorentzian lineshape at different temperatures. Extrapolation to $T = 0$ gives $\Gamma_{ee} + \Gamma_{def} = (281 \pm 7)$ meV. The difference of 16 meV with respect to the computed value $\Gamma_{ee} = 265$ meV is attributed to Γ_{def}. For Cu(1 1 1) the linewidth at $\bar{\Gamma}$ was calculated to be $\Gamma_{ee} = 21.7$ meV [52] and observed with $\Gamma_{ee} = (23 \pm 1)$ meV in photoemission [100]. Two conclusions are evident: First, the calculation of intraband transition probabilities and resulting hole-decay times is
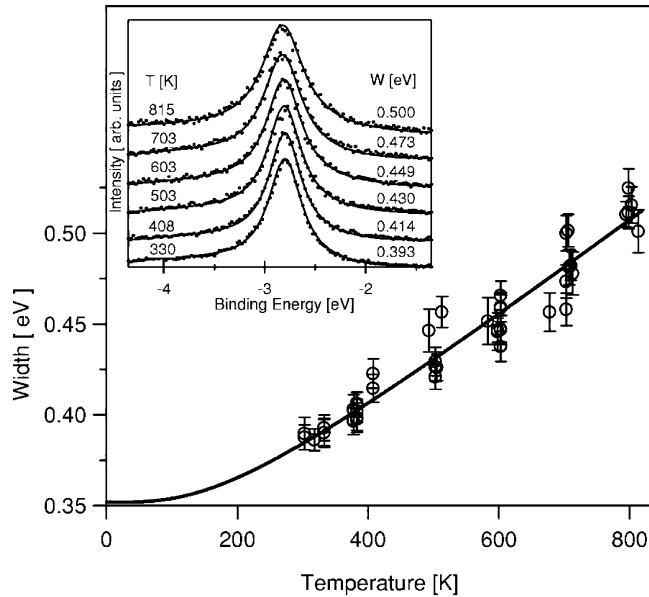

Fig. 25. Experimental surface-state linewidth W at $\bar{\Gamma}$ on Be(0 0 0 1), compare Fig. 59. The solid line is a fit using the Debye model. The insert shows experimental spectra at $\bar{\Gamma}$ for various sample temperatures (dots) and the corresponding fits using Lorentzians (solid line) plus a linear background. From Ref. [143].

meanwhile performed with great precision and confidence. Second, the large increase in Γ_{ee} for Be(0 0 0 1) as compared to Cu(1 1 1) is almost exclusively determined by the increase in binding energy at $\bar{\Gamma}$, which gives much more electrons between E_F and $\bar{\Gamma}$ to fill the $\bar{\Gamma}$ hole by intraband transitions.

As mentioned already, the electron–phonon interaction near E_F is comparatively strong in Be. Balasubramanian et al. [140] were the first to detect an unexpectedly large electron–phonon coupling parameter $\lambda = 1.15 \pm 0.10$, more than four times the bulk value of Be, and speculated on the possibility of surface superconductivity at Be(0 0 0 1). Although the authors corrected their result to $\lambda = 0.87$ in a following publication [126] this value is still large compared e.g. to the noble metals. Very high-resolution lineshape results on the $\bar{\Gamma}$ surface state were presented first by Hengsberger et al. [141,142], with data taken at $T = 12$ K and resolution parameters $\Delta E = 5$ meV and $\Delta\theta = 0.2°$ (in the direction of strong dispersion), respectively. They determine the initial state energy $E_i = -2.73$ eV at $\bar{\Gamma}$, and effective masses $m^*/m = 1.19$ (along $\overline{\Gamma M}$) and $m^*/m = 1.14$ ($\overline{\Gamma K}$). Hengsberger et al. [141,142] demonstrated that the surface state is drastically modified near E_F by the electron–phonon interaction. In particular, the lineshape near E_F is no longer a Lorentzian: as the surface state approaches E_F, a second peak appears at $E_i \approx -70$ meV. Its intensity increases strongly towards k_F, where it finally dominates the spectral function, see Fig. 26. The second quasiparticle peak is caused by the strong electron–phonon coupling. Using conventional many-body theory Hengsberger et al. [142] describe precisely this exceptional double-peak evolution of the experimental spectra. Moreover, they demonstrate that all necessary parameters can be extracted from the experiment: $\lambda = 1.18$ and $\hbar\omega_m = 70$ meV. Also a contribution of $\Gamma_{def} = 75$ meV is found, which translates into a mean free path of about 15 Å in the surface plane [142]. This value appears independent of E_i, at least up to a distance of 0.6 eV from E_F. Similar results for the $\bar{\Gamma}$ surface state on Be(0 0 0 1) have been obtained later by LaShell et al. [126]. Using a slightly different analytic approach, they obtain $\lambda = 0.7 \pm 0.1$. Their experimental data, however, agree excellently with those of Hengsberger et al. [142] where comparable. They again demonstrate that the Be(0 0 0 1) surface-state lineshape around $\bar{\Gamma}$ is progressively dominated by electron–phonon interaction when it approaches E_F. As a consequence, the description by a Lorentzian-type quasiparticle peak breaks down. As a benefit for the detailed analysis using many-body theory (in the Debye model) all relevant interaction parameters can be obtained directly from the experimental results.

Shockley-type surface states have also been resolved on the Be(1 0 $\bar{1}$ 0) surface. Balasubramanian et al. [146] determined the surface electronic band structure by angle-resolved photoemission and density-functional theory. After subtraction of Γ_{ep} the linewidth of a surface state at $\bar{A}$ ($E_i = -0.42$ eV) is determined to be 51 ± 8 meV. This is in surprisingly good agreement with the calculated total contribution $\Gamma_{ee} = 53$ meV to the total width and indicates that Γ_{def} is most probably much smaller that Γ_{ee}. Again the calculated width is completely dominated by the intraband decay rates and this demonstrates the absolute necessity to consider the very details of the surface band structure for lifetime calculations. Tang et al. [147] studied the electron–phonon coupling and the temperature-dependent energy shift of two Shockley states at $\bar{A}$ ($E_1 = -0.37$ eV, $E_2 = -2.62$ eV at room temperature) on Be(1 0 $\bar{1}$ 0). The two states shift linearly in temperature at similar rates but in opposite directions. They also exhibit different values for λ, $\lambda_1 = 0.677$ and $\lambda_2 = 0.491$. Both effects are attributed to differences in the surface charge localization [147].

So far we discussed surface states residing in wide open gaps (see Fig. 59 as an example). For these states the intraband contribution to the hole linewidth is dominant, giving typically 80% of the total
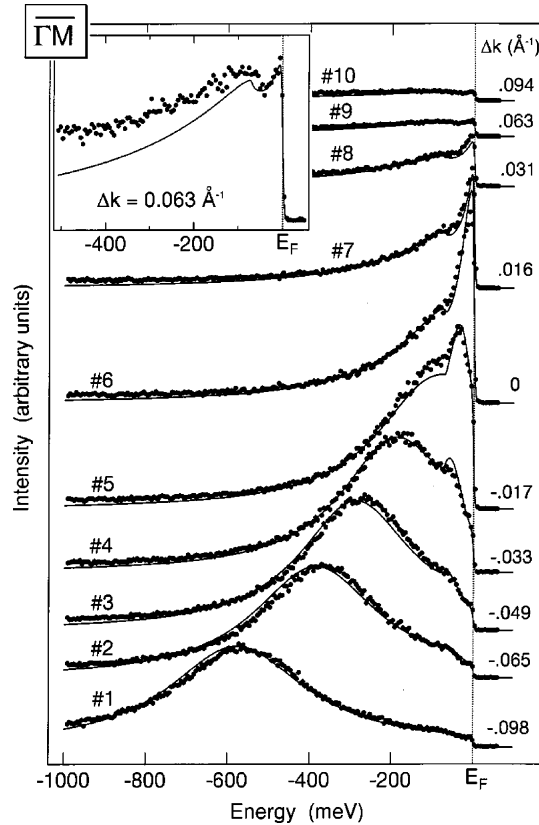
Fig. 26. Photoemission spectra of the surface state around $\bar{\Gamma}$ on Be(0 0 0 1), compare Fig. 59, along the $\overline{\Gamma M}$-direction. Solid lines through the experimental data points are the calculated spectral functions, see text for details. Sample temperature 12 K. The right column gives the wave-vector distance to the Fermi level, $\Delta k_{\parallel} = k_{\parallel} - k_F$. The 10 spectra extend over a polar angle of $6°$. The insert shows spectrum #9 enhanced in order to show the sharp peak pinned at E_F and the second structure at $\hbar\omega_m = -70$ meV. From Ref. [142].

calculated Γ_{ee}. The situation is different for metal surfaces with surface states in narrow energy gaps, where due to the close proximity of many bulk electrons the bulk contribution to the decay of a surface-state hole is dominant [53,54]. In consequence, surface-state holes in narrow band gaps decay much faster in general than surface-state holes in wide gaps if located at comparable initial state energy. Examples are Al(1 0 0) [148,149], Al(1 1 1) [149] and Mg(0 0 0 1) [53,150]. All quoted examples were studied rather early at room temperature. No temperature-dependent high-resolution studies are available to the best of our knowledge.

3.5. Overlayer and quantum well states

Quantum well states (QWS) represent another class of states localized mostly in atomic layers adjacent to the metal-vacuum interface. These states can appear in systems formed by ultrathin metal films adsorbed on metal surfaces [151–153]. If the substrate has a local band gap in the direction normal to the surface the electron can be trapped in quantum well states. Depending on the properties

of the substrate, valence electrons may be confined to the overlayer with a probability amplitude which decays exponentially into the substrate forming discrete QWS or they can be found in extended Bloch states with an enhanced amplitude within the film forming resonance QWS. The first observation of quantum well states was reported in Ref. [154] where measurements of the tunneling current from a thin metal film through an insulating oxide layer had been presented. Later QWS have been found in ultrathin metal films grown on metal substrates. Lindgren and Walldén discovered QWS in a single monolayer of sodium on Cu(1 1 1) [155] by using photoemission spectroscopy. That was the first observation of a metal overlayer state formed in an effective potential well between a metal substrate band gap and the vacuum barrier. Since then QWS were found in many different metal overlayers of a widely varied thickness on metal substrates. Various techniques have been used to measure binding energies and dispersion of QWS. Angle-resolved photoemission spectroscopy was used to study QWS in alkali-metal overlayers on different metals [151,156,157], in silver overlayers on Fe(1 0 0) [152,158,159] and on V(1 0 0) [153,160,161]. Unoccupied QWS in overlayers have been studied with inverse photoemission [162–171] and with 2PPE spectroscopies [4,172–175].

4. Scanning tunneling techniques

Noble-metal surface states have been the focus of experimental interest for over two decades, from their initial observation by angle-resolved photoemission spectroscopy by Gartland and Slagsvold [12] through to recent studies of defect scattering and lateral confinement on surface nanostructures [176–180]. The insight obtained from photoelectron spectroscopy has been reviewed in the preceding Section 3. In this section, we discuss various approaches which are based on low-temperature scanning tunneling microscopy and spectroscopy to determine surface-state lifetimes. The ability of the STM to detect surface topology and to identify minute amounts of contamination, well below the limits of conventional surface analytical techniques, ensures that effectively defect-free surfaces can be studied. Moreover, using the spatial resolution of the STM individual nanostructures on surfaces can be addressed enabling spatially-resolved measurements of electronic lifetimes.

4.1. Surface states viewed by the scanning tunneling microscope

To large extent electrons in the Shockley surface states of metals behave like a 2D electron gas which can be scattered by defects such as steps or adsorbates. Interference of the scattered wave with an incoming wave gives rise to oscillatory variation of the local density of the surface state in the vicinity of scatterers. From scanning tunneling spectroscopy and microscopy information on the dispersion of the surfaces state, scattering phase shifts, mean free path of the electron waves and the lifetime of the surface state can be derived.

The wave functions of surface states have significant amplitude outside of a crystal, making it an ideal subject for STM which probes wave functions several Angstrom above a surface [176–178]. In particularly favorable cases, e.g. alkali-covered surfaces, surface states make up for more than 90% of the total tunneling current [181].

The most common mode of scanning tunneling spectroscopy is to record the differential conductance dI/dV of the tunneling gap, which is related to the local density of states of the sample (LDOS) [182], versus the sample bias voltage while keeping the tip-sample distance fixed. The surface-state
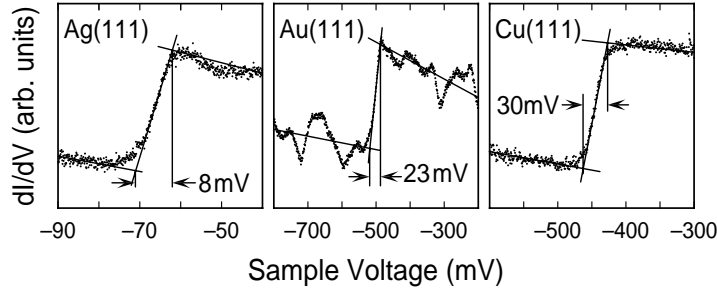
Fig. 27. dI/dV spectra for the surface states on Ag(1 1 1), Au(1 1 1) and Cu(1 1 1). All spectra were taken at least 200 Å away from impurities and are averages of different single spectra from varying sample locations and tips. In particular the Au(1 1 1) spectrum constitutes an average over 17 single spectra taken across various positions across the surface reconstruction. The width Δ of the surface-state-induced rise is defined geometrically by extrapolating the slope at the midpoint of the rise to the continuation of the conductance above and below the onset. Adapted from Ref. [52].

contribution ρ_s to the LDOS can be modeled as [183]:[1]

$$\rho_s(E) \propto \frac{1}{2} + \frac{1}{\pi} \arctan\left(\frac{E - E_0}{\Gamma/2}\right). \tag{47}$$

This has the characteristics of a quasi-2D electron gas, namely a sharp increase at the bottom of the surface-state band, E_0, and an energy-independent density of states at higher energies. The width of the band onset varies with the imaginary part of the self-energy.

Experimental data from Cu(1 1 1) which, similar to the other noble-metal (1 1 1) surfaces exhibits a surface state with parabolic dispersion, is shown in the right panel of Fig. 27. The band minimum is located at $E_0 = 445$ meV below the Fermi level [52]. A rapid rise of the conductivity occurs at the band minimum while dI/dV is approximately constant at higher energies within the band as expected from Eq. (47).

Scattering of surface states at defects affects the LDOS and thus the differential conductance of the STM junction, dI/dV, as well as its integral, the tunneling current I. Consequently, constant current images as well as maps of dI/dV may be used to study the spatial variation of surface states. Basic principles of surface-state scattering as viewed by the STM are introduced in the following along the line of Refs. [176,184]. If we assume a step along the y-direction at $x = 0$, which acts as a hard wall, then the wave function of the surface state must vanish at $x = 0$ leading to a 2D wave function:

$$\psi \propto \sin\left(k_x x\right) \exp(\mathrm{i}k_y y). \tag{48}$$

Eq. (48) can be modified to account for an energy-dependent reflectivity, including a phase shift, of the step. Any other scattering events than scattering at a step are neglected in Eq. (48).

Counting the number of states $N(E, x)$ with energies below E at a distance x from the step yields

$$N(E,x) \propto \int_{\mathrm{disk}} \mathrm{d}k_x\, \mathrm{d}k_y |\psi|^2 \propto \frac{\pi k_\parallel^2}{2}\left(1 - \frac{J_1(2k_\parallel x)}{k_\parallel x}\right). \tag{49}$$

---

[1] Found from the Green function for 2D free electrons.

The integral is over a circular disk with $\hbar^2 k_{\parallel}^2/2m^* \leq E$, where $k_{\parallel}^2 = k_x^2 + k_y^2$ and m^* is the effective mass of the surface state. The LDOS is then

$$\rho(E, x) = \frac{\mathrm{d}N(E, x)}{\mathrm{d}E} \propto 1 - J_0(2k_{\parallel}x). \tag{50}$$

J_0, J_1 are zeroth- and first-order Bessel functions, respectively, which asymptotically can be approximated as

$$J_{\mathrm{m}}(2k_{\parallel}x) \simeq \sqrt{\frac{1}{\pi k_{\parallel}x}} \cos\left(2k_{\parallel}x - (2m+1)\frac{\pi}{4}\right). \tag{51}$$

Eq. (50) describes an oscillation of the LDOS induced by the scattering at the step whose intensity falls off as $1/\sqrt{x}$. This decay reflects the fact that a range of k_x, namely those with $k_x^2 + k_y^2$ fixed, contributes to the pattern. It does not involve any other electron scattering yet. An additional, exponential damping of the scattered wave with a phase-relaxation length λ can be introduced to mimic the effect of electron–electron or electron–phonon scattering (see Section 4.3.1) [177,184].

Assuming that the coupling between the sample and an electronically featureless tip is weak, the tunnel current I is obtained from the LDOS (see e.g. Ref. [185]):

$$I \propto \int_{-\infty}^{\infty} \rho(E, x) t(E, eV, x)[f(E - eV) - f(E)] \,\mathrm{d}E. \tag{52}$$

The broadening of the Fermi edges of the tip and the sample at a given temperature T is accounted for by Fermi functions f. t is a transmission factor, e.g.

$$t(E, eV, x) = \exp\left[-z(x)\sqrt{\frac{4m}{\hbar^2}(\Phi + eV - 2E)}\right], \tag{53}$$

with Φ representing an effective tunneling barrier height which is usually approximated by the average work function of the tip and the sample. The difference of the Fermi functions of the tip and the sample effectively determines the energy range of the integral in Eq. (52). Therefore, the integration corresponds to averaging over oscillatory LDOS patterns with a range of wavelengths and represents an additional source of damping of the experimentally observed oscillations in constant-current images. Fig. 28 shows cross-sections of both a constant current and a dI/dV image of a monatomic step on Ag(1 1 1) [186]. A clear oscillatory behavior of dI/dV (Fig. 28b) is observed as expected from Eq. (50) while the constant current data (Fig. 28a and inset) display a small undulation only with $\sim$0.1Å corrugation as expected.

The effect of temperature on the standing wave patterns is two-fold. First, it enters via electron–phonon scattering and thus affects the phase coherence length L. Next, it broadens the Fermi functions of the tip and the sample. As a result, at elevated temperatures the range of the integration in Eq. (52) is enlarged and the standing wave patterns become less prominent. Nevertheless, imaging of the patterns is feasible at room temperature as demonstrated in some of the pioneering work [176,177].
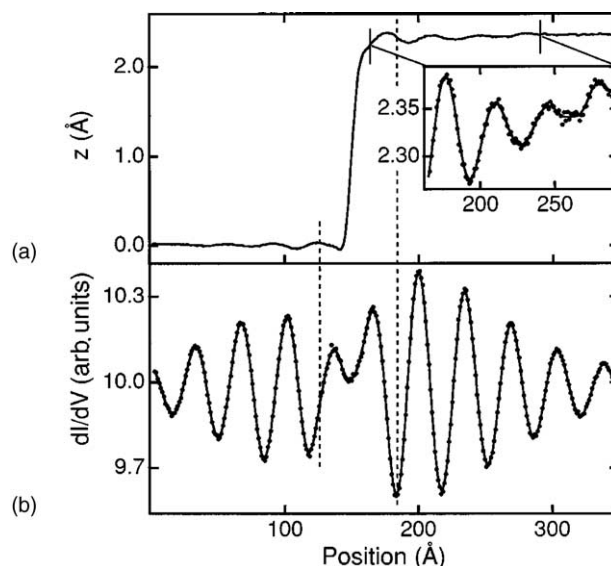
Fig. 28. Cross-sections of: (a) a constant current and (b) a dI/dV image of a monatomic step on Ag(1 1 1) acquired at $V = 20$ mV and $I = 2.0$ nA. All experimental cross-sections are obtained by averaging over 40 line scans. From Ref. [186].

4.2. Lifetimes from scanning tunneling spectroscopy

In angle-resolved photoelectron spectroscopy, lifetimes are determined from the linewidths of spectral features. It would be desirable to directly apply this concept to scanning tunneling spectroscopy and evaluate lifetimes from the widths of features in STS spectra, taking into account instrumental effects. However, STS does not offer momentum resolution and, as a consequence, addressing the lifetime of a specific state defined by its momentum $k_{\parallel}$ and energy E may seem impossible. Fortunately, as will be discussed below, this problem can be circumvented to some extent.

4.2.1. Spectroscopy of "perfect" surfaces

First measurements of electronic lifetimes τ reported by Li et al. [187] were based on an analysis of the width of the surface-state-induced rise in dI/dV tunneling spectra. As evident from Fig. 29, this width is related to the imaginary part Γ of the self-energy. As Γ increases, the onset of the surface-state contribution is seen to broaden, whilst the relative contribution of the surface state to the conductance above the onset decreases. Provided that instrumental effects, which would broaden this rise, can be neglected or corrected for, the width can be used to estimate Γ or the lifetime $\tau = \hbar/\Gamma$ of (a hole in) the surface state at the very band minimum.

For quantitative analysis the conductance was calculated within the framework of the many-body tunneling theory of Zawadowski [188] and Appelbaum and Brinkman [189]. Following Hörmandinger [190] the tip was approximated by a single atom, using a 4 eV optical potential to give a realistic spectral density. The sample Green function was calculated using multiple-scattering techniques treating the crystal within the atomic-sphere approximation [191]. Lifetime effects were incorporated via an imaginary part of a self-energy, using for the self-energy operator Γ a local constant term restricted to the sample. Results of these calculations were found to agree quantitatively with experimental data using Γ as a free parameter.
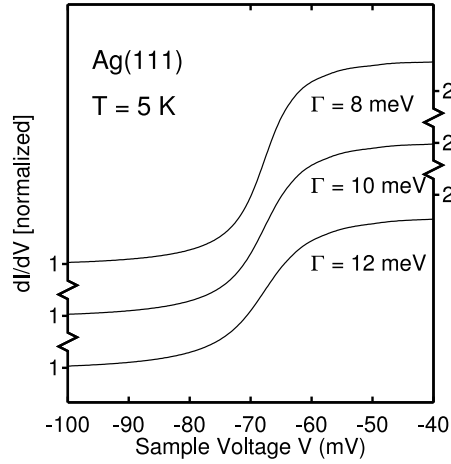
Fig. 29. Calculated dI/dV spectra for various imaginary parts Γ of the self-energy. Curves for $\Gamma = 8$ and 10 meV are offset for clarity and each is given relative to the conductance below the surface-state onset. Adapted from Ref. [187].

In addition to these calculations, Li et al. also used a simple model to establish a connection between τ and the width of the onset. To this end, Eq. (52) was used assuming that the energy and momentum dependence of the tunneling matrix elements can be neglected. This approximation is valid because in the rate of exponential decay into vacuum, both eV as in Eq. (53) and the energy associated with the momentum of the surface state are much smaller than the tunneling barrier height. The surface density of states was modeled as a constant background of bulk states at the surface plus the contribution from the surface state (cf. Eq. (47)): $\rho(E) = \rho_b + \rho_s$. A geometrical definition illustrated in Fig. 27 was adopted to quantify the width Δ, by extrapolating the slope at the midpoint of the rise to the continuation of the conductance above and below the onset. This definition of the width has the advantage of allowing an analytical treatment. In particular at 5 K, where $kT \ll \Gamma$, Li et al. obtained a linear relation between the geometrical width of the onset and the self-energy:

$$\Delta \simeq \frac{\pi}{2}\Gamma\left[1 + \mathrm{O}\left(\frac{T}{\Gamma}\right)^2\right]. \tag{54}$$

In the $T = 0$ limit the model corresponds to identifying dI/dV as ρ. Convoluting a step-like density of states with a Lorentzian of full width at half maximum Γ and then applying the same definition of the width Δ provides an alternate route to $\Delta = (\pi/2)\Gamma$. The geometrical width of the Lorentzian alone can readily be shown to be Γ, so the additional factor of $(\pi/2)$ can be identified as resulting from the distribution of states probed by the STM.

The linear relation of Eq. (54) was confirmed by the detailed calculations, but with a slope $\simeq(\pi/2)\beta$, where the small deviation of the value of β from 1 reflects the probability of the finding the electron in the barrier region where the imaginary part of the self-energy $\Gamma = 0$.

Vitali et al. suggested that the data analysis may be improved by calculating the derivative of the dI/dV data and fitting the resulting peak at E_0 with a Voigt (i.e. Lorentzian convoluted with a Gaussian) profile in order to remove the broadening introduced by the modulation used for lockin detection [192].

While this approach appears appealing it may introduce additional problems since the effect of the modulation is not appropriately described by a Gaussian [193]. Moreover, in practice different slopes of the dI/dV spectra below and above the surface-state onset are usually observed leading to extra structure in the numerical derivative the quality of which also tends to suffer from enhanced noise.

From an analysis of the data from Fig. 27, Kliewer et al. [52] arrived at lifetimes of $\tau = 120$, 35 and 27 fs for the states at the surface-state band edge on Ag, Au and Cu, respectively. For Ag(1 1 1) and Au(1 1 1) STM measures lifetimes longer by a factor of 3 than previous PES data, illustrating how large the electron-defect-scattering contribution is. For Cu(1 1 1), the situation is markedly different. In this case, the PES value was obtained by exploiting an observed correlation with low-energy electron diffraction spot profiles to extrapolate the PES linewidth to zero defect density [86]. The good agreement found here with the STM value provides evidence to support the use of this procedure for removing defect-induced broadening in PES. It is important to note that very recent PES data [100] are in excellent agreement with the lifetimes reported by Kliewer et al. [52] (see Section 3.2). Apparent remaining differences of the measured binding energies of the order of a few meV have recently been identified as being due to modifications of the electrostatic potential at the sample surface caused by the STM tip through a Stark effect, the contact potential and the modified image potential [194].

Eliminating the defect scattering contribution improved partially agreement between experiment and theory, but a significant discrepancy remained. In the absence of defect scattering, two processes limit the lifetime of the hole: inelastic electron–electron scattering and electron–phonon coupling. The importance of the phonon contribution was only recently identified [99] and used to successfully describe the temperature dependence of the linewidth of the Cu(1 1 1) surface state in terms of the electron–phonon scattering rate. Previous estimates of the electron–electron contribution have assumed the hole to be filled by interband transitions involving the bulk electrons near the surface (Fig. 30) and have calculated the decay rate using the degenerate electron-gas model of an isotropic Fermi liquid [76]. In a new treatment (see Section 2.3), both band-structure and surface effects were included to correctly describe both 2D and 3D decay processes.

For comparison with experimental values calculated electron–electron and electron–phonon contributions have to be combined to give total decay rates. The results are in good agreement with the STM data (see also Table 4), so that for the first time a consistent account was found for the hole lifetimes of the noble-metal surface states [52]. Scattering by lattice vibrations provides the dominant
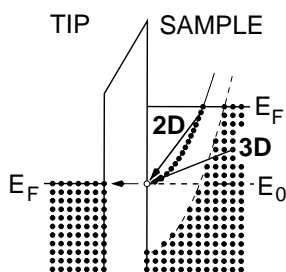
Fig. 30. Schematic energy diagram for an electron (electrons shown as filled circles) tunneling from the bottom (E_0) of an occupied surface band (solid parabola) of the sample to a metallic tip. States in the sample are displayed as a projected band structure, the dashed parabola indicating the maximum of the bulk bands. Fermi energies are denoted by E_F. The hole (empty circle) left behind by a tunneling electron is filled by an intraband transition (arrow 2D) or from a bulk state (arrow 3D). From Ref. [52].

Table 4
Energies (in eV) and linewidths (in meV) for different surface states at low temperatures

Surface state		Energy	Γ_{ee}	Γ_{ep}	Γ_{calc}	Γ_{exp}	Calculated	Experimental
Cu(1 1 1)	$\bar{\Gamma}$	−0.445	14	8	22	24	[52]	[52]
		−0.435				23 ± 1		[100]
Cu(1 1 0)	$\bar{Y}$	−0.510	8			≤ 32	[295]	[127]
Ag(1 1 1)	$\bar{\Gamma}$	−0.067	2	4	6	6, 5	[52]	[52,125]
		−0.063				6 ± 0.5		[100]
Au(1 1 1)	$\bar{\Gamma}$	−0.505	14	4	18	18	[52]	[52]
		−0.484				21 ± 1		[100]
Be(0 0 0 1)	$\bar{\Gamma}$	−2.73	265	80	345	350	[143]	[143]
Be(0 0 0 1)	$\bar{M}_1$	−1.8	72	80	152	(380)	[143]	[145]
Be(1 0 $\bar{1}$ 0)	$\bar{A}$	−0.42	53	80	133	130	[146]	[146]
		−0.39				185		[147]
Mg(0 0 0 1)	$\bar{\Gamma}$	−1.6	83	25	108	(∼500)	[53]	[150]
		−1.7				(∼200)		[144]
Al(1 0 0)	$\bar{\Gamma}$	−2.75	131	18	149	(500)	[96]	[148]
			67			(450)	[295]	[149]
Al(1 1 1)	$\bar{\Gamma}$	−4.56	336	36	372	(∼1500)	[53]	[149]
Pd(1 1 1)	$\bar{\Gamma}$	+1.35	37			(54)	[225]	[225]

The calculated values (Γ_{calc}) are decomposed in electron–electron (Γ_{ee}) and electron–phonon (Γ_{ep}) contributions. Γ_{ep} values for Cu, Ag, Au(1 1 1) and Al(1 0 0) surfaces are from microscopic calculations [95,96], other values from 3D Debye model evaluations for $T = 0$ K. Values for Γ_{exp} in parentheses were measured at room temperature.

process limiting the hole lifetimes in Ag, but for Au and Cu electron–electron scattering is most important. Moreover, the previously neglected 2D intraband transitions within the surface state represents a considerable fraction of the total linewidth (Fig. 14) and dominate the electron–electron interactions which contribute to the hole decay, screened by both s–p- and d-electron states of the underlying 3D bulk electron system. At energies above the band edge E_0 the surface-state wave function penetrates deeper into the solid and the relative importance of the 2D scattering channel is likely to decrease. This is discussed in more detail in Section 6.1.

The lineshape analysis presented above has recently been extended to alkali-covered surfaces [57] and lanthanide films [195].[2] For Na overlayers on Cu(1 1 1) STS measurements have been performed for energies below as well as above E_F [181]. Intriguingly, the binding energies of the QWS are strongly affected by the Na coverage [151]. For example, for coverages of 1 and 0.95 monolayers, binding energies of −127 and −42 meV with respect to the Fermi level were observed with scanning tunneling spectroscopy [181] confirming previous data from photoelectron spectroscopy [151] which yielded values of approximately −100 and −75 meV. For the lanthanides Lu, Ho and Gd, Bauer et al. observed nearly symmetric spectral lines (rather than bands with a sharp onset), presumably due to the large effective mass of the surface states on these surfaces [195]. A linear variation of Γ with $|E_0|$, the energetic distance from the Fermi energy, was found for both occupied and unoccupied states. In the

---

[2] Note that the simplification for $E_\perp$ given before Eq. (2) of Ref. [195] is not valid for $|m^*| \gg m$, but for $|(m^*/m)(E_0 - E)| \gg E$. The important structure in the integrand in Eq. (1) of Ref. [195] arises when E is near E_0. There the simplification may not be valid since $(m^*/m)(E_0 - E)$ is small, whilst for Ho and Gd E_0 is quite significant (see Fig. 64). It is not clear how this would affect the analysis (S. Crampin, Private communication).
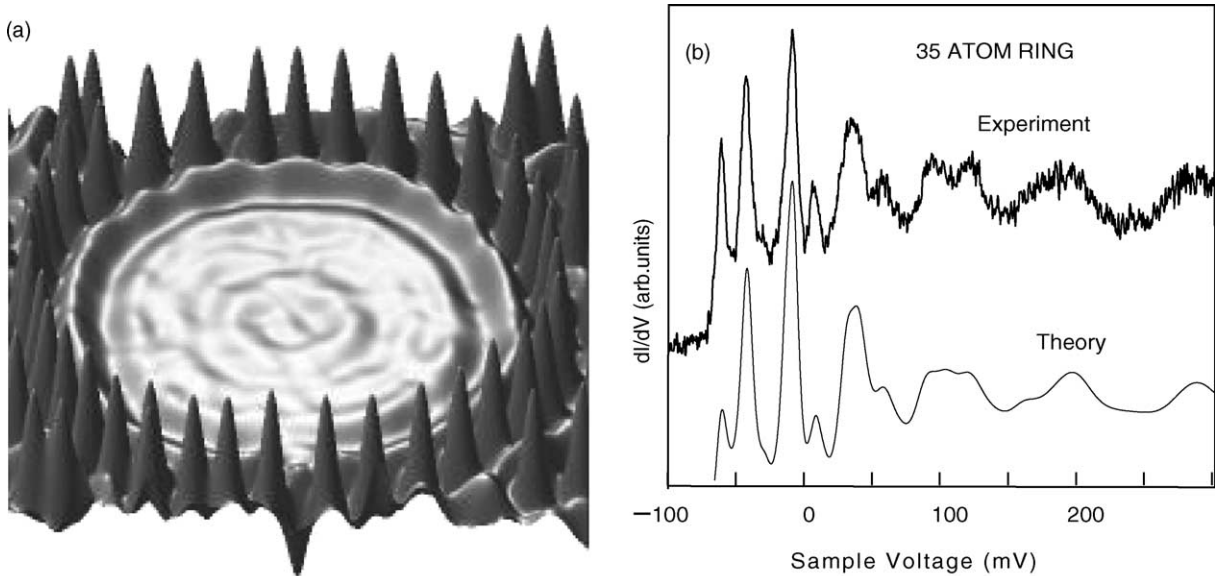
Fig. 31. (a) Circular array of 35 Mn atoms on Ag(1 1 1). Diameter ~ 22 nm. (b) dI/dV spectra from the center of the array as measured (top) and calculated (bottom). Adapted from Ref. [198].

case of the spin-split Gd surface states, which give rise to fairly broad lines with $\Gamma = 44$ meV and $\Gamma = 132$ meV for the occupied and unoccupied states, respectively, the temperature dependence of the linewidth between 10 and 160 K has been measured and analyzed by fitting the data with Lorentzians convoluted with the derivative of the Fermi function [196].

4.2.2. Spectroscopy of "quantum corrals"

The spectroscopic approach of measuring lifetimes presented above appears to be limited to electronic states at band minima (or maxima). However, this limitation can be circumvented. To this end, Kliewer et al. constructed electron resonators by laterally moving adatoms on the surface with the STM tip [197,198] (Fig. 31a).

Such resonators, first constructed and dubbed "quantum corrals" by Crommie et al. [179], exhibit electronic features over a range of energies, including the vicinity of E_F (Fig. 31b). The lineshapes of the spectral features are affected by lifetime-limiting processes so that through analysis the lifetime τ can be determined. By changing the geometry of nanoscale structures it is possible to tune the eigenstate energies of the structures and thus generate states at various energies in order to obtain the energy dependence of the lifetime.

In Ref. [198], the LDOS of the adatom arrays was calculated using a multiple-scattering technique introduced by Heller et al. [199]. The calculations were extended to include an energy-dependent lifetime of the electronic states. Since strong coupling to bulk states occurs at the adatoms [200] they were modeled as perfectly absorbing scatterers. Fig. 32 demonstrates the importance of the self energy in determining the peak amplitudes and widths in the LDOS [200,201]. The calculation for vanishing Γ, i.e. infinite lifetime, yields a series of sharp resonances (Fig. 32a, top curve). With increasing Γ there is a reduction of the peak heights and a concomitant broadening, especially apparent for the lowest of the states which have the sharpest intrinsic profile. These trends are quantified by fitting a series of
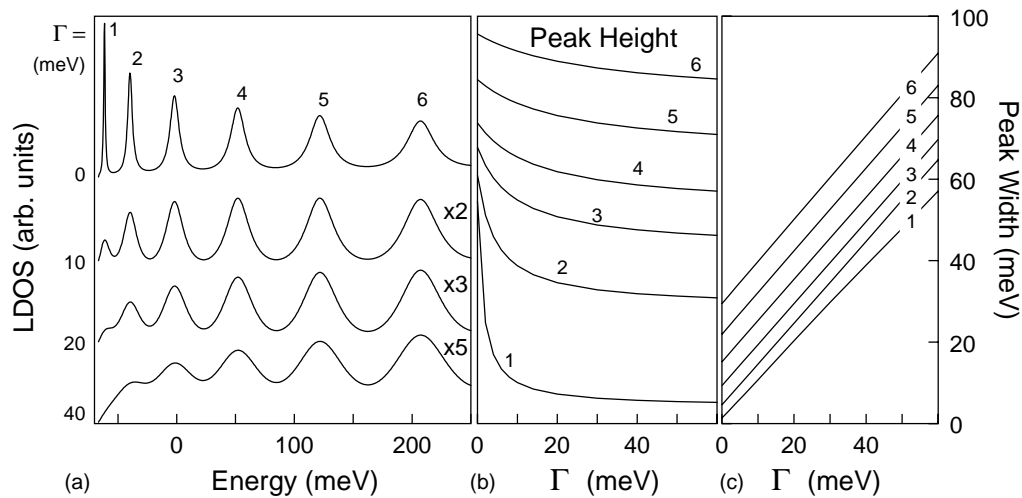
Fig. 32. Effect of a constant parameter Γ on the LDOS of a 36-atom circle with 21 nm diameter. Calculations corresponds to the center of the structure where the high symmetry gives the "cleanest" spectrum, avoiding difficulties due to overlapping resonances at off-center positions. (a) Calculated LDOS for various Γ indicated in the figure. Variation of peak (b) heights and (c) widths with Γ evaluated by fitting Lorentzians. For large Γ, owing to increased overlap of the spectral structures, the fits become less reliable for the low-energy structures and the respective width values should be taken as estimates. From Ref. [198].

Lorentzians to the data and Fig. 32b and c display the heights and widths extracted through this analysis. As Γ increases, the peak heights decrease monotonically, the lowest (in energy) peaks most rapidly, whilst there is an essentially linear dependence of the peak width on Γ.

Fig. 33 shows values of $\Gamma(E)$ obtained from an analysis of measurements from two nanostructures, 16- and 35-atom circles. Below the Fermi energy ($E = 0$) Γ approaches the value obtained previously from spectra taken on clean terraces (6 meV) [52] (Section 4.2). There is a clear increase of Γ at large energies, with $\Gamma(E = 0.5\,\text{eV}) \sim 40\,\text{meV}$, which is comparable with an extrapolation down to this energy of data for the Ag(1 1 1) surface state extracted from the spatial coherence of interference patterns at energies $E > 1\,\text{eV}$ by Bürgi et al. [202] (Section 4.3.1). Finally, at energies close to E_{F} a decrease of Γ reflects an increased lifetime of the corresponding quasiparticles (inset in Fig. 33). Increased lifetimes are indeed expected as both the phononic and electronic decay channels become less efficient. While further data close to E_{F} are needed to quantitatively characterize this effect, the first results are encouraging and may prompt theoretical investigations of electronic lifetimes in confined geometries.

4.3. Lifetimes from scanning tunneling microscopy

4.3.1. Scattering patterns at steps

As discussed in Section 4.1 the interference patterns which are observed near steps are affected by inelastic scattering processes which can be characterized by a phase-relaxation length $L(E)$. By a quantitative analysis of these patterns Bürgi et al. [202] succeeded in extracting L for surface-state electrons on Ag(1 1 1) and Cu(1 1 1) over a range of energies above the Fermi level. Fig. 34a
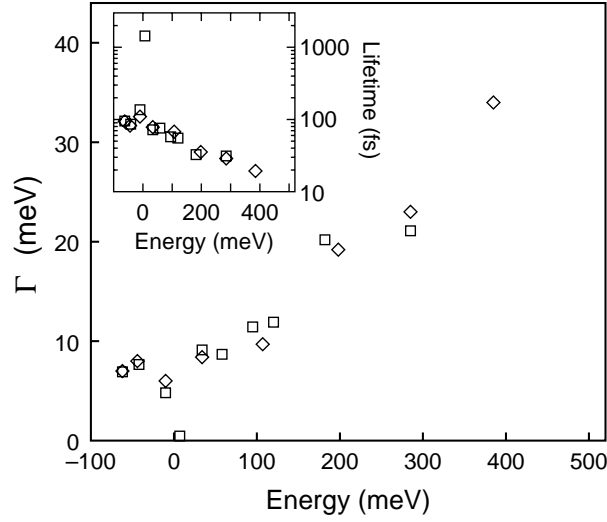
Fig. 33. Γ extracted from analysis of dI/dV spectra of a 11.5 nm radius 35-atom circular resonator (diamonds, squares) and a 4 nm radius 16-atom circular resonator. The Γ values are plotted at the position of the respective spectral features. The inset shows the equivalent lifetimes $\tau = \hbar/\Gamma$ of holes and hot electrons. Adapted from Ref. [198].
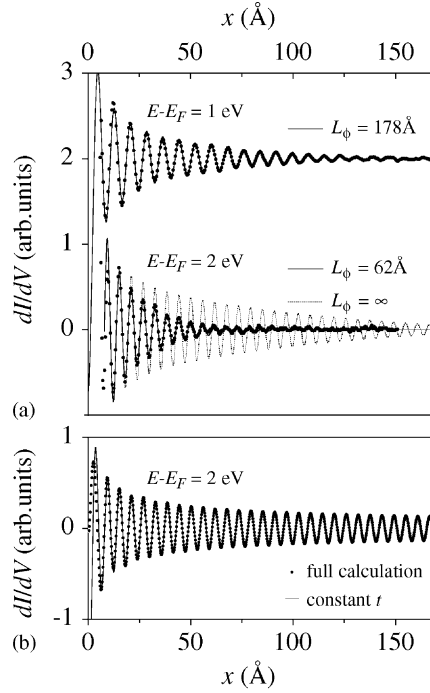

Fig. 34.   (a) dI/dV data perpendicular to a descending Cu(1 1 1) step obtained by averaging over several line scans of a dI/dV image. Solid lines indicate fits. The significance of the deduced L is demonstrated by the dotted line: neglecting inelastic processes by setting $L \to \infty$ leads to a much slower decay rate than observed. (b) Comparison between the full calculation of dI/dV with Eqs. (52) and (55) and the result obtained by setting t constant (at $T = 0$ and $L \to \infty$). From Ref. [202].

summarizes characteristic data recorded at two different sample bias voltages, 1 V (top) and 2 V (bottom), near a downward monatomic step on Cu(1 1 1). The experimental data (dots) exhibit the expected decaying oscillatory pattern. The data can be fitted well (solid lines) using Eqs. (50) and (52), where the surface-state DOS of Eq. (50) is modified to include an exponential decay:

$$\rho_s \sim 1 - r(E)\exp\left(\frac{-2x}{L}\right)J_0(2k_\parallel x), \tag{55}$$

$r(E)$ is an energy-dependent reflectivity of the step. The factor 2 in the exponent accounts for the fact that for interference at location x of the tip an electron has to travel to the step and back. The quality of the fits is obtained only for a suitable choice of the phase coherence lengths L. Neglect of L, i.e. setting $L \to \infty$ (dotted line), does not lead to an acceptable description of the data. During the fit procedure, the wave vector of the surface state $k_\parallel(E)$ was treated as an adjustable parameter. The resulting dispersion was found to agree within 10% with dispersion relations determined previously. Fig. 34b shows a calculation of the effect of the transmission factor t (see Eq. (53)) on the wave pattern. Fortunately, it turns out to be negligible at sufficiently large distances from the step edge. Thus the choice of t is not critical and it has in fact been neglected for data analysis.

To convert L to a lifetime τ, Bürgi et al. used the relation $\tau = L/v$, where $v = \hbar k/m^*$ is the group velocity. The effective mass m^* is determined from the surface-state dispersion as measured by STM [186,203] or photoelectron spectroscopy [100]. Energy-resolved lifetimes thus determined from a series of standing wave patterns are shown in Fig. 35. Given the fairly high electron energies of Fig. 35, the overall shape of the data is determined by electron–electron scattering and roughly follows a $(E - E_F)^{-2}$-law which is comparable to bulk electronic lifetimes. This lead the authors of Ref. [202] to conclude that the surface-state lifetimes are determined by scattering from bulk electronic states. It is important to note that some of the lifetimes reported, e.g. in Ref. [192], correspond to phase coherence lengths of several hundred Angstrom. Consequently, unusually large defect-free surface areas have to

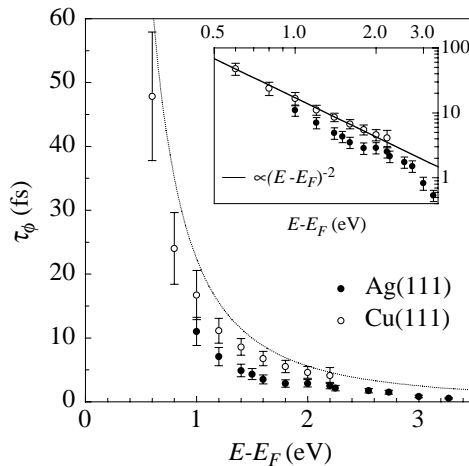Fig. 35.   Lifetimes of surface-state electrons as a function of excess energy. The dotted line indicates the lifetimes predicted by 3D Fermi liquid theory for Cu [204]: $\tau = 22.4$ fs eV^2 $(E - E_F)^{-2}$. The inset shows the same data on a double logarithmic scale. The best inverse quadratic fit to the Cu data yields $\tau = 17.1$ fs eV^2 $(E - E_F)^{-2}$ (solid line). From Ref. [202].

be used in the experiment to eliminate defect scattering. While a detailed discussion of this issue is not available, the authors of Ref. [192] reported terrace widths $\geq 2L$.

The authors of Ref. [202] note that the absolute values of the lifetimes in Fig. 35 were somewhat tip-dependent. They hint that tip wave functions which depend on the azimuthal angle (i.e. the angle in the surface plane) may effectively change the amplitude decay and thus affect the extracted lifetimes.

As discussed above, temperature causes the standing-wave patterns to decay over a shorter range. While, in principle, increased electron–phonon scattering and broadening of the Fermi levels are involved in this effect, a quantitative analysis for Ag(1 1 1) and Cu(1 1 1) shows that the Fermi-level broadening fully accounts for the temperature-induced changes of the standing-wave patterns [203]. Nevertheless, Jeandupeux et al. could establish upper limits of the surface-state linewidth at E_F [203]. For Ag(1 1 1) at $T = 5$ K, $\Gamma \lesssim 2.6$ meV was reported while for Cu(1 1 1) at $T = 77$ K, $\Gamma \lesssim 6$ meV was found.

Recently standing-wave patterns at steps have also been observed for image-potential states and good agreement with results from two-photon photoemission regarding dispersion and lifetimes has been found [205]. The asymmetry of the step reflectivity (upstairs versus downstairs) has been correlated with the asymmetry of lifetimes measured by 2PPE [206].

4.3.2. Scattering patterns in adatom arrays

A direct extension of the method discussed in the preceding section to the interesting range of lower energies close to the band bottom appears to be difficult owing to the increase of L. For large L, measuring the additional damping of the wave pattern beyond the inherent $1/\sqrt{x}$-decay is very demanding. Recently, Braun and Rieder [207] circumvented this problem by using electron resonators arranged from adatoms. Fig. 36 shows steps from the construction of a triangular resonator on Ag(1 1 1). Inside the triangle, interference leads to a fairly complex pattern while the outside pattern is similar to the scattering at a step. Braun and Rieder argue that in such a closed scattering geometry, the interference of scattered waves from many adatoms adds up to a standing wave pattern which is more sensitive to the phase coherence length than the patterns at steps.

For quantitative analysis, maps of dI/dV recorded from selected areas inside the triangle were compared to calculated LDOS patterns. The calculation was based on the multiple-scattering approach of Ref. [199]. The scattering from an adatom is characterized by a phase shift δ and an absorption α which describes the amplitude of the scattered wave. Finally, a phase coherence length L reflects scattering events inside the triangle which destroy the phase coherence. Fig. 37 shows the degree of similarity achieved by fitting the parameters δ, α and L to minimize the deviation between measured and calculated images. The fit yields average scattering parameters for absorption $\alpha = 0.43$ and phase shift $\delta = 0.24\pi$ which vary somewhat with energy. The extracted values of L were converted to lifetimes using $\tau = L/v$ leading to Fig. 38. At the bottom of the surface-state band, the lifetime agrees with previous values from STS [52] (Section 4.2.1) and recent photoelectron spectroscopy results [100] (Section 3.2). There is further encouraging qualitative similarity with the data of Ref. [198] in Fig. 33. The lifetime is drastically enhanced close to E_F as expected due to decreased phase space for electron–electron and electron–phonon scattering. The absolute lifetimes of Ref. [198], however, are generally somewhat smaller than the data by Braun and Rieder. An extrapolation of the results of Ref. [202] (Section 4.3.1) at $E - E_F > 1$ eV to the lower energies of Fig. 38 reveals that both data sets appear to be consistent far from E_F. In addition to these general trends the authors of Ref. [207] discuss edge-like features at 65 and 300 meV. The latter is attributed to a change of the surface state into a surface
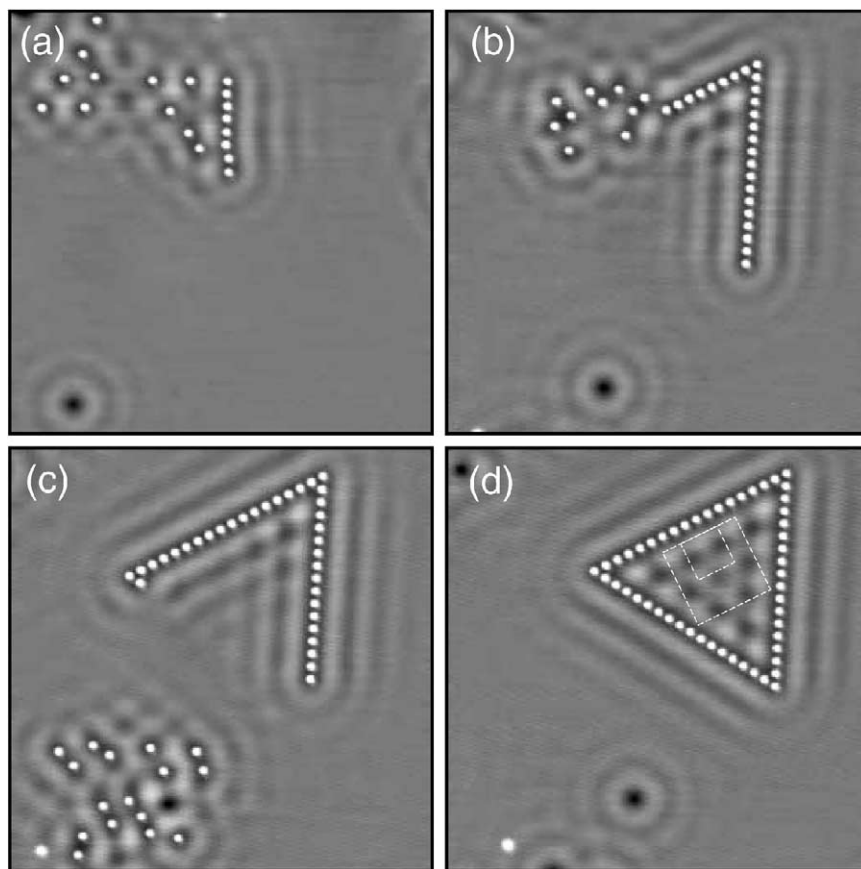
Fig. 36. Series of images showing the construction of the triangle consisting of 51 Ag atoms on a Ag(1 1 1) surface (49.3 nm × 49.3 nm, $V = +39$ mV, $I = 1.1$ nA). From Ref. [207].

resonance. The former is interpreted in terms of a change of the scattering probability as the electron energy exceeds the surface-state binding energy $E_0 \sim -65$ meV. Finally, additional fine structure in Fig. 38 is tentatively attributed to the specific electronic structure of the triangle.

While the qualitative trends in Fig. 38 agree with previous data and expectations, the lifetime reported at E_F is astonishingly long. Conversion to a linewidth leads to $\Gamma \approx 0.04$ meV. The interpretation of this small value is not obvious. Model calculations, however, indicate that the influence of the modulation on the extracted phase coherence length is fairly small [208].

The results discussed in this section have opened the way to new experimental investigations of electron dynamics in 2D systems which can complement k-space techniques such as ultrafast two-photon photoelectron spectroscopy. The long-standing discrepancy between experimental and theoretical values for the lifetimes of holes in the surface-state electron bands on noble-metal surfaces has been resolved. The experimental approaches developed can be extended to study adsorbed atoms, alloys and thin films including magnetic multilayers, systems which raise interesting questions concerning electronic coupling and the effects of disorder.
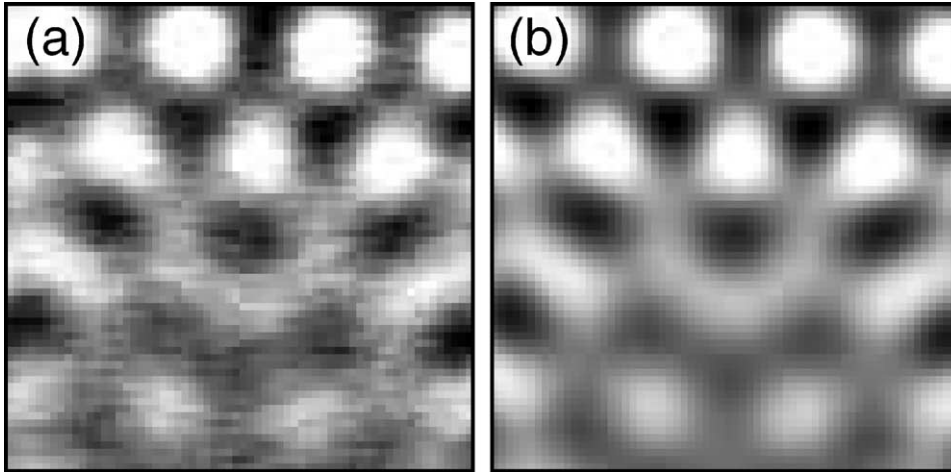
Fig. 37. (a) dI/dV data taken in the smaller rectangle of Fig. 36d at $V = +0.7$ V. (b) Calculated image for optimized adjustable parameters (see text). From Ref. [207].
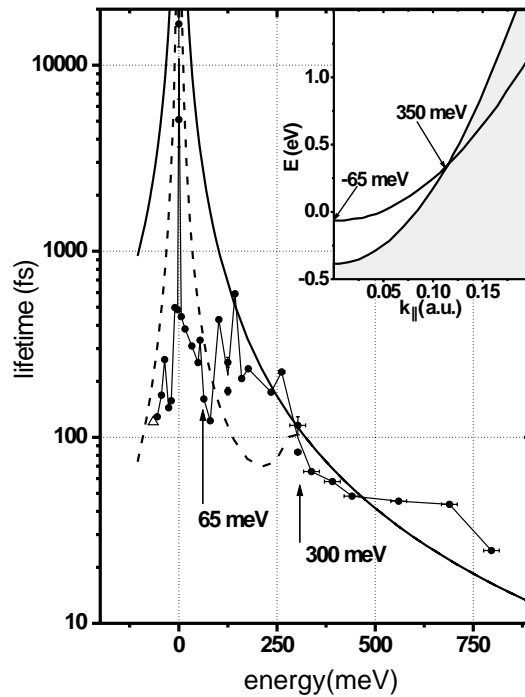
Fig. 38. Lifetimes evaluated from a triangular Ag adatom array on Ag(1 1 1) (dots connected by straight lines). The lifetime measured at -65 meV on a defect-free terrace by tunneling spectroscopy [52] is indicated by an open triangle. The solid line extrapolates the data at $E > 1$ eV from Ref. [202]. The dashed line is derived from a calculation for Cu(1 1 1). The inset shows the dispersion with momentum $k_\parallel$ of the surface state along with the projected bulk states shown by gray area [56]. From Ref. [207].

5. Two-photon photoemission

The decay of electronic excitations at metal surfaces occurs on the time scale of femtoseconds. Laser pulses of a few femtoseconds duration can be generated conveniently with Ti:sapphire lasers [209–211] and the time delay between two laser pulses can be controlled with sub-femtosecond resolution [212]. Two-photon photoemission is the method of choice to study the decay of electronic excitations at surfaces directly in the time domain [35,213–215]. The excitation scheme of the two-photon photoemission process is shown in Fig. 39. The first photon of energy $\hbar\omega_a$ excites an electron from an occupied initial state $|i\rangle$ below the Fermi energy E_F to an intermediate state $|m\rangle$. A second photon of energy $\hbar\omega_b$ is used to lift the electron above the vacuum energy E_{vac} into the final state $|f\rangle$. The energy of the intermediate state is above E_F and usually below E_{vac} in order to avoid one-photon photoemission by choosing $\hbar\omega_a$ less than the work function $\Phi = E_{vac} - E_F$. Two-photon photoemission experiments can be done in two different modes: (i) in time-resolved measurements the time delay between the two laser pulses is scanned while the energy of the detected electrons is kept fixed (top curve in Fig. 39); (ii) for energy-resolved spectroscopy the kinetic energy of the emitted electrons is measured at fixed time delay (right curve in Fig. 39). Both modes are done at fixed photon energies. Photoemission spectra for different photon energies are used to assign spectral features to initial, intermediate, or final states. For the intermediate state also the sequence of the excitations can be determined in this way. The use of different photon energies $\hbar\omega_a \neq \hbar\omega_b$ is preferable, because the low-energy background can be reduced [4,216]. The asymmetric, shifted time-resolved 2PPE signal of a two-color experiment allows
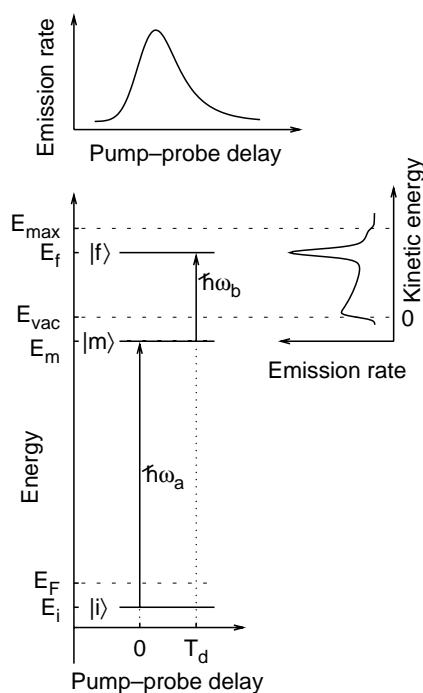

Fig. 39. Energy diagram for a two-photon-photoemission process and results of time- (top) and energy-resolved (right) measurements.
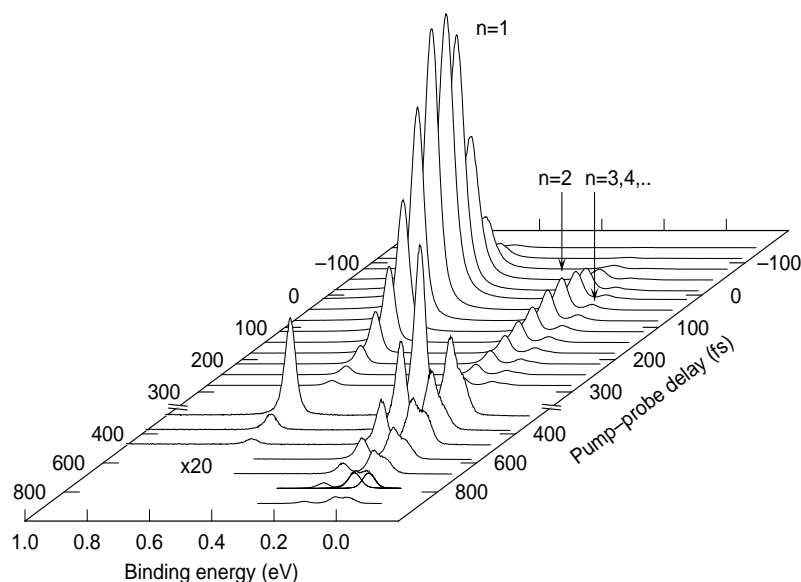
Fig. 40. Two-photon photoemission spectra of image-potential states from Cu(0 0 1) for various time delays between the pump and probe pulses. The $n = 1$ state is seen to decay rapidly. The spectra taken at large delays are dominated by the emission from the states $n \geq 2$.

for the extraction of intermediate-state lifetimes by a factor of 5 shorter than the cross-correlation [217,218]. A similar factor applies to the case of interferometric single-color experiments [175].

An overview of the results obtained from both operational modes of two-photon photoemission for image-potential states on Cu(0 0 1) is shown in Fig. 40. This set of energy-resolved spectra taken at different time delays illustrates the wealth of information which can be obtained in 2PPE experiments, just by adding another photon and the associated time delay to a photoemission experiment.

Before we are going to discuss the unique physics of 2PPE measurements, we will shortly present the experimental requirements [218–220]. The experiment basically consists of a laser system and an electron energy analyzer. For time-resolved measurements a Ti:sapphire laser provides pulses with duration down to 12 fs at photon energies around 1.5 eV. The second laser pulse is usually derived from the same laser source by harmonic generation. Apart from the short pulse duration, the main advantage of Ti:sapphire lasers is the high repetition rate around 80 MHz. This permits high count rates, because only few electrons should be emitted per pulse to avoid space-charge effects. The electrons can be detected by conventional hemispherical analyzers taking into account the rather low kinetic energies around 1 eV. The low kinetic energies permit also a time-of-flight analysis with the advantage of the simultaneous acceptance of any electron energy. However, this detection scheme requires a laser repetition rate below 1 MHz [215,221].

5.1. Lifetimes of surface states on clean metal surfaces

The spectra of Fig. 40 show that the energy position of the peaks is independent of the time delay. Therefore, it is possible to tune the energy analyzer to a fixed kinetic energy and scan the time delay. Results from such time-resolved measurements for the lowest image-potential states on a clean
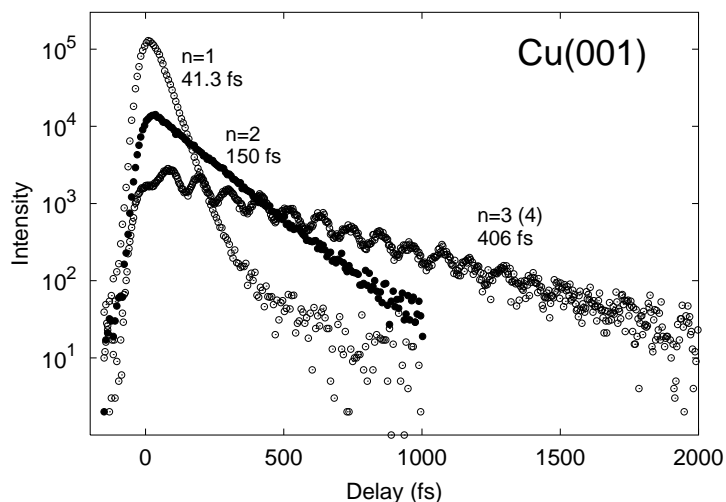
Fig. 41. Two-photon photoemission signal for the lowest image-potential states on Cu(0 0 1) as a function of pump-probe delay [222].

Cu(0 0 1) surface are shown in Fig. 41. The data are presented on a semilogarithmic scale in order to reveal the exponential decay over several orders of magnitude for long time delays. An excellent statistics is necessary to obtain the lifetime of the $n = 1$ state of 41 fs which is shorter than the cross-correlation between pump and probe pulses ($\sim$60 fs). Lifetimes down to 10 fs can be determined reliably from the shift of the signal relative to the cross-correlation or curve fitting [223,224]. The lifetimes increase strongly with quantum number n as the probability density of the image-potential state wave function is concentrated further and further away from the metal (see discussion in Section 6.2).

The spectroscopy of surface states on the (1 1 1) surfaces of noble metals has been discussed in Sections 3 and 4. These occupied surface states can be seen as initial states in 2PPE [34,226] and linewidths comparable to regular photoelectron spectroscopy are observed [4,223,227,228]. An exception among the noble-metal surfaces is Pd(1 1 1) where the intrinsic surface state is unoccupied [229]. Time-resolved measurements for the surface state and the $n = 1$ image-potential state are shown in Fig. 42. For comparison the cross-correlation obtained for the occupied surface state on Cu(1 1 1) is also shown, which has a negligible lifetime. The exponential decay for the two states on Pd(1 1 1) is observed for different signs of the time delay between the two laser pulses due to an interchanged excitation sequence for these states [225,230]. The shorter lifetime of 13 ± 3 fs for the unoccupied ($n = 0$) surface state at 1.35 eV compared to 25 ± 4 fs for the $n = 1$ image-potential state at 4.90 eV indicates a much stronger coupling to bulk bands.

Lifetimes of image-potential states have been measured with time-resolved two-photon photoemission for many clean single-crystal surfaces. For normal emission the available experimental data are compiled in Table 9 of Section 6.2 and are discussed there in conjunction with calculated values.

5.2. Momentum dependence of lifetimes

Similar to the measurement of the dispersion $E(k_\parallel)$ of occupied states with conventional photoemission, the dispersion of unoccupied states can be determined with 2PPE by detecting
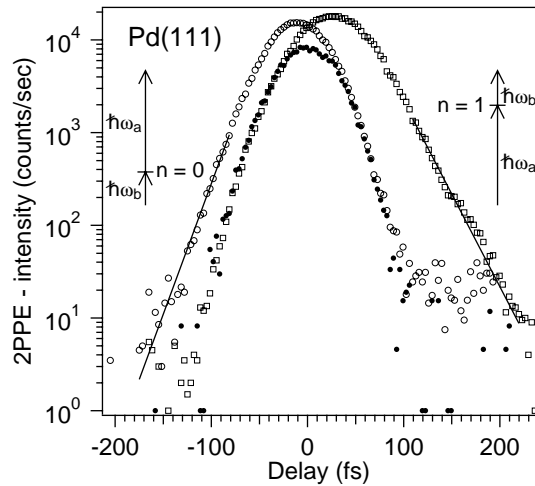
Fig. 42. Time-resolved spectra for the surface (open circles, $n = 0$) and image-potential state (open squares, $n = 1$) on Pd(1 1 1). The solid dots show the cross-correlation determined for the occupied surface state on Cu(1 1 1). Adapted from Ref. [225].

electrons emitted at different angles using Eq. (43). The combination of this capability with the pump-probe techniques can give very detailed information about momentum-dependent relaxation and scattering processes at surfaces [3]. Image-potential states on clean metal surfaces generally show a parabolic dispersion as a function of parallel momentum $k_{\parallel}$. In the case of clean Cu(1 0 0) or Ag(1 0 0) surfaces, the effective mass is close to that of a free electron. Although the image-potential state electrons move almost freely parallel to the surface their decay shows a quite pronounced dependence on parallel momentum [231].

The time-resolved 2PPE data plotted in Fig. 41 correspond to electrons emitted from the band minimum at $k_{\parallel} = 0$. With increasing parallel momentum, the lifetime of the $n = 1$ image-potential-state energy decreases from $\tau = 40$ fs at the $\bar{\Gamma}$-point ($k_{\parallel} = 0$) to $\tau = 25$ fs at $k_{\parallel} = 0.24$ Å^{-1} (Fig. 43). Two factors are responsible for this behavior (details in Section 2). First, the increase of the image-potential state energy with parallel momentum leads to increased decay to the bulk. This interband contribution is indicated as a dashed line in Fig. 44. Equally important, however, is a second decay channel that is only available to electrons with finite parallel momentum. In this process of intraband scattering the electrons remain inside the image-potential state band, but change their momentum and relax towards the band minimum. In contrast to the intraband redistribution due to phonon scattering [3] this relaxation pathway is mediated by the interaction with bulk electrons. An excited bulk electron takes up the loss of energy and momentum [231].

For delay times around 400 fs the pump-probe traces of Fig. 43 show a weak shoulder that decays with a time constant of 120–130 fs. This shoulder is partially caused by another scattering process that we mention here only briefly. By performing experiments with different photon energies of the pump pulses, it has been demonstrated that electrons excited into $n = 2$ state at $k_{\parallel} \simeq 0$ are able to scatter without appreciable energy loss into the $n = 1$ state at $k_{\parallel} \simeq 0.3$ Å [232]. This interband scattering can be mediated by defects [222,233]. Systematic studies on vicinal surfaces have shown that steps are particularly efficient sources for this resonant interband scattering between image-potential states of different quantum numbers [234,235]. Theoretically, these quasielastic scattering processes are not as
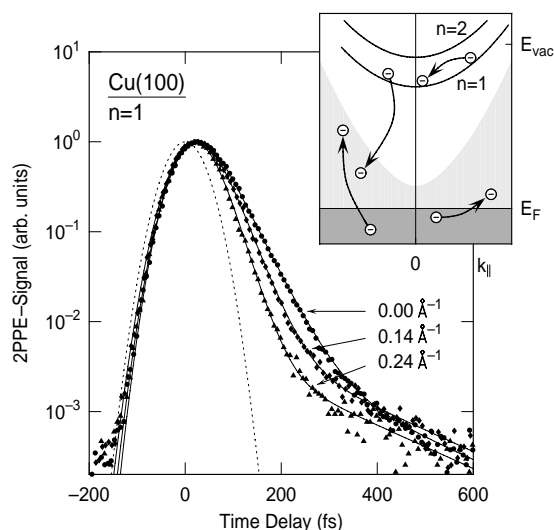
Fig. 43. Time-resolved 2PPE signal of the $n = 1$ state of Cu(1 0 0) for three different values of the parallel momentum $k_\parallel$. The two basic $k_\parallel$-dependent decay processes mediated by bulk electrons are depicted schematically in the upper right corner; left: interband decay to the bulk, right: intraband decay within the $n = 1$ band. Adapted from Ref. [231].

well understood as electron–electron scattering processes. Some progress has been made for defects [21–23], but work for steps is still lacking. Probably these scattering processes are the most important reason for the fact that the measured lifetimes of the image-potential states $n \geq 2$ in earlier work

Fig. 44. Experimental (dots) and theoretical (solid lines) decay rates of the first two image-potential states $n = 1, 2$ as a function of excitation energy $E(k_\parallel)$ above the respective band bottom. Computed decay rates without the contribution of intraband relaxation are shown as dashed lines. Inset: measured dispersion of $n = 1, 2$ parallel to the surface. From Ref. [231].

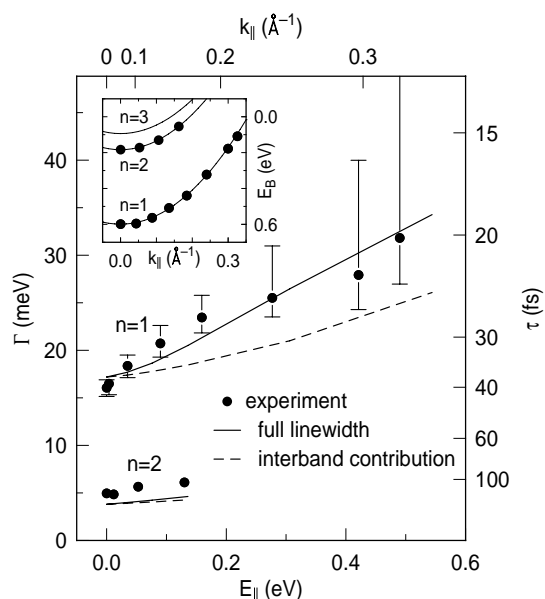[36,218] are systematically shorter than predicted theoretically (see discussion of Table 8 in Section 6.2). High-quality samples are needed to obtain longer lifetimes as shown in Fig. 41 [222]. Similar scattering events at steps and defects are also responsible for the dephasing of image-potential states as discussed below.

5.3. Quantum-beat spectroscopy

The time-dependent 2PPE intensity from the $n = 3$ state in Fig. 41 shows oscillations on top of the exponential decay which are due to quantum interference in the time domain [36]. The energy difference between the $n = 3$ and $n = 4$ states, $E_{3,4} = 34$ meV, is comparable to the bandwidth of the femtosecond pump pulses and leads to a coherent excitation of both states. The resulting beat period is $v_{3,4}^{-1} = h/E_{3,4} = 117$ fs. This 2PPE variant of quantum-beat spectroscopy permits an accurate determination of the energy differences between higher image-potential states which are very difficult to resolve in the energy domain (compare Fig. 40). An example where this has first been demonstrated is shown in Fig. 45. Pump pulses of 95 fs duration predominantly excite electrons into the $n = 4$ and the $n = 5$ states. The beating period observed for short delays is $v_{4,5}^{-1} = 230$ fs. After 2 ps most of the population in the $n = 4$ state has decayed. The oscillations now reflect the interference of the amplitudes in $n = 5$ and $n = 6$ states that persist at these delays ($v_{5,6}^{-1} = 430$ fs).

In general, the various beating frequencies can be obtained from the Fourier transform of the data with the smooth exponential decay subtracted. Numerical modeling with a density-matrix formalism involving several intermediate states allows to extract the decay time of the individual levels [36,236]. The results agree with the asymptotic n^{-3} dependence of the energy separation $E_{n,n+1}$ and inverse lifetime $\Gamma_n = \hbar/\tau_n$ (see Section 6.2) expected for hydrogen-like states. They confirm an early
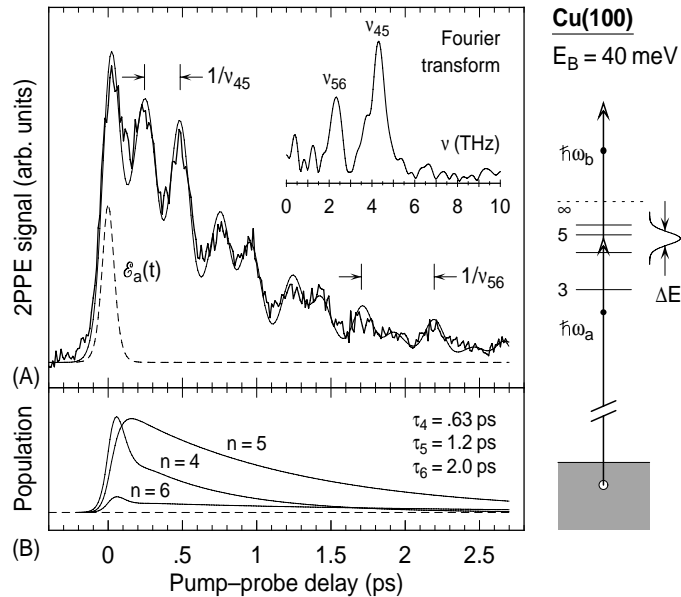

Fig. 45. Quantum beats observed after the coherent excitation of image-potential states with quantum numbers $n = 4, 5, 6$ and deduced time dependence of the relative population of these levels. From Ref. [36].
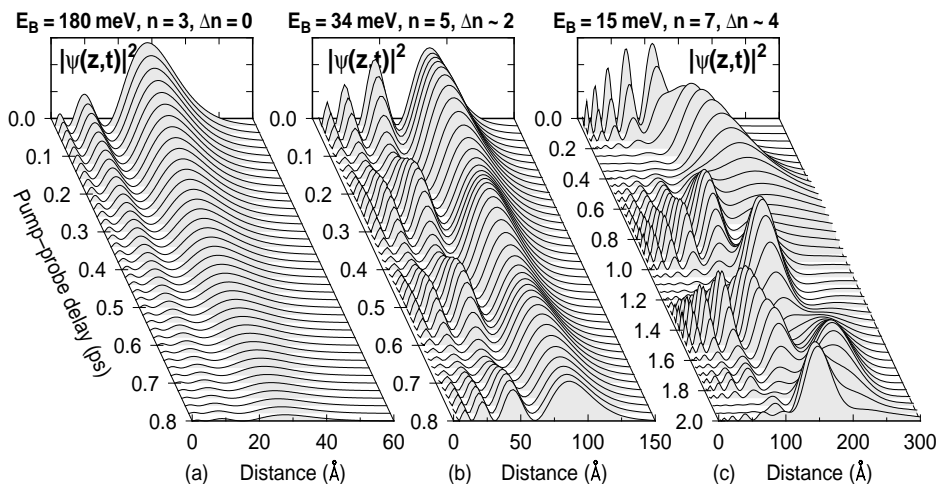
Fig. 46. Calculated temporal evolution of the vacuum probability $|\psi(z,t)|^2$ for electrons in image-potential states for three cases: (a) exponentially decaying eigenstate $n = 3$; (b) superposition of three levels in the vicinity of $n = 5$ by a 95 fs pulse; (c) superposition of image-potential states centered around $n = 7$ created by the same excitation pulse (the finite lifetime has not been taken into account).

prediction of theory [7]: if one image-potential state can be resolved experimentally, the complete series should be observable in principle.

For a better understanding of the detection of quantum beats in a 2PPE experiment it is useful to examine the temporal evolution of the excited image-potential-state wave function. Fig. 46a shows the probability density $|\psi(z,t)|^2$ of a pure $n = 3$ state (i.e. without a coherent admixture of neighboring states) as function of distance from the surface ($z = 0$) for various time delays after the excitation. The amplitude decays monotonically with a time constant of 300 fs. The situation contrasts with that corresponding to the quantum-beat experiment of Fig. 45 depicted in Fig. 46b. In this case, $|\psi(z,t)|^2$ exhibits strong temporal modulations close to the surface. This modulation is compensated by the small oscillations of $|\psi|^2$ at a distance of ~ 90 Å where the probability density is mainly concentrated. The photoemission process probes $|\psi|^2$ close to the surface because there the contribution to the matrix element is strongest. As a consequence, the 2PPE signal oscillates as function of pump-probe delay.

As for higher quantum numbers n the energy separation between image-potential states decreases with n^{-3}, many states will be excited with short pump pulses. Depending on the exact pulse parameters and the energy of the detected photoelectrons this can result in rather complex beat patterns. In certain limiting cases, such as the one shown in Fig. 46c, the dynamics of the created wave packet is simple. It resembles the classical motion of an electron bouncing back and forth between the vacuum and crystal barrier with a period of 800 fs [36,237]. Given the hydrogen-like wave functions of image-potential states it is relatively straightforward to show that the oscillation period of such a wave packet corresponds to that of a classical particle in a $1/z$ potential [238]. In this asymptotic limit, the n^3 dependence the of the lifetime simply originates from the n^3 dependence of the traveling time of the electron between surface and maximum elongation [239].

It should be noted in this context that the correct theoretical description of the inelastic decay of a coherent state due to electron–hole-pair excitation is considerably more complicated than that of a pure eigenstate. The density matrix that describes a coherent state not only consists of several diagonal

elements ρ_{nn} that decay with certain rates Γ_n, but also of off-diagonal elements $\rho_{nn'}$. The corresponding rates $\Gamma_{nn'}$ result in a non-exponential decay of the total population $\int dz|\psi(z,t)|^2$. Again, the classical behavior of α particle, inelastically reflected at a surface, is obtained for the situation of Fig. 46c. The probability for the image-potential state electron to excite an electron–hole pair is significant only if it is located close to the substrate.

5.4. Linewidths of image-potential states

Time-resolved measurements determine the decay rate of the population which can be directly compared to the theoretical calculations of Section 2. Energy-resolved spectra are needed to determine the energies of the peaks and the assignment to specific states. Data from a Cu(0 0 1) surface similar to Fig. 40 are shown in the inset of Fig. 47 for various pump-probe delays. Interestingly, there is a considerable change in linewidth decreasing with time delay and reaching a constant value for long delays. These observations can be explained by modeling the two-photon photoemission process in the Liouville–van-Neumann formalism [240]. The density-matrix description leads to the optical Bloch equations [241] which can be solved analytically for certain limiting cases [242,243]. The decay and dephasing rates (Γ_n and $\Gamma_{nn'}$) are introduced ad hoc into these equations without modeling the underlying microscopic scattering processes. For the one-step process of direct photoemission the linewidth contains the sum of decay and dephasing (throughout this chapter dephasing refers to pure dephasing set apart from decay) rates, which cannot be separated directly in the experiment. For the identification of the contributions of phonons or defects to the linewidth one has to vary the temperature or defect density, respectively, as discussed in Section 3.

The distinction of two-photon photoemission lies in the fact that a time-dependent population of the intermediate state is probed [242]. If the laser pulses are longer than the lifetime of the involved states the linewidth is given approximately by the sum of decay and twice the dephasing rate [243].
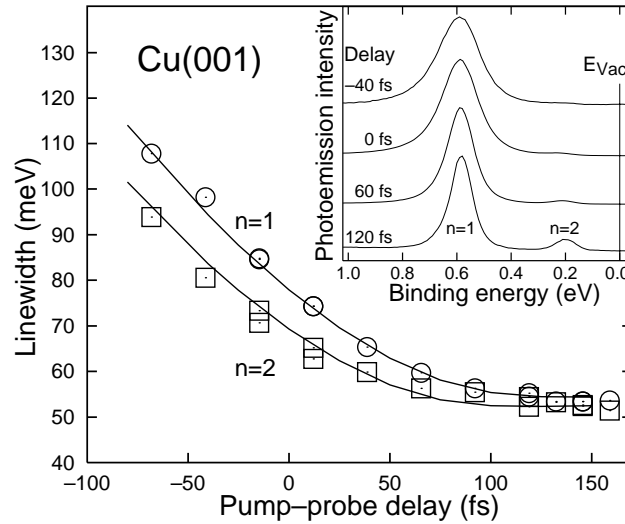
Fig. 47. Linewidth for the $n = 1$ and $n = 2$ peaks (circles and squares) from spectra as shown in inset as function of pump-probe delay compared to the results of numerical calculations. Adapted from Ref. [242].

For comparable time scales, the time dependence includes the temporal shape of the pump pulse and the decay of the excited electron, which is assumed to be exponential after the pump pulse is over. This is illustrated in Fig. 47 where calculations are compared to the data extracted from spectra as shown in the inset. The parameters decay and dephasing rates as well as the widths of pump and probe pulses match the values obtained by independent measurements [242]. One important observation concerns the linewidth for long delays which is given by the dephasing rate and spectral width of the laser pulses only. The decay rate does not contribute for Gaussian-shaped laser-pulse envelopes in two-photon photoemission [242]. This is in contrast to one-photon photoemission which proceeds from a constant initial-state population and where the spectral lineshape (Eq. (45)) is interpreted in terms of the hole lifetime. From the almost identical linewidth for both image-potential states at long delays (see Fig. 47) we can immediately deduce almost identical dephasing rates for the $n = 1$ and $n = 2$ image-potential states. The dephasing rates are negligible for the Cu(0 0 1) surface as can be seen also for the higher image-potential states by the similar decay of the average population and the oscillations in Fig. 41.

For metal surfaces with negligible amounts of impurities and defects the dephasing rate should generally be rather low as long as the overlap with bulk states is small. This reduces electron–phonon scattering which provides the only quasielastic scattering channel on a perfect surface. Electron–electron scattering with bulk or surface electrons is predominantly inelastic and described by the lifetime. For clean metal surfaces the intrinsic linewidths Γ should therefore be identical to the decay rates $\hbar/\tau$. However, the linewidths measured previously with low-repetition-rate nanosecond laser systems [4] are usually larger than the decay rates obtained from Table 9. The contributions from the bandwidth of the laser pulses can be neglected in this case. The discrepancy to the former data is therefore most likely attributable to poorer statistics and longer measurement times. The latter could lead to surface contamination which would result in dephasing. From the energy-resolved spectra associated with the time-resolved results compiled in Table 9 the intrinsic linewidth has to be determined with care, because of the effects presented in Fig. 47.

Fig. 48 shows the decay rate as a function of binding energy for the image-potential states on (1 1 1), (1 1 7) and (0 0 1) copper surfaces. Data for Cu(1 1 9) are identical to Cu(1 1 7) [244]. The image-potential-state electron is trapped between the surface and the vacuum barrier [7]. In a classical picture the electron bounces with a rate $\propto E^{3/2}$ at the surface [239]. This might lead to decay and justifies the $E^{3/2}$ dependence indicated by the dashed lines in Fig. 48. The experimental data follow this dependence quite well for low binding energies, i.e. high quantum numbers. For $n \leq 2$ the decay rates are below the expectation from the simple picture. For Cu(1 1 1) this deviation is particularly large because the $n = 1$ image-potential state is just slightly below the band edge, whereas the higher states are degenerate with bulk bands and have a correspondingly large decay rate. The two dashed lines are adjusted to the experimental data for the higher image-potential states on Cu(1 1 1) and Cu(0 0 1). These represent the extreme cases of high and low penetration of the wave function into the bulk, because the states are located just outside and in the center of the band gap, respectively [4]. Accordingly, the decay rates differ by approximately one order of magnitude. For the stepped copper surfaces Cu(1 1 7) or Cu(1 1 9) the decay rates of the higher image-potential states contain a significant contribution from the interband scattering into lower image-potential bands at the same energy but at a different momentum [234,244]. The decay due to electron–electron scattering with bulk or surface electrons would therefore be close to the Cu(0 0 1) line. This confirms that the relevant band gap for the stepped surfaces is not formed by backfolding all bands according to the reciprocal lattice vectors of the step superlattice [244].
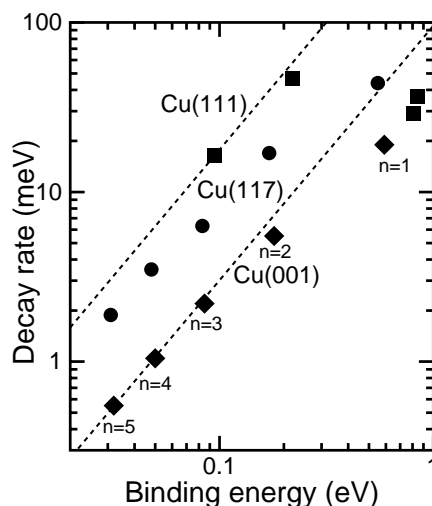
Fig. 48.   Decay rates for the image-potential states as a function of binding energy for Cu(1 1 1) (squares), Cu(1 1 7) (circles) and Cu(0 0 1) (diamonds). The dashed lines indicate an $E^{3/2}$ dependence.

5.5. Influence of defects

In the previous section we have discussed in detail the image-potential states on the clean Cu(0 0 1) surface. The decay rates are significantly higher than the dephasing rates which means that inelastic scattering with bulk (or surface) electrons is much more frequent than quasielastic scattering by phonons or defects. The small penetration of the image-potential-state wave function into the bulk explains this behavior and is confirmed by the negligible temperature dependence of lifetimes or linewidths [244] in contrast to the situation for Cu(1 1 1) with a large penetration and strong temperature effects [221].

In energy-resolved spectroscopy an increase of the linewidth of image-potential states with adsorbate coverage was observed for several systems [4,216,245,246]. However, these studies cannot distinguish between inelastic decay and quasielastic scattering induced by the adsorbates. The combination of time- and energy-resolved measurements is needed to separate the different processes for the lower image-potential states. In quantum-beat spectroscopy the decay of the population is caused by inelastic scattering, whereas the oscillations are dampened also by quasielastic scattering events which change the temporal phase of the wave functions. An example are small amounts of Cu adatoms and CO molecules on Cu(0 0 1) shown in Fig. 49 [222,224,233,239,247]. CO has almost no influence on the lifetime, but destroys the oscillations very effectively. On the other hand, a small concentration of Cu adatoms decreases the lifetime substantially. The same behavior as for the higher image-potential states shown in Fig. 49 is found for the $n = 1$ and $n = 2$ image-potential states from an analysis of time- and energy-resolved data [224,239,247]. The reason for the different behavior of Cu and CO is not completely understood yet. A good starting point for a theoretical modeling might be the distinction between attractive and repulsive scattering potentials presented by electronegative and electropositive adsorbates to the electrons in the image-potential states [23,239].

The decay and dephasing rates for different systems can be compared by looking at the ratio between these rates. Such an evaluation is shown in Fig. 50 as a function of binding energy. For the clean
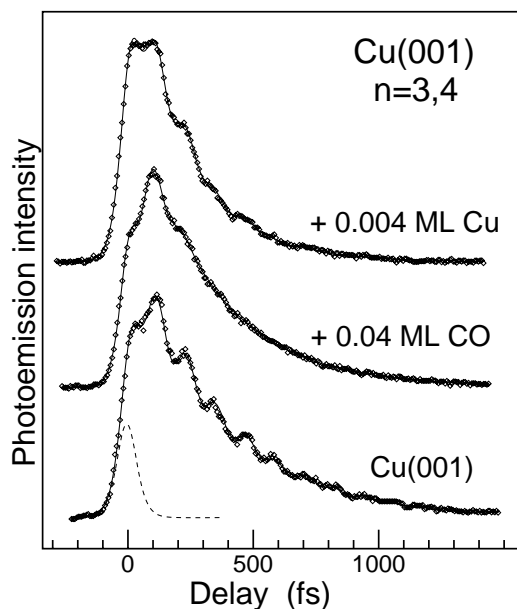
Fig. 49.   Influence of adsorbates on the quantum beats on Cu(0 0 1). From Ref. [219].

surfaces decay exceeds dephasing in all cases. For the Cu(0 0 1) surface (not shown in Fig. 50) only upper bounds for the dephasing rates can be given [244]. For Cu(1 1 1) a strong increase of the dephasing with temperature is found [221,244]. The almost equal strength of decay and dephasing for the $n = 1$ image-potential state on Cu(1 1 7) is most likely attributed to disorder in the step separation [234,235,248]. For CO and Cu on copper substrates the change of the respective rates with coverage is given. By taking the ratio any differences in coverage or morphology cancel. All adsorbate systems lead
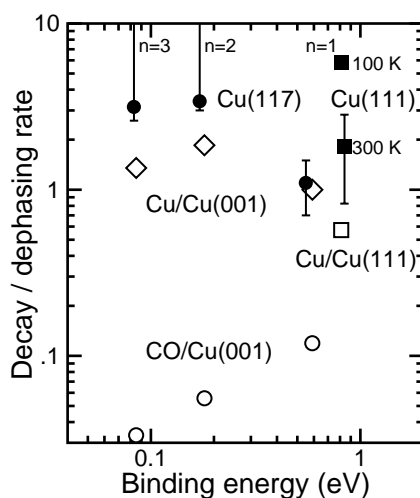
Fig. 50.   Ratio of decay rate to dephasing rate as a function of binding energy. For adsorbate-covered surfaces the change of the rates with coverage is evaluated.

Fig. 51. Linewidth (solid squares) and decay rate (open diamonds) for the $n = 1$ image-potential state as a function of CO coverage on Cu(0 0 1). The solid line shows the width of the LEED spots scaled to match the linewidth. Adapted from Ref. [224].

to a decrease of the ratio compared to the clean substrates. This indicates that disorder on the surface favors quasielastic over inelastic scattering. For Cu on Cu(0 0 1) decay is comparable or larger than dephasing, while for CO on Cu(0 0 1) dephasing dominates. Assuming that decay 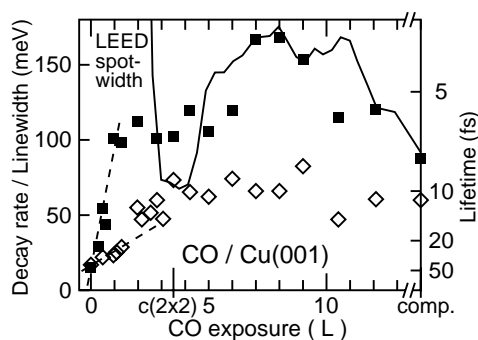and dephasing occurs by scattering events close to the surface, one would expect the ratio to be independent of the quantum number of the image-potential state. For CO on Cu(0 0 1) the ratio increases with binding energy while the opposite trend with a small variation is observed for the other systems. Further studies of other adsorbate systems and substrates are necessary to understand this behavior.

The discussion so far concentrated on low coverages of adsorbates. For higher coverages the adsorbates agglomerate in islands leading to a decrease in the number of scattering centers. For complete layers and ordered structures the quasielastic scattering by defects should be minimized as illustrated in Fig. 51 for CO on Cu(0 0 1) [224]. Minima in the linewidth are observed for the $c(2 \times 2)$ and the compression structure while the lifetime stays around 10 fs for exposures > 3 L. The sum of all scattering processes represented by the linewidth correlates well with the width of the LEED spots. In homoepitaxial growth, RHEED-like oscillations of the linewidth are found for layer-by-layer growth [247].

5.6. Decoupling by spacer layers

In the previous section, our discussion of adsorbates concentrated on their influence as isolated scattering centers for electrons in image-potential states. Well-ordered, homogeneous adsorbate layers can, of course, also drastically alter the properties of the states. For metallic overlayers the coupling of image-potential states to quantum-well states has been observed [4,249]. Of particular interest has been the decoupling of the states from the metallic substrate by insulating spacers. The possibility to increase the lifetime in this way has been crucial for recent 2PPE experiments on the dynamics of localization due to small polaron formation [250,251] and electron solvation [252–254]. Likewise, in conventional photoemission work, rare-gas layers have been employed successfully to resolve the vibrational fine structure of 2D molecular layers [255–257]. And finally, for the applicability of molecular electronic devices it may prove to be crucial to control and reduce the charge transfer between the active molecular entities and the substrate.

Image-potential states are very suitable to arrive at a quantitative description of decoupling. In the presence of adsorbates that do not introduce unoccupied electronic levels in the energy range of the
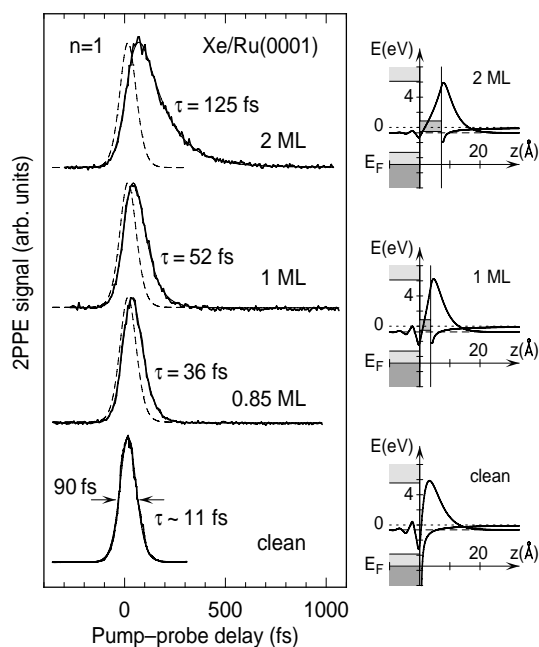
Fig. 52. Lifetime measurements of the $n = 1$ state of Ru(0 0 0 1) for various Xe coverages, schematic energy diagrams and wave functions as computed with a tunneling model. The coverage of 0.85 ML corresponds to the commensurate $(\sqrt{3} \times \sqrt{3})R30°$ superstructure, 1 and 2 ML to the incommensurate monolayer and bilayer, respectively. The dashed curves reproduce the results of the clean surface for comparison. From Ref. [267].

image-potential states, the wave functions of the latter will retain their simple hydrogenic character, but will be repelled from the metal. Systems with such properties that have been studied by time-resolved 2PPE include Xe/Ag(1 1 1) [258,259], alkanes/Ag(1 1 1) [260,261], Xe/Cu(1 1 1) [262,263], O$_2$/Xe/Cu(1 1 1) [264], N$_2$/Cu(1 1 1) [263], N$_2$/Xe/Cu(1 1 1) [263], naphthalene/Cu(1 1 1) [265], Xe/Ru(0 0 0 1) [266,267] and Ar/Cu(1 0 0) [268,269].

Data obtained for the two latter systems are shown as examples in Figs. 52 and 53. Due to the large density of states at the Fermi level the lifetime of the first image-potential state of Ru(0 0 0 1) is only 11 fs despite a larger band gap than Cu(0 0 1). It increases by more than an order of magnitude when 2 monolayers (ML) of Xe are adsorbed. Interestingly, the binding energy of the $n = 1$ state on Xe layers is not reduced much as compared to the clean surface [215,262,267]. This is partly due to the high polarizability of Xe which contributes significantly to the image potential. Additionally, the conduction band of adsorbed Xe is located well below the vacuum level, close to the $n = 1$ state. Therefore the wave function can penetrate appreciably into the Xe layers.

Argon layers represent a more clear-cut example for decoupling. There, the conduction band lies above the vacuum level and these layers provide a high barrier even for weakly bound electrons. The polarizability of Ar is by a factor of 2.5 smaller than that of Xe. Consequently, for thin layers, the binding energy of image-potential states is mainly determined by their distance from the metal surface. It decreases systematically with layer thickness whereas the lifetime increases. The longest lifetime of an image-potential state that has been measured so far with 2PPE is 10 ps for the $n = 1$ state of Cu(1 0 0) in the presence of 5 monolayers of Ar [268].
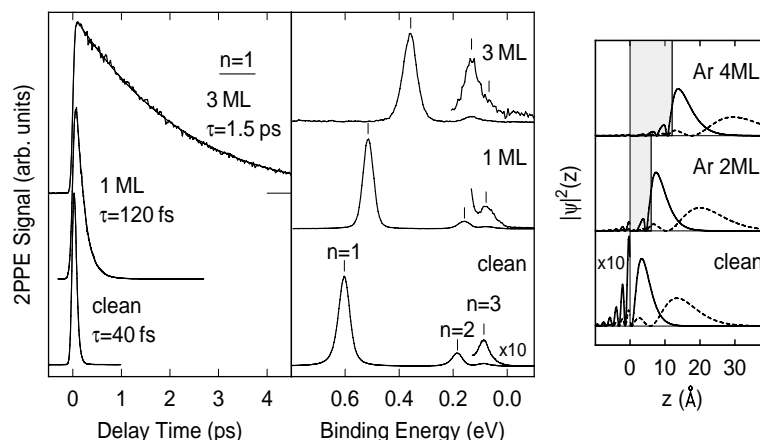
Fig. 53. Decoupling of the image-potential states of Cu(1 0 0) by 1 and 3 ML of argon. Left: pump-probe curves of the $n = 1$ state; center: 2PPE spectra; right: calculated probability densities of the $n = 1$ (solid line) and $n = 2$ (dashed line) image-potential states. From Ref. [269].

Several models have been used to describe the decoupling of image-potential states by spacer layers. The basic physics is already contained in simple dielectric continuum descriptions of the adlayers [270]. The main parameters that determine the amount of decoupling are the thickness of the layer and the position of the affinity level, i.e. the conduction band minimum, with respect to the energy of the image-potential state. In a simple tunneling picture they correspond to the width and height of a barrier and determine the penetration of the wave function [260,267]. In a more realistic description, the modification of the image potential inside and outside of the layer due to its polarizability is also taken into account [263,270,271]. If the energy levels of the image-potential states become degenerate with the conduction band of the adlayer, as it is the case for the $n = 2$ state and the rare gases Xe and Kr, the wave function of the states penetrate the layer. In this case, a quantum-well-like behavior with an oscillatory dependence of energy and lifetime as a function of layer thickness is found [272,273].

Systematic studies performed for the series of rare gases Ar, Kr and Xe adsorbed on Cu(1 0 0) at various coverages (Fig. 54) have shown, however, that a satisfactory, quantitative description of binding energies and lifetimes can only be achieved when the atomic corrugation of the potential inside the adlayers is taken into account [273]. In the case of Ar layers adsorbed on Cu(1 0 0) a full 3D potential based on ab-initio parameters has been calculated by Gauyacq and co-workers [269,274,275]. Lifetimes estimated from the penetration of the wave function into the metal by wave-packet-propagation methods were found to agree reasonably well with experiment. Many-body calculations of the inelastic decay, however, are still very demanding for such a 3D potential. For this purpose a parameterized potential that takes the atomic corrugation into account but retains the 1D character of the image-potential states is more practical [273,276].

5.7. Adsorbate states

Most adsorbate states located between the Fermi and the vacuum level are important for chemical reactions at surfaces. In the majority of systems their electronic excitations will delocalize within a few
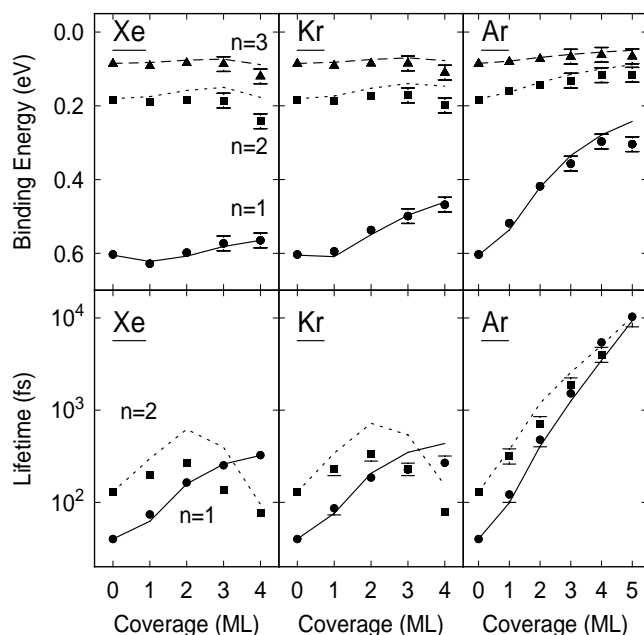
Fig. 54. Binding energies and lifetimes of the first image-potential states of Cu(1 0 0) for Xe, Kr and Ar spacer layers of various thickness. Experimental values are shown as symbols; theoretical results, calculated with a 1D atomic model potential, are drawn as thin lines. From Ref. [273].

femtoseconds or even on a sub-femtosecond timescale due to charge transfer into the metal [277–279]. With the time-resolution of present 2PPE experiments it is difficult, if not impossible, to study the dynamics of such states directly in the time domain. Only few systems with special properties have been investigated up to now. The substrate was mainly Cu(1 1 1) or Ag(1 1 1) with its large s–p-gap at the $\bar{\Gamma}$-point that extends below the Fermi level. This gap can effectively hinder resonant charge transfer between the adsorbate-induced states and the metal, just like for image-potential states. In the case of weakly bound adsorbates one can thus hope to observe sufficiently long lifetimes. Nevertheless, for the decay time of the $2\pi^*$ resonance in CO/Cu(1 1 1) only an upper limit of 5 fs could be given [280].

Longer lifetimes have been observed for the antibonding s–p-state of alkali atoms [281–285]. In particular, for Cs/Cu(1 1 1), lifetimes between 10 and 50 fs, depending on temperature have been reported [281,283] (see Fig. 55). Upon excitation of this antibonding state the Cs atom is repelled from the surface. Due to the long time it takes for the excitation to delocalize [286], the beginning of desorption could be monitored for this system. It manifests itself in a time-dependent shift of the energy of the 6s-derived state and a non-exponential decay [287,288].

A clear example for a molecular resonance with finite lifetime is provided by hexafluorobenzene (C_6F_6) adsorbed on Cu(1 1 1) [289,290]. The lowest unoccupied molecular orbital (LUMO) of the weakly bound adsorbate is located at ∼3 eV above the Fermi level [290]. Its lifetime increases as a function of coverage and reaches a value of 30 fs for 4–5 monolayers [289] (Fig. 56). In contrast, the transient electronic states observed for benzene adsorbed on Cu(1 1 1) [291,292] and Ag(1 1 1) [293] are most likely modified image-potential states. For a more detailed discussion, the reader is referred to a recent review article by Zhu [294].
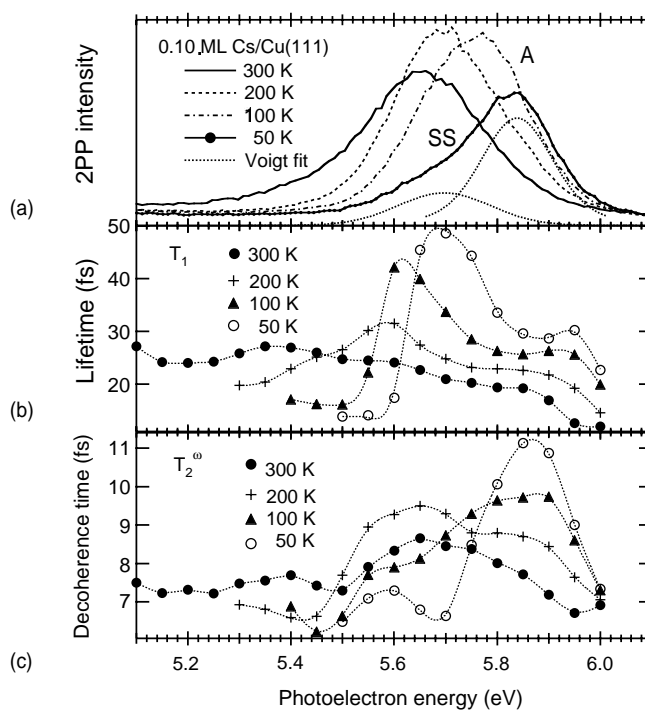
Fig. 55. Temperature-dependent 2PPE spectra (a), inelastic decay times (b) and dephasing times (c) for Cs/Cu(1 1 1) determined by interferometric cross-correlation measurements. From Ref. [281].
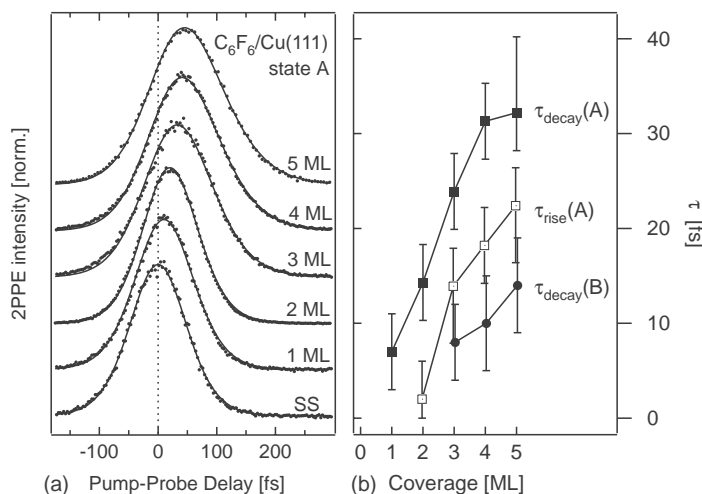

Fig. 56. Time-resolved 2PPE spectroscopy of the lowest unoccupied molecular orbital of C_6F_6 on Cu(1 1 1). From Ref. [289].

6. Comparison between theory and experiment

In this section, we complete the theoretical description of the physics of the hole and electron dynamics by comparing the results of the calculations with the experimental results of the preceding sections.

6.1. Surface states

6.1.1. Surface-state holes at $k_\parallel = 0$

The results of the calculations for several surfaces show [53,54,96] that the role of intraband transitions within the surface-state band varies from one surface to another. In particular, for surface states located in a wide energy gap, and therefore, having very clear surface character, the intraband contribution to the hole-linewidth broadening Γ_{ee} at $\bar{\Gamma}$ dominates the electronic decay. This is the case for the $\bar{\Gamma}$ surface state on Cu(1 1 1), Ag(1 1 1), Au(1 1 1) [52,53,55] and Be(0 0 0 1) [53–55,143] as well as for the $\bar{A}$ surface state of Be(1 0 $\bar{1}$ 0) [146]. In contrast, for surface states located in a narrow energy gap (examples are the $\bar{\Gamma}$ surface states on Al(1 0 0), Al(1 1 1), Mg(0 0 0 1) [53,54,96] and the $\bar{M}$ surface state on Mg(0 0 0 1) [53,54]) 3D → 2D transitions dominate and 2D → 2D transitions give only 20–30% of the full Γ_{ee}.

The calculated and experimental results for a wide variety of surfaces are collected in Table 4. There is generally very good agreement proving that all the necessary ingredients are included in the theoretical description and that the experimental methods and sample preparations are well understood and under control. The results obtained by Keyling et al. [295] disagree somewhat with recent measurements and other calculations. An explanation could be the fact that in Ref. [295] the surface screening has not been included in the calculation.

In the noble metals the d-bands lie rather deep in energy and, therefore, are not directly involved in the 2D → 2D or 3D → 2D transitions discussed in Section 2.4.3. However, d-electrons do have an impact on the inelastic decay via screening of the electron–electron interaction. Kliewer et al. [52] included this effect in the calculation of lifetimes following the approach proposed by Quinn [74] who showed that in the bulk these effects are important for excitation energies less than 1 eV. Kliewer et al. concluded that d-screening reduces the electron–electron scattering leading to better agreement with recently measured linewidths on noble-metal surfaces [52,100] (see also Tables 2 and 6).

6.1.2. Surface-state electrons and holes for $k_\parallel \neq 0$

At the (1 1 1) surfaces of noble metals the surface-state band bottom is well separated from bulk states [45,116]. For energies above E_F the surface-state band approaches the bulk band edge and enters the bulk continuum (at ∼0.45 eV for Ag(1 1 1), ∼1.08 eV for Cu(1 1 1) and ∼1.20 eV for Au(1 1 1)) losing its surface weight. This behavior is of crucial importance to understand the physics of the momentum dependence of the electron decay in the surface state [192]. The evaluation of Γ_{ee} for Ag(1 1 1) leads to a significant reduction (by a factor of 4 at $E = 0.5$ eV) of the intraband contribution [192] as the parallel momentum of the surface state increases.

In Fig. 57, we show the calculated results for Ag(1 1 1) in terms of Γ_{ee} scaled by $(E - E_F)^{-2}$ for energies from 0.1 to 1.1 eV [192]. We also display the experimental data of Kliewer et al. [198] and Vitali et al. [192]. The evaluated decay rate Γ_{ee} due to interband and intraband transitions, the electron–phonon contribution Γ_{ep} and the decay rate due to all inelastic processes $\Gamma_{total} = \Gamma_{ee} + \Gamma_{ep}$ are shown
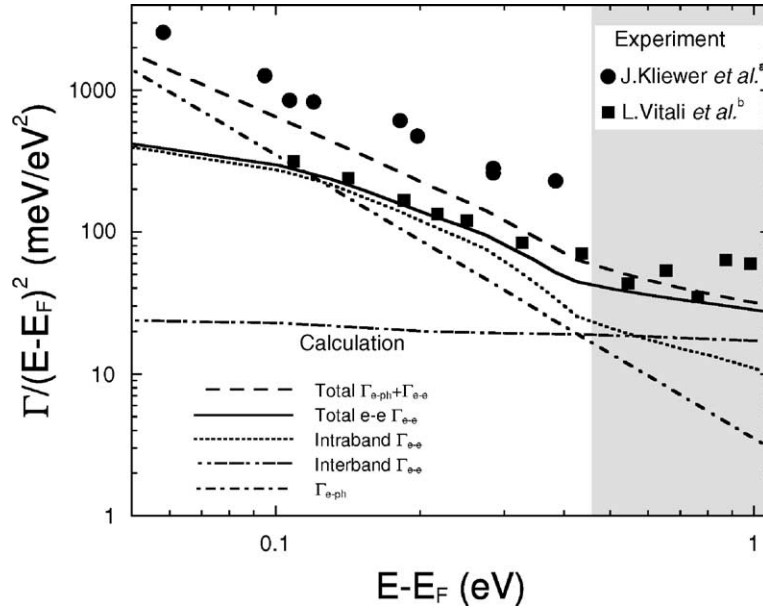
Fig. 57. Comparison between the experimental surface-state inverse lifetime Γ (solid symbols) and the calculated Γ (lines) plotted as $\Gamma/(E - E_F)^2$ vs. $(E - E_F)$ for Ag(1 1 1). The various inelastic channels contributing to the calculated $\Gamma_{ee} + \Gamma_{ep}$ (dashed line) are given in different line formats (see legend in the figure). The deviation from the quadratic behavior found at low energies is due to contributions from intraband electron–electron scattering (dotted) and electron–phonon interaction Γ_{ep} (dash-dotted). The gray shaded area of the plot marks the region where the surface state overlaps in energy with the projected bulk bands ([a] Ref. [198]; [b] Ref. [192]). Adapted from Ref. [192].

separately. In this calculation screening by the d-band was not included. For $E > 0.5$ eV the interband scattering from bulk states becomes the largest contribution, however, it still remains comparable with the intraband contribution. For high energies electron–phonon scattering becomes negligible at low temperatures. For small energies (lower than 0.35 eV) the calculated linewidths lie between the two experimental data sets. The intraband transitions and electron–phonon scattering are competitive processes at energies lower than 0.4 eV and are responsible for the deviation from the quadratic behavior. For these energies the surface state shows less bulk behavior than for higher energies.

Another example of the dependence of electron dynamics with the parallel momentum in a surface state is provided by the Cu(1 1 1) surface state. The results of the calculation of the total inelastic decay rate of Shockley surface-state electrons and holes on Cu(1 1 1) [56] are shown in Fig. 58 (solid line with circles) versus the surface-state energy. Separate interband and intraband contributions to the decay rate are also represented in this figure by solid lines with triangles (interband) and inverted triangles (intraband), and the inverse lifetime of bulk free-electrons with the same energy is represented by a dotted line. The interband decay rate shows the $(E - E_F)^{-2}$ energy dependence that is present in the case of a 3D free-electron gas. Fig. 58 shows that at the surface-state band edge ($k_\parallel = 0$) the intraband decay represents 80% of the total decay rate (see also Table 2). As the surface-state wave vector parallel to the surface increases, the surface-state wave function acquires a bulk-like character, with a larger penetration into the bulk, and the intraband contribution to the linewidth decreases very rapidly. This conclusion explains the observation that while 3D free-electron gas predictions of
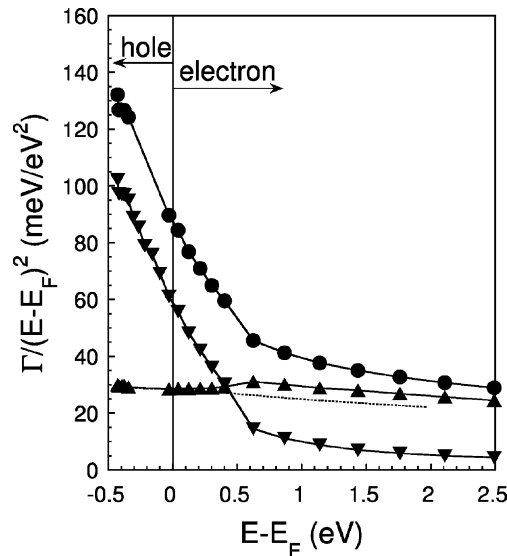
Fig. 58.   Scaled inelastic electron–electron contribution to the decay rate of Shockley surface-state electrons and holes in Cu(1 1 1), as a function of the surface-state energy. The total decay rate is represented by a solid line with circles. Intraband and interband contributions to the decay are represented by solid lines with triangles (interband) and inverted triangles (intraband). No effect due to *d*-band is included in this calculation. The 3D free-electron-gas prediction is represented by a dotted line. Adapted from Ref. [56].

surface-state hole-decay rates are too large, they are in the case of surface-state electrons (above the Fermi level) comparable to those obtained within a more sophisticated model.

No first-principle calculations have been done for noble metals so far. The only available ab-initio calculation has been realized for the Be(0 0 0 1) surface and is discussed next.

6.1.3. First-principle hole dynamics on Be(0 0 0 1)

First-principles GW calculations as described by Eq. (24) of electron (hole) dynamics in surface states take the surface corrugation fully into account, i.e. the band structure in the direction parallel to the surface. Because of their high complexity these calculations are very time consuming and only recently the first ab-initio GW evaluations have been done by Silkin et al. [143] using Be(0 0 0 1) as an example. The study of this surface is very instructive since Be(0 0 0 1) has the very clear s–p_z surface state at $\bar{\Gamma}$ (see Fig. 59) and two p_x–p_y surface states at the zone boundary, at $\bar{M}$ [60,145]. The lower $\bar{M}_2$ state at the gap edge is very bulk-like compared to the $\bar{\Gamma}$ and $\bar{M}_1$ surface states located in large energy gaps. This variety of states allows to test the importance of different contributions to Γ_{ee}. For Be(0 0 0 1) the different contributions to the surface-state-hole decay rate at $\bar{\Gamma}$ and $\bar{M}$ and its energy (momentum) dependence are summarized in Table 5 and in Fig. 60 [143]. The computed Γ_{ee} at $\bar{\Gamma}$ (265 meV) is in good agreement with the experimental value if the electron–phonon contribution is subtracted (see below) and with the calculated, using the model potential, decay rate of 280 meV [53]. For the $\bar{M}_1$ state a value of $\Gamma_{ee} = 72$ meV is found. This value is significantly smaller than the first reported value of 380 meV [145] measured at room temperature which contains large contributions from phonons, defects and uncertainties due to experimental energy and momentum resolution. Surprisingly, the calculated decay rate of the $\bar{M}_2$ state is only slightly larger than that at $\bar{M}_1$ which is
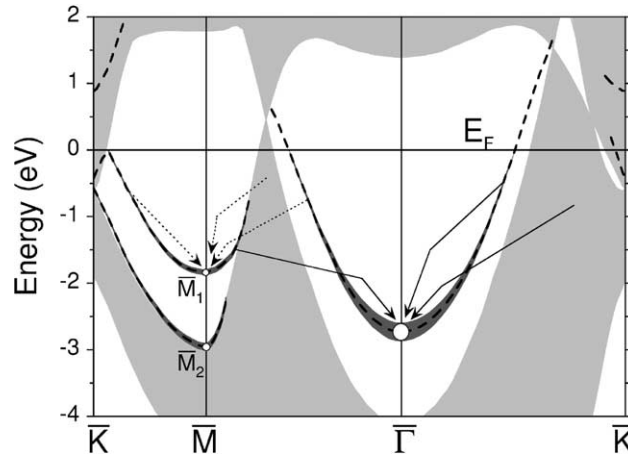
Fig. 59. The computed Be(0 0 0 1) electronic structure along symmetry directions. The projected bulk states are in light gray whereas the dashed lines denote the surface states. All possible electronic transitions to a surface hole (open circle) are indicated by arrows. The calculated decay rates are shown by shaded bands as a function of the momentum. From Ref. [143].

1 eV closer to E_F and nearly three times smaller than the Γ_{ee} of the $\bar{\Gamma}$ surface state with a similar binding energy. This unusual behavior can be understood by examining the contributions of surface and bulk states to the hole-decay mechanism.

In Fig. 60, we show in detail the different contributions to Γ_{ee}. We divide the transitions into intraband and interband transitions (see arrows in Fig. 59). Intraband transitions turn out to be the main channel responsible for the hole decay accounting for 85% (65%) of the total width at $\bar{\Gamma}$ ($\bar{M}_1$). Their relevance increases as the state approaches E_F (see Fig. 59 for the evolution of $\Gamma_{ee}(\bar{\Gamma})$ and $\Gamma_{ee}(\bar{M}_1)$ along the symmetry directions). Special mention should be given to the evolution of the $\bar{M}_1$ state along $\overline{M\Gamma}$. Fig. 59 shows how this state becomes rapidly a resonance in the projected bulk band structure as it disperses towards E_F. This transition is also manifested in a change of the dominant channel for hole decay in Γ_{ee} as we move away from the bottom of the surface band towards E_F, namely, from intraband to interband (3D-bulk) with a non-negligible contribution from the $\bar{\Gamma}$ surface state. So 2D inter- and intraband transitions account for ∼80% of the full decay at $\bar{M}_1$.

Table 5
Surface-state decay rate Γ (meV) for Be calculated at the $\bar{\Gamma}$ and $\bar{M}$ symmetry points (Ref. [143]) together with the results from the 3D- and 2D-EGM and experiments

	Surface-state energy (eV)		Contributions from				Total Γ	3D EGM	2D EGM	Experimental $T = 0$
			$\bar{\Gamma}$	$\bar{M}_1$	$\bar{M}_2$	Bulk				
$\bar{\Gamma}$	−2.73	−2.78	225	5	∼ 0	35	265	90	610	281
$\bar{M}_1$	−1.83	−1.8	10	46	∼ 0	16	72	40	420	
$\bar{M}_2$	−2.95	−3.0	9	36	9	42	96	105	620	
$\bar{\Gamma}$	−2.80		240			40	280			

Γ is decomposed in contributions from different states. The computed surface-state energies (2nd column) are in good agreement with experiments (3rd column) [143,145]. The bottom line shows the 1D calculation results of Ref. [53].
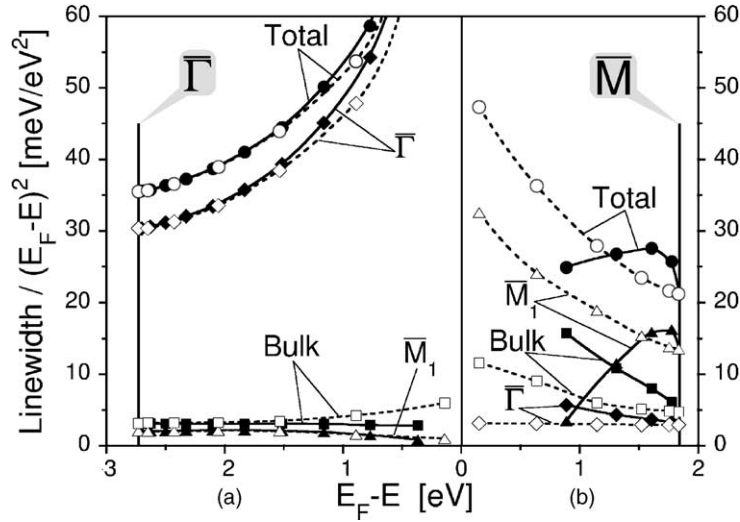
Fig. 60. Hole-decay rate divided by $(E_F - E)^2$ as a function of energy for: (a) the $\bar{\Gamma}$ surface state along $\bar{\Gamma}\bar{M}$ (solid lines) and $\overline{\Gamma K}$ (dashed lines); (b) the $\bar{M}_1$ surface state along $\overline{M\Gamma}$ (solid lines) and $\overline{MK}$ (dashed lines). Filled circles correspond to the total decay rate, diamonds give the contribution from the $\bar{\Gamma}$ state, squares from bulk states and triangles from the $\bar{M}_1$ state. Adapted from Ref. [143].

This result clearly illustrates the competition between the 2D character of the surface states and the 3D screening and delocalization of the underlying bulk states in controlling the hole-decay dynamics at metal surfaces. Furthermore, for the $\bar{\Gamma}$ state, the interband contribution (bulk and from $\bar{M}_1$ state) to the energy-scaled decay rate $(\Gamma_{ee}/(E_F - E)^2)$ is energy independent (Fig. 60). The sum of these two contributions is below 20% of the total Γ_{ee}. The case of the $\bar{M}_2$ state is more complicated since it is not a well-defined surface state as the other two states are. It is located mainly at the third and fourth atomic layers [60] and has one additional decay channel, i.e. electron transitions from the $\bar{M}_1$ state. For this state the intraband contribution is only 10% of the full decay rate, but interband transitions from the $\bar{M}_1$ state accounts for 38% comparable to the 44% contribution from bulk states. These results indicate that even for this very weak surface-state inter- and intraband surface transitions provide more than 50% of the full decay rate. The reduction of the intraband contribution is responsible for the smaller decay rate at $\bar{M}_2$ as compared to the $\bar{\Gamma}$ state and thus the evaluated decay rate is closer to what one obtains using a 3D EGM (see Table 5). Thus deviations from a quadratic law stem from the peculiar character of the dynamically screened surface-state transitions contributing to Γ_{ee}. This explains the different momentum and energy dependence in Be as compared to other metal surfaces (Cu, Ag and Mo) [138,202].

As stated before, it is necessary to address the issue of how the low-dimensionality of the surface influences the energy dependence of the hole decay and to compare with the results from a 2D(3D) EGM. In the 3D EGM the decay rate scales as $(E_F - E)^2$ [71,76], while in 2D the dependence is modified to $(E_F - E)^2 \ln |E_F - E|$ [296,297]. For Be the 3D EGM gives $\Gamma_{ee} = 90$ meV at $\bar{\Gamma}$ that is significantly smaller than the intraband contribution of 225 meV, but larger than the interband one (40 meV). This difference is a direct consequence of the absence of a surface energy gap in the 3D EGM. On the other hand, the 2D EGM gives $\Gamma_{ee} = 610$ meV which is substantially larger than the first-principle value. This difference is a direct consequence of the different type of screening in the two

models. The absence of the underlying bulk states in the 2D EGM strongly limits the screening of the electron–electron interactions. Therefore, larger linewidths are expected in this low-dimensional screening scenario for the hole decay. In fact, the computed energy-scaled decay rates in Fig. 60 exhibit a clear deviation from the expected constant value of a 3D system and the deviation increases as we approach the Fermi energy. It is quite difficult to determine the precise energy dependence of the decay rate (logarithmic or power law), but the computed data show a strong deviation from the quadratic law with an approximate energy dependence $\Gamma \propto (E_{\mathrm{F}} - E)^{\alpha}$ with $0 < \alpha < 2$ ($\alpha \approx 1.6$ at $\bar{\Gamma}$). The highly non-local electron self-energy (peaked at the surface) enhances the contributions from intraband transitions within the surface-state band (2D character). This effect is common to all metal surfaces, however, the precise energy and momentum dependence of the decay rate is determined by the specific surface band structure and screening (provided mainly by the underlying bulk states).

6.1.4. Electron–phonon contribution to the decay rate

The main signature of the electron–phonon contribution to the linewidth broadening is the temperature dependence. For binding energies exceeding $k_{\mathrm{B}}T$ we can neglect the temperature dependence of the electron–electron scattering. The temperature dependence of Γ_{ep} was calculated for the hole state at the $\bar{\Gamma}$ point for Cu(1 1 1), Ag(1 1 1) and Au(1 1 1) [95,96,101]. For a comparison with the experimental temperature dependence we show in Fig. 61 the sum of the constant contribution from
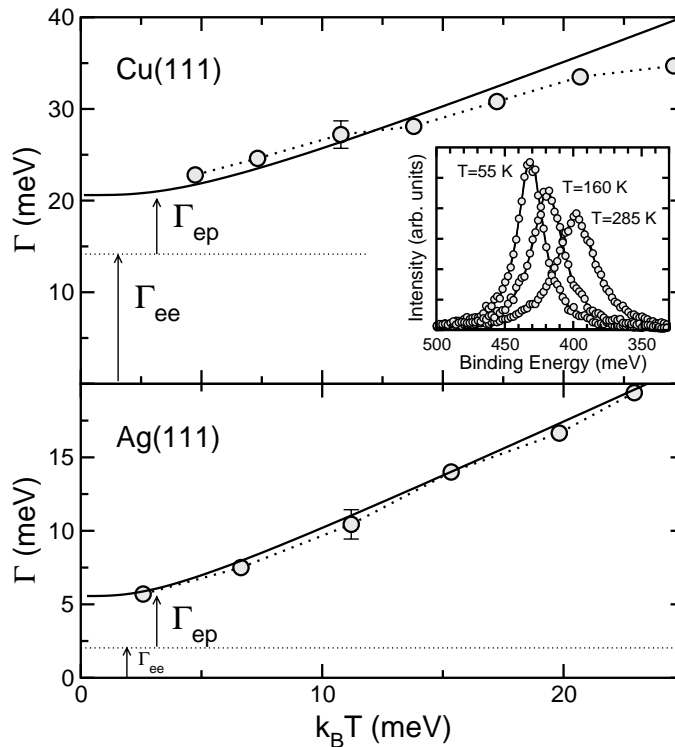

Fig. 61. Calculated linewidth broadening of the Cu(1 1 1) and Ag(1 1 1) surface hole state at the band minimum as a function of temperature (solid lines), Γ_{ee} (dotted lines) photoemission data (open circles). The inset shows the energy distribution curves on Cu(1 1 1) for selected temperatures. Adapted from Ref. [95].

Table 6
Calculated and measured low-temperature linewidths Γ at the band minimum, in meV, and mass enhancement factors λ for the surface states of Cu(1 1 1) and Ag(1 1 1)

	Γ_{2D}	Γ_{3D}	Γ_{ep}	Γ_{ee}	$\Gamma_{ee} + \Gamma_{ep}$	Γ_{STM}	Γ_{PES}	λ
Cu(1 1 1)	7.6	8.1	7.3	14.0	21	24	23 ± 1.0	0.16
Ag(1 1 1)	4.7	5.2	3.7	2.0	5.7	6	6 ± 0.5	0.12

Γ_{2D} and Γ_{3D} are electron–phonon contributions to the width Γ calculated within 2D and 3D Debye models (from [52]). Γ_{ee} is the calculated linewidth due to electron–electron scattering [52] (this value for Γ_{ee} is a lower limit, because the used model does not take into account the confinement of d-electrons [79]), Γ_{ep} from electron–phonon scattering [96], Γ_{STM} from STM measurements at $T = 4.6$ K [52], Γ_{PES} from PES measurements [100].

Γ_{ee} and the T-dependent Γ_{ep} [95]. In Table 6 we summarize the calculated and measured low-temperature results for the linewidth broadening for the surface states of Cu(1 1 1) and Ag(1 1 1) at the bottom of the band. The sums of the calculated contribution from the electron–electron interaction Γ_{ee} [52] and the electron–phonon interaction Γ_{ep} are in good agreement with STM [52] and PES [100] data.

The most interesting hole-binding energy region is of course the one very close to the Fermi level, in particular when the binding energy is less than the maximum phonon frequency ω_m. In this region, the linewidth broadening is mainly determined by the electron–phonon coupling. The contribution from electron–electron interaction is very small. For Cu(1 1 1), Ag(1 1 1) and Au(1 1 1), $\Gamma_{ee} < 0.2$ meV. In Fig. 62 we show the calculated results Γ_{ep}, at $T = 30$ K, for Cu(1 1 1) and Ag(1 1 1) together with the experimental results [95]. From a simple 3D Debye model we would expect a cubic binding energy dependence in the region below ω_m (see Table 3), which obviously is not the case in the experimental data. The saturation of Γ_{ep} for binding energies exceeding ω_m is clearly seen in experimental data. Adding the contribution from the electron–electron interaction, values close to the experiment are obtained (see Table 6). We note from Fig. 62, that the contribution from the Rayleigh mode gives about 38% of Γ_{ep} beyond the maximum phonon frequencies, indicating that bulk phonons give most of the contributions in this range. But for binding energies below the maximum of the Rayleigh-mode energy, this mode alone represents on an average of about 85% of the electron–phonon scattering rate Γ_{ep}.

On Al(1 0 0) the $\bar{\Gamma}$ surface state is located at the bottom of a narrow energy gap [62] in contrast to the (1 1 1) surfaces of the noble metals. Here the Rayleigh mode plays a minor role at any energy including very close to E_F [96]. It accounts only for 10% of the total electron–phonon contribution for energies around E_F. This contribution decreases strongly moving away from the Fermi level to larger binding energies. The explanation is based on the fact that the surface-state charge distribution lies mainly in the bulk: only 7% of the charge is localized at the surface atomic layer leading to a small overlap with the Rayleigh modes and therefore to a small contribution of this mode to the decay rate.

6.2. Image-potential states

The first self-energy calculations of the decay rate of image-potential states were performed for noble-metal surfaces. The drastic approximations used for surface and bulk wave functions as well as for the surface screening allowed only to obtain qualitatively correct results [298–300]. A detailed quantitative comparison with experimental data has been obtained recently with the methods presented in this review.
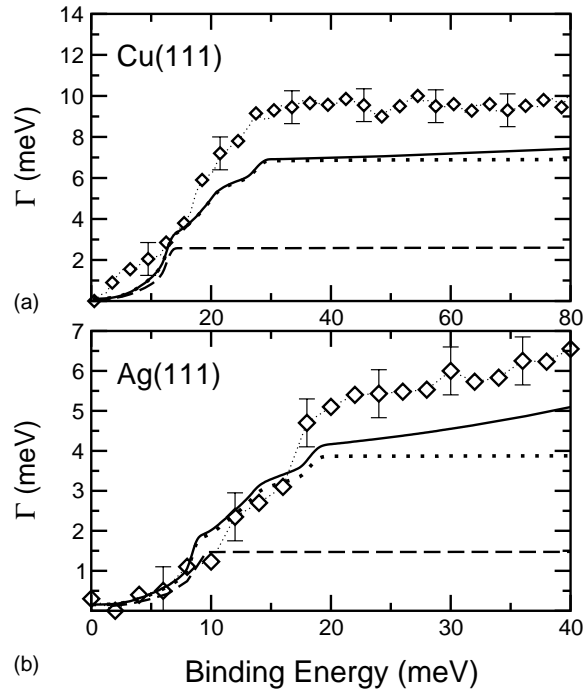
Fig. 62.   (a) Linewidth broadening of the Cu(1 1 1) surface hole state as a function of binding energy, $\Gamma_{ee} + \Gamma_{ep}$ (solid line), Γ_{ep} (dotted line), the Rayleigh mode contribution to Γ_{ep} (dashed line), and photoemission data (diamonds). (b) The same as in (a) for Ag(1 1 1). Adapted from Ref. [95].

6.2.1. Electron–electron contribution at $k_\parallel = 0$

To analyze the physics of the electron dynamics in image-potential states we begin with the (1 0 0) and (1 1 1) surfaces of Cu as examples [301]. In Fig. 1, the electronic structure of these surfaces was schematically shown illustrating possible channels of electron decay from the $n = 1$ image-potential state, namely, interband transitions into bulk and surface states. The electron decay from the higher image-potential states also includes transitions into lower lying image-potential states. In Table 7, we

Table 7
Decay rates in meV of the $n = 1$ image-potential state on Cu(1 1 1) [69] together with the experimentally determined decay rate at $T = 25$ K [221]

m^*	W	Γ_{bulk}	Γ_{vac}	Γ_{mix}	Γ_{ee}	Experimental
$=1$	GW–RPA	44(28)	47(5)	$-54(-12)$	37 (21)	
$=1$	GW–TDLDA	43	42	-45	40	
$=1$	GWΓ–TDLDA	43.5	47	-54	36.5	
$\neq 1$	GW–RPA	32(24)	34(5)	$-37(-12)$	29(17)	
$\neq 1$	GWΓ–TDLDA	30.5	35	-38	28.5	30

Contributions from decay into bulk states lying below the bottom of the projected band gap, thereby excluding the contribution from decay into the $n = 0$ intrinsic surface state, are displayed in parentheses. Effective masses have been set equal to either the free-electron mass ($m^* = 1$) or to realistic values for all available final states ($m^* \neq 1$). Three different models for the description of the interaction and screening have been used: GW–RPA, GW–TDLDA and GWΓ–TDLDA.

present the results of the calculation by Sarría et al. [69] for the inverse lifetime of an electron in the $n = 1$ state at the $\bar{\Gamma}$ point on Cu(1 1 1) obtained using different approximations for the effective masses of final states and for the description of the interaction and screening (see Section 2.3). As follows from the table when realistic effective masses of final states are used, both the GW–RPA and GWΓ–TDLDA calculations give values for the linewidth broadening that are in excellent agreement with low-temperature TR-2PPE measurements [221]. When free-electron effective masses $m^* = 1$ are used, all the obtained inverse lifetimes are 20–30% larger than the measured ones.

It is useful to separate the different contributions to the integral equation (17) given for the decay rate. This integral can be calculated for either bulk ($z < 0$) or vacuum ($z > 0$) coordinates. Thus Γ_{ee} is separated into three contributions:

$$\Gamma_{\text{ee}} = \Gamma_{\text{bulk}} + \Gamma_{\text{vac}} + \Gamma_{\text{mix}}, \tag{56}$$

where Γ_{bulk}, Γ_{vac} and Γ_{mix} correspond to take $(z, z' < 0)$; $(z, z' > 0)$ and $(z, z'$ of different signs) integrals of Eq. (17) or equivalently Eq. (19). Comparing the different results displayed in Table 7 one can conclude that: (i) GW–RPA and GWΓ–TDLDA give nearly identical results; (ii) the surface state is an important channel for the decay of image-potential-state electrons giving 30–40% of the total decay value [69,302]. In the calculations of Osma et al. [302] the wave functions $\phi_s(z)$ calculated at the $\bar{\Gamma}$ point were used for all parallel momenta of the surface state. This probably leads to some overestimation of the surface-state-channel decay.

In Table 8, we show the evaluated decay rate for electrons in the $n = 1, 2$ and 3 image-potential states at the $\bar{\Gamma}$ point on Cu(1 0 0). The computations have been done for both $m^* = 1$ and $m^* \neq 1$ effective masses of final bulk and surface states. Effective masses for $n = 1$ and 2 have been taken as $m^* = 1$ following the measured dispersion of these states [4]. The use of realistic effective masses leads to excellent agreement with the measured lifetime for $n = 1$ while for $n = 2, 3$ the theory gives lifetimes which are longer than published experimental values [218,231]. However, recent measurements on a better sample (see Fig. 41) come close to the latest calculations [69]. The remaining discrepancy can be attributed to the residual step density on the sample which leads to an efficient resonant interband scattering to the $n = 1$ band [232,234,235] and an apparent reduction of the measured lifetimes for the higher image-potential states.

The GW calculation of the decay rate takes into account not only the overlap of the wave function with the metallic bulk and surface states, but also the availability of states below the image-potential

Table 8
Calculated decay rates and lifetimes of the $n \leq 3$ image-potential states on Cu(1 0 0) together with experimentally determined values

	Decay rate (meV)			Lifetime (fs)			
$n = 1$	22	17.5		30	38	40 ± 6	41.3
$n = 2$	5	3.9		132	168	120 ± 15	150
$n = 2 \rightarrow n = 1$	0.5	0.4	0.4				
$n = 3$	1.8	1.4		367	480	300 ± 20	406
$n = 3 \rightarrow n = 2$	0.05	0.05					
$n = 3 \rightarrow n = 1$	0.17	0.16					
Specification	$m^* = 1$	$m^* \neq 1$	Experimental	$m^* = 1$	$m^* \neq 1$	Experimental	Experimental
Ref.	[301]	[69]	[222]	[301]	[69]	[218]	[222]

In the case of $n = 2$ and $n = 3$, contributions from decay into the lower image-potential states are also displayed.

Table 9
Lifetimes τ_n in fs for the nth image-potential state on clean metal surfaces measured by time-resolved two-photon photoemission and calculated using the GW approximation

		τ_1	τ_2	τ_3	τ_4	τ_5	Refs.
C(0 0 0 1)	Experimental	40 ± 6					[303]
Ni(1 1 1)	Experimental	7 ± 3					[304]
Cu(0 0 1)	Experimental	40 ± 6	120 ± 15	300 ± 20	630	1200	[36,218]
	Experimental	41.3	150	406			[222]
	Theoretical	38	168	480			[69]
Cu(1 1 9)	Experimental	15 ± 5	39 ± 5	105 ± 15	200 ± 20	350 ± 40	[248]
Cu(1 1 7)	Experimental	15 ± 5	39 ± 5	95 ± 15	190 ± 20	350 ± 40	[248]
Cu(1 1 1)	Experimental	18 ± 5	14 ± 3	40 ± 6			[221,244]
	Theoretical	29					[69]
Cu(7 7 5)	Experimental	18 ± 2					[305]
Ag(0 0 1)	Experimental	55 ± 5	160 ± 10	360 ± 15			[218]
	Theoretical	55	219	658			[75]
Ag(1 1 1)	Experimental	32 ± 10	≤ 20				[260]
	Theoretical	18					[75]
Pd(1 1 1)	Experimental	25 ± 4					[225]
	Theoretical	22	89				[225]
Pt(1 1 1)	Experimental	26 ± 7	62 ± 7				[68]
	Theoretical	29	73				[68]
Ru(0 0 0 1)	Experimental	11					[267,306]
	Theoretical	14					[56]
Li(1 1 0)	Theoretical	18	44				[307]

state and the screened interaction in the metal. As evident from Table 8 the decay to the $n = 1$ state amounts to ~10% of the total decay rate in good agreement with recent experimental values [222]. For the $n = 3$ state the decay rate into the $n = 2$ state is about one third of that into the $n = 1$ state. For the creation of the electron–hole pair the overlap with bulk states is more important than the one between the image-potential states which would favor the decay $n = 3 \to n = 2$ over $n = 3 \to n = 1$. The predicted trend is in qualitative agreement with experimental results for stepped copper surfaces [235].

Table 9 shows the available measured and calculated lifetimes for single-crystal surfaces for $k_{\parallel} = 0$. Only the most recent results have been included, for the discussion of previous work we refer the reader to the references. There is generally quite good agreement between first-principles theory and experiment. The main ingredient is the penetration of the wave function into the metal. The shorter lifetimes for the d-band metals can be explained by the large density of states around the Fermi level [308].

It must be stressed, however, that penetration arguments alone are generally not sufficient to understand the decay of image-potential states at different surfaces, sometimes not even qualitatively. One striking example of the limitations of the penetration approximation appears when comparing Cu(1 0 0) and Ag(1 0 0) surfaces which have a very similar electronic structure. Due to a slightly smaller s–p-gap, the penetration of the wave functions in Ag(1 0 0) is slightly larger than in Cu(1 0 0), whereas the experimental decay rates of the image-potential states are nearly 40% smaller [218]. Only after properly accounting for the decay into the surface plasmon, as described below, many-body calculations can explain the experimental trend. Another example is provided by the first

image-potential state of Cu(1 1 1) and Cu(1 0 0). While experimental decay rates are 30 meV [221] and 16.5 meV [218], respectively, model-potential calculations give penetration values of 0.22 and 0.05 [45]. Thus, the rates differ by a factor of 2, while the penetrations differ by a factor of 4. In this case, it is the reduced phase space of available final states in Cu(1 1 1) and the presence of the occupied surface states in Cu(1 1 1), when accounted for in a many-body description, that give the correct ratios of lifetimes.

6.2.2. Role of collective excitations for Ag

In many metals plasmon excitations have energies of 10–15 eV. Therefore, these excitations are beyond the relevant energy interval 0–4 eV for the decay of the image-potential-state electrons. In Ag, however, both the surface and bulk plasmons have energies around 3.8 eV. These collective excitations can influence the decay of image-potential states via the participation of d-electrons in the screening of electron–electron interaction [75,79]. The effect of d-electrons in the screening can be taken into account by using the s–d-polarization model of Liebsch [77,309] (see Eq. (20)) that replaces the d-states by a polarizable medium characterized by the local dielectric function $\epsilon_d(\omega)$. It had been expected that the inclusion of the d-band effect and therefore of the surface-plasmon excitation as a new channel for the decay of image-potential states would reduce their lifetimes. García-Lekue et al. [79], however, showed that the subtle combination of the spatial variation of s–d-polarization and the characteristic non-locality of electron–electron interaction near the surface yield actually longer lifetimes for the $n = 1$ state on Ag(1 0 0) which are in excellent agreement with time-resolved 2PPE measurements [218]. The presence of collective excitations thus explains why the lifetimes of the image-potential states on Ag(1 0 0) are longer than on Cu(1 0 0) (see Table 9).

6.2.3. Momentum and energy dependence of the decay

The electron decay in image-potential states at the $\bar{\Gamma}$ point is determined by interband transitions weighted by the imaginary part of the screened electron–electron interaction. The decay of electrons with finite momentum also includes intraband transitions within the image-potential-state band itself. The role of these transitions has been studied recently by Berthold et al. [231] for the $n = 1$ and 2 image-potential states on Cu(1 0 0). As already shown in Fig. 44 intraband transitions contribute approximately 50% to the total extra increase of the inverse lifetimes with respect to the $k_\parallel = 0$ value. The physical origin of the remarkable importance of intraband scattering is the good spatial overlap of the initial- and final-state wave functions (Fig. 63). It makes this process competitive with interband decay to the bulk metal despite a much smaller phase space and energy exchange [231].

On Ag(1 0 0) a significantly stronger linewidth broadening as function of parallel momentum compared to Cu(1 0 0) has been found [310]. No time-resolved measurements have been reported, so an influence of dephasing by defects or steps cannot be excluded. However, the possible influence of the collective excitations in Ag discussed in Section 6.2.2 deserves further investigation.

6.2.4. Phonon contribution

Compared to surface states the coupling of image-potential states to bulk bands is significantly smaller and one can expect a minor role of electron–phonon interaction in the linewidth broadening of image-potential states. Recently, Eiguren et al. [101] evaluated the phonon contribution to τ^{-1} for the first image-potential state on Cu(1 0 0) and Ag(1 0 0). The calculations for the electron–phonon
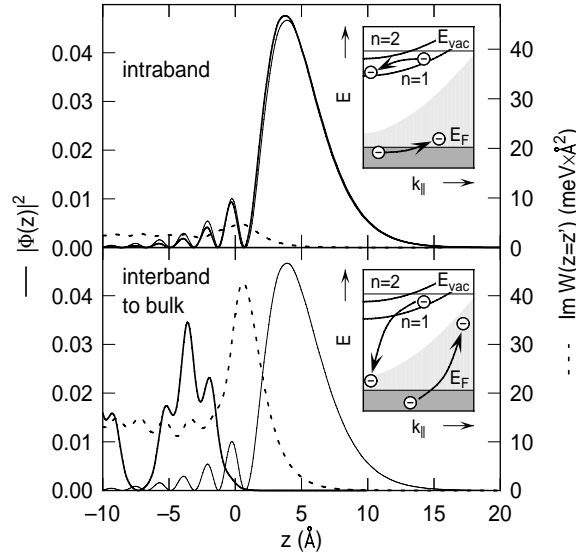
Fig. 63. Imaginary part of the screened Coulomb interaction $\text{Im}W(z = z')$ (dashed line) and final-state probability density $|\phi_f|^2$ (thick solid line) computed for typical cases of the decay of an $n = 1$ image-potential state electron with probability density $|\phi|^2$ (thin solid line). Top: intraband scattering. The energy exchange is $E_0 - E_f = 0.55$ eV. Bottom: interband decay with energy exchange $E_0 - E_f = 3.5$ eV. Momentum exchange is $q_\parallel = 0.38$ Å^{-1} in both cases. The insets illustrate the different decay processes. From Ref. [231].

coupling parameter λ and Γ_{ep} resulted in $\lambda \lesssim 0.01$ and $\Gamma_{\text{ep}} < 1$ meV thus demonstrating the negligibly small role of phonons in the electron dynamics of image-potential states in agreement with the experimental findings [244]. The situation is different for the Cu(1 1 1) surface, where the image-potential state is close to the band edge. The larger overlap with the bulk bands leads to an electron–phonon coupling parameter of $\lambda = 0.06 \pm 0.01$ [221]. However, the shift of the band edge with temperature limits the accessible temperature range.

6.3. Magnetic surface states

The decay of electronic excitations at magnetic surfaces differs from non-magnetic systems in several aspects: (i) the majority- and minority-spin electrons constitute two subsystems and the total spin is not changed by scattering or decay processes; (ii) there are additional low-energy excitations of the spin systems such as spin waves or magnons. The fact that there are more unoccupied minority-spin states available as final states in scattering processes leads to a larger decay rate for minority-spin electrons than for majority-spin electrons.

For image-potential states the exchange splitting between majority- and minority-spin states is comparable to the total linewidth [4,30], so an analysis of the intrinsic linewidth of the individual states is difficult. This limits also the use of time-resolved 2PPE. For Fe(1 1 0) the linewidth of the minority-spin state was found with spin-dependent inverse photoemission to be twice the value for the majority-spin state [311]. A later study with 2PPE with better resolution observed a somewhat smaller difference [312] in agreement with fcc Fe films on Cu(1 0 0) [313]. The 2PPE experiments employed polarization selection rules to obtain spin sensitivity [314]. Time-resolved two-photon photoelectron spectroscopy
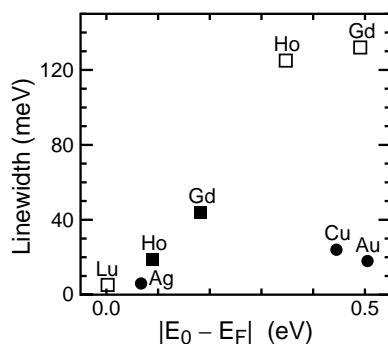
Fig. 64. Linewidth of occupied (filled symbols) and unoccupied (open symbols) surface states as a function of energy distance to E_F measured by STS [52,195]. The linewidths of the lanthanides (squares) are significantly larger than those of the noble metals (dots).

with spin analysis is needed for a reliable determination of the intrinsic linewidth and of the exchange splitting of image-potential states at ferromagnetic surfaces.

Spin-resolved photoemission [315] and inverse photoemission [316] has been used to study the spin-split surface states at the Gd(0 0 0 1) surface. The photoemission results show a somewhat larger linewidth for the minority-spin hole compared to the majority-spin hole [315]. The difference is attributed to electron–magnon scattering in the minority-spin channel as opposed to electron–phonon scattering in the majority-spin channel [317].

Scanning tunneling spectroscopy has been used to study the linewidth of the occupied and unoccupied spin-split surface states on several lanthanide metals [195,196]. The linewidth increases linearly with the distance from the Fermi energy (see Fig. 64). There is no significant difference in the slope of the linewidth between occupied (majority-spin) and unoccupied (minority-spin) states. However, the linewidths for the lanthanides are considerably larger than the ones found for the noble-metal surfaces [52]. This is attributed to the larger density of states around E_F [195].

6.4. Overlayer and adsorbate states

6.4.1. Rare gases on metal surfaces

The influence of rare-gas layers on the properties of image-potential states have been investigated for Xe/Ag(1 1 1) [259,272], Xe/Cu(1 1 1) [262,263,318], Ar, Kr and Xe on Cu(1 0 0) [268,269,273] and Xe/Ru(0 0 0 1) [266,267]. Experimental results for the lifetime of the states are collected in Table 10 for various systems together with predictions from different models. Frequently, the lifetimes can be estimated by scaling the measured values of the clean surface with the inverse penetration of the wave function. In some cases, even simple models that treat the rare-gas layer as tunneling barrier and use this penetration approximation give reasonably good agreement between experiment and theory (compare Table 10). In other cases, however, significant deviations, whose origins are not fully understood, remain.

Crucial for the calculation of lifetimes in the presence of overlayers are certainly accurate wave functions for the image-potential states which, in principle, should be based on a full 3D potential. Presently such a potential is only available for Ar/Cu(1 0 0) from the work of Marinica et al. [269]. For the other systems, the corrugated 1D model potential described below generally gives better results than

Table 10

Lifetimes (in fs) of the first two image-potential states of different surfaces covered with rare-gas layers

		0 ML		1 ML		2 ML		3 ML		4 ML		Ref.
		$n=1$	$n=2$	$n=1$	$n=2$	$n=1$	$n=2$	$n=1$	$n=2$	$n=1$	$n=2$	
Xe on Ag(1 1 1)	exp	32	≤ 20	192	131	507	173	507	86	800	58	[272]
	tunn	–	–	38	102	240	320	744	148	–	14	[272]
	1D	32	–	192	131	396	204	523	77	552	52	[273]
Xe on Cu(1 1 1)	exp	22	17	70	40	250	95	300	70	–	–	[263]
	cont	9	12	130	120	310	25	380	38	–	–	[263]
	1D	–	–	168	–	337	–	426	–	440	–	[273]
Xe on Cu(1 0 0)	exp	40	130	74	200	164	265	252	134	325	76	[273]
	1D	–	–	62	298	158	620	260	395	323	95	[273]
Kr on Cu(1 0 0)	exp	40	130	86	230	185	330	226	230	268	79	[273]
	1D	–	–	76	342	206	720	348	539	435	153	[273]
	exp	40	130	120	320	480	710	1520	1840	5400	3900	[268]
Ar on Cu(1 0 0)	1D	–	–	99	372	406	1187	1252	2563	3468	5054	[273]
	3D	–	–	142	309	447	611	1190	1150	3070	1640	[269]
	1D GW	38	132	90	425	465	2300	2290	–	–	–	[276]
Xe on Ru(0 0 0 1)	exp	11	–	(52)	(130)	125	155	–	–	–	–	[267]
	tunn	–	–	50	266	99	38	–	–	–	–	[267]
	1D	–	–	20	154	51	321	–	–	–	–	[273]

exp: experiment results of 2PPE; tunn: tunneling model using a square barrier, cont: continuum model with k-dependent effective mass (model 2 of Ref. [263]); 1D: corrugated 1D model potential and penetration approximation; 3D: ab-initio three-dimensional Ar potential and penetration approximation; 1D GW: one-dimensional model potential and GW-calculation. Values in parentheses are for a complete incommensurate monolayer.

continuum descriptions. Another possible source for the deviations is of course the inadequate inclusion of the many-body physics of the decay at the metal/dielectric interface in the penetration approximation.

Machado and co-workers have performed many-body calculations of the decay rate of image-potential states for 1–4 monolayers of Ar on Cu(1 0 0) [276]. As it is computationally very demanding to combine the 3D Ar-potential of Marinica et al. [269] with a full many-body treatment of the decay, they used a parameterized potential that takes effectively into account the atomic corrugation of the Ar layers but retains the 1D character of the image-potential states. This model potential, proposed by Berthold et al. [273], is constructed in such a way that, for infinitely thick rare-gas layers, it would reproduce the known effective mass of the electrons in the minimum of their conduction band.

The potential is plotted in Fig. 65 for the case of 2 ML of Ar on Cu(1 0 0) (solid line) together with the probability density of the first image-potential state (dotted line). For comparison we have included the potential and the probability density of clean Cu(1 0 0) (thin solid and thin dotted lines, respectively). The metal jellium edge $z = 0$ is placed at half an interlayer distance beyond the last atomic plane. The shaded region indicates the position of the adlayer.

In Fig. 66, we show the theoretical and experimental results for the lifetimes of the first and second image-potential states of Ar/Cu(1 0 0), from 0 to 4 monolayers of Ar [276]. Lifetimes are plotted on a logarithmic scale that clearly shows the exponential rise of τ with increasing coverage. For the $n = 1$
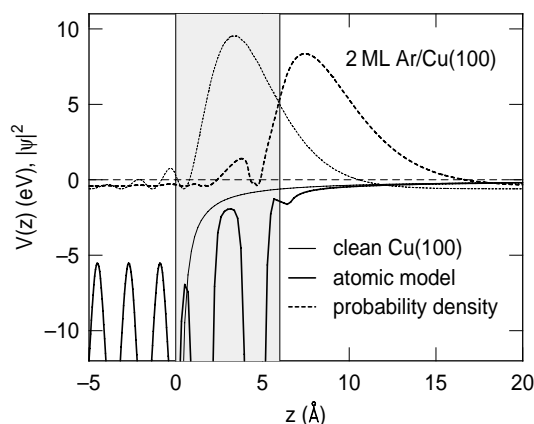
Fig. 65.   Example of the model potential (thick solid line) and the calculated $n = 1$ probability density (thick dotted line) for 2 ML of Ar/Cu(1 0 0). For comparison the potential and probability density of clean Cu(1 0 0) are also shown (thin lines). The shaded region indicates the adlayer, the metal jellium edge is at $z = 0$.

state a very good agreement between theory and experiment is found. However, for the second image-potential state, theoretical lifetimes are longer than the experimental ones.

In addition to the increase of lifetimes, another effect of the adsorbed layers is the decrease in binding energies of image-potential states (see Ref. [268]). This is due to the decoupling of the wave function from the metal induced by the Ar layers, whose negative electron affinity acts on image-potential states as a repulsive potential barrier. The probability density of the image-potential states is shifted towards the vacuum region, where the image potential is weaker, so that these states become less bound. This shift is illustrated in Fig. 67, where we have plotted the calculated $n = 1$ probability densities for Cu(1 0 0) and for 2 ML Ar/Cu(1 0 0). The image-potential-state wave function decouples from the metal substrate as coverage increases. The penetration of the $n = 1$ wave function into the metal ranges from 5.2% at Cu(1 0 0), to 1.24% for 1 ML and 0.036% for 4 ML.

It is interesting to analyze the contributions of bulk, vacuum and mixed terms to the decay rate of image-potential states (see Eq. (56)) and their variations with coverage. The contributions to the total
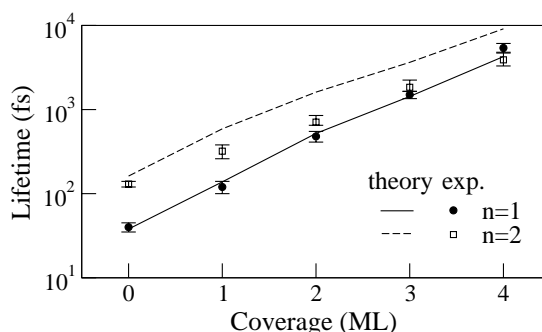

Fig. 66.   Calculated and experimental lifetimes of $n = 1$ and $n = 2$ image-potential states for 0–4 ML Ar coverage. Solid line and circles stand for theoretical and experimental results for $n = 1$, respectively. Dashed line and open squares show theoretical and experimental results for $n = 2$.
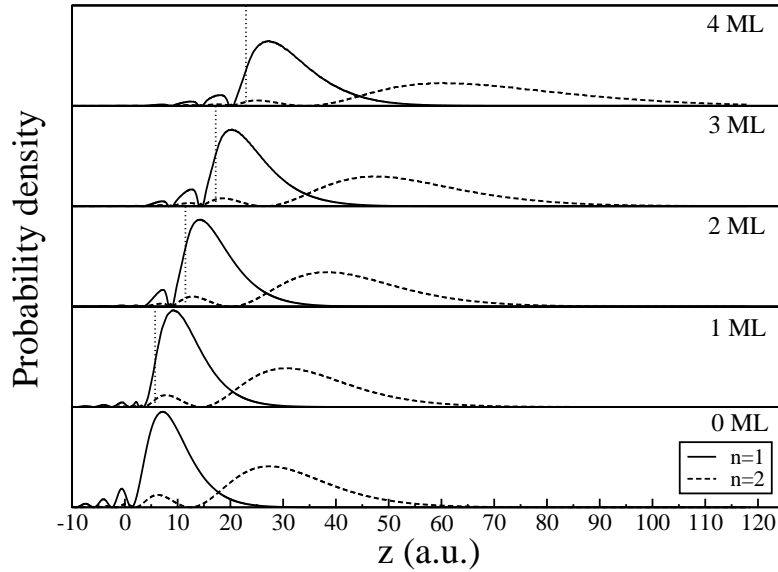
Fig. 67. Calculated probability density for $n = 1$ (solid line) and $n = 2$ (dashed line), for 0–4 ML Ar/Cu(1 0 0). Position of last Ar plane is shown with dotted line. $z = 0$ corresponds to metal jellium edge.

rate Γ_{ee}, and to Γ_{bulk}, Γ_{vac} and Γ_{mix}, from the clean surface to 2 ML of Ar/Cu(1 0 0), are shown in Table 11. One can see that for the clean surface the contribution from the mixed term is of similar magnitude but of opposite sign compared to the vacuum term. So the total decay rate is approximately the same as the bulk contribution $\Gamma_{ee} \sim \Gamma_{bulk}$. However, for 1 and 2 ML this is not the case, and this approximation would involve an error around 15–25%. This partial compensation explains why penetration arguments have led to the good agreement with experiment obtained for Ar/Cu(1 0 0) in Ref. [269].

6.4.2. Overlayer states Na/Cu

Overlayers of Na on Cu(1 1 1) are one of the most extensively studied system, experimentally and theoretically. Very recently theoretical calculations and STS measurements of the hole-linewidth broadening Γ in a quantum well state for 0.95 and 1.0 monolayers of Na on Cu(1 1 1) have been performed at the $\bar{\Gamma}$ point [57]. The electron–electron contribution, Γ_{ee}, to Γ has been calculated using the model potential proposed in Ref. [57] and the electron–phonon contribution Γ_{ep} has been calculated

Table 11
Calculated bulk, vacuum and mixed terms to the decay rate Γ_{ee} of $n = 1$ and 2 image-potential states, for 0–2 ML of Ar/Cu(1 0 0)

	Γ_{ee}		Γ_{bulk}		Γ_{vac}		Γ_{mix}	
	$n = 1$	$n = 2$	$n = 1$	$n = 2$	$n = 1$	$n = 2$	$n = 1$	$n = 2$
0 ML	17.75	4.02	17.61	3.58	10.34	2.90	−10.2	−2.46
1 ML	4.76	1.13	5.22	0.92	3.03	0.90	−3.49	−0.69
2 ML	1.26	0.41	1.44	0.31	0.80	0.33	−0.98	−0.23

Table 12
Comparison of experimental Γ_{STM} and calculated decay rates Γ for Na on Cu(1 1 1)

ML	E_0	Γ_{STM}	Γ_{ee}	Γ_{ep}	Γ
0.95	−42	14.5 ± 1.5	4	9	13
1.0	−127	21.0 ± 2.0	13	9	22

E_0 is the experimental energy (all energies in meV). Γ_{ee} and Γ_{ep} are the electron–electron and electron–phonon contributions to the decay rate, respectively. From Ref. [57].

by applying the Debye and Einstein model combined with the experimental value $\lambda = 0.24$ determined by Carlsson et al. [151] for 0.95 ML Na/Cu(1 1 1). The value of the Debye energy, $\hbar\omega_D = 18$ meV, has been deduced from helium-atom scattering for 1 ML of Na on Cu(1 0 0) [319] and corresponds to the lower value obtained in a first-principles calculation [320]. Debye models give $\Gamma_{ep} = 9$ meV.

In Table 12, we compare decay rates obtained from the STM measurements with the calculations of Chulkov et al. [57]. In view of the complexity of the processes under consideration, the agreement of the calculated total decay rates Γ which includes electron–electron and electron–phonon contributions with the measured data is reasonable.

Despite the uncertainty in converting Δ to Γ_{STM} (see Eq. (54)) there is a clear variation of the experimental linewidths. The calculations indicate that the change of the decay rate with Na coverage is due to a change of the electron–electron interaction. The increase of the electron–electron contribution, moving from 0.95 to 1 ML, is due to the large increase of the QWS binding energy from 42 to 127 meV. This will open up an increasing number of possible intraband scattering events which increase the linewidth. Furthermore, the electron–electron contribution to the decay rate is as important as the electron–phonon contribution which is in contrast to naive expectations based on the 3D free-electron gas model which leads to $\Gamma_{ee} < 1$ meV for both coverages. This discrepancy was explained in terms of a large contribution to Γ_{ee} from transitions within the surface-state band itself, which are weighted by the enhanced imaginary part of the screened interaction in the surface region (see Fig. 9). Fig. 68, which displays the probability densities of the QWS at 1 ML Na/Cu(1 1 1) and the surface state on
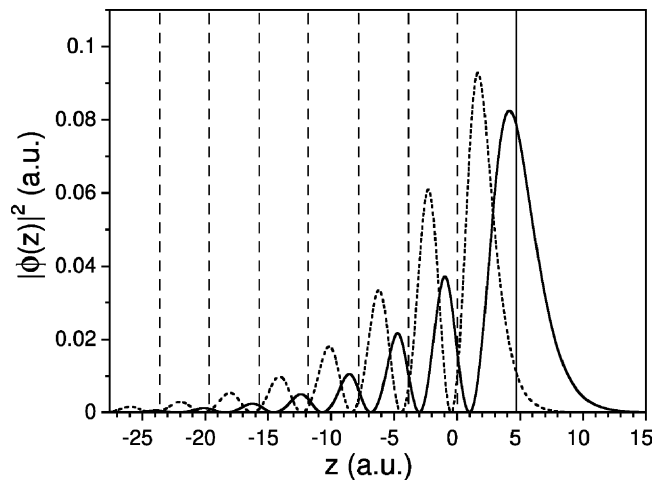

Fig. 68. Calculated probability density for the QWS at 1 ML Na/Cu(1 1 1) (thick solid line) and for the $\bar{\Gamma}$ surface state on clean Cu(1 1 1) (dotted line). Vertical lines indicate the atomic layer positions. From Ref. [57].

clean Cu(1 1 1), highlights that the localization of the QWS to the adlayer separates the 2D state from 3D states even more efficiently than in the case of the clean-noble-metal surface state.

The importance of the contribution of the electron–phonon interaction to the QWS hole decay is illustrated by the numbers in Table 12. Combining estimates based on phonon models with limited first-principles calculations Chulkov et al. [57] find that the surface vibrational mode of Na on Cu(1 1 1) is less localized to the overlayer than previously suggested [320]. According to their analysis, only about 40% of the mode is localized to the Na layer. Furthermore, the phonon-induced decay seems to be insensitive to the variation of the Na coverage in the range 0.95 and 1 ML, the reason being that the surface phonon energies are smaller than the QWS binding energies at these coverages.

6.4.3. Adsorbate states: alkali metals

In most systems electronic excitations located between the Fermi and vacuum levels will decay or delocalize within a few femtoseconds or even less, due to charge transfer to the conduction band of the metal. Lifetimes of alkali-induced states on a free-electron gas have been calculated by several methods [321–324] yielding lifetimes below 1 fs for alkali-surface distances typical of chemisorption. The charge transfer to the continuum is strongly reduced in the case of alkalis adsorbed in the (1 1 1) faces of noble metals, because the large s–p-gap at the $\bar{\Gamma}$ point limits the charge transfer to the conduction band.

In some cases the elastic charge transfer can be comparable to the inelastic decay channel, as it is the case for Cs on Cu(1 0 0), where the Cs level lies in a region of the projected band gap where only small regions of $k_{\parallel}$ are forbidden.

Borisov et al. used the wave-packet-propagation method [20,325–327] to study the one-electron elastic tunneling between several atoms and a Cu(1 1 1) surface. Later Borisov et al. [286] performed calculations for Cs adsorbed on Cu and studied the relative importance of the two decay channels of the adsorbate, namely the one-electron elastic tunneling (the so-called resonant charge transfer) or the multielectron terms (inelastic decay via excitations of the bulk substrate). The resonant charge-transfer contribution Γ_{RCT} was evaluated by the wave-packet-propagation method. The same wave packet was used as the initial state in the calculation of the electron–electron contribution Γ_{ee} to the decay rate using the self-energy of a clean Cu surface. In Table 13, we show the comparison of the results of the calculation with experimental data. For Cs on Cu(1 0 0) the elastic scattering rate is 112 meV, much larger than the 7 meV of the (1 1 1) surface, but still smaller than the 900 meV that would correspond to a free-electron metal. The difference between the (1 0 0) and the (1 1 1) faces is due to the different regions of $k_{\parallel}$ which are forbidden for elastic tunneling from the alkali resonances at $\approx$3 eV above the

Table 13
Lifetimes and decay rates for the Cs/Cu(1 1 1) and Cs/Cu(1 0 0) systems

	Cs/Cu(1 1 1)	Cs/Cu(1 0 0)	Reference
τ (fs) (300 K)	15 ± 6	6 ± 4	Experimental [282,283]
τ (fs) (50 K)	50	Very short	Experimental [281,284,287]
Γ_{RCT} (free-electron)	900	900	Calculated [286]
Γ_{RCT} (meV)	7	112	Calculated [286]
Γ_{ee} (meV)	16.5	20	Calculated [286]
$\Gamma = \Gamma_{RCT} + \Gamma_{ee}$ (meV)	23.5	132	Calculated [286]
$\hbar/\Gamma$ (fs)	28	5	Calculated [286]

Fermi energy (see Fig. 1). The inelastic channel gives similar contributions in both cases leading to values of lifetimes that are in reasonable agreement with the experimental values [281–284,287].

A theoretical study, together with a comparison of the available experimental data, of the lifetime of electronically excited states in the Na, K, Rb, Cs/Cu(1 1 1) systems has been made by Borisov et al. [328]. The theoretical lifetimes of the excited states are found to increase along the sequence Na, K, Rb, Cs in agreement with the experimental results [281–283,288]. This evolution along the alkali series is attributed to the alkali polarizabilities.

6.4.4. Adsorbate states: rare gases

In the last few years a different approach to time-resolved pump-probe experiments using ultrafast lasers that can tackle the time regime below 10 fs has been implemented [279]. This approach is based on high-resolution spectroscopy of the Auger decay of core-excited states. In this method the core-hole-decay time is used as an internal time standard to measure electron-transfer processes. The energy of the emitted Auger electrons will be different depending on whether the resonance electron is still localized or not on the adsorbate when the core-hole decay takes place. This energy shift of the core-hole-decay channels with or without the presence of the resonance electron can be discriminated and the relative contribution of the two processes can be used to determine the charge-transfer time in units of the intrinsic core-hole filling time.

Wurth and Menzel [279] estimate that the approach is sensitive to time scales ranging from approximately 0.1–10 times the intrinsic core-hole decay time. This intrinsic time is about 6 fs for the case of the $2p_{3/2}$ core state in Ar, but can be chosen to be shorter for the case of adsorbates that are more tightly bound to the surface and therefore have shorter charge-transfer times than those of Argon. The charge-transfer time for the case of Ar on Ru(0 0 1) is 1.5 fs. When additional layers are introduced the charge-transfer time increases. For the case of Ar atoms adsorbed on the (1 1 1) faces of Ag, Ni and Cu recent experimental results show that the charge transfer is faster on Ni ($\sim$5 fs) than on Cu and Ag ($\sim$7 fs in both).

An ab-initio study of the resonant charge-transfer problem for the case of a monolayer of Ar adsorbed on Ru(0 0 0 1) has been performed by Sánchez Portal [329]. A width of 600 meV was obtained for the Ar resonance in a supercell calculation using Green function techniques, in good agreement with experiment. The calculations reproduce the counterintuitive energy dependence of the charge-transfer time, namely the increase of the tunneling time with increasing excitation energies and therefore levels closer to the vacuum level. This unexpected result was explained in terms of the interaction of the 4s resonance of Ar with the bulk states and surface resonances of Ru(0 0 0 1).

7. Summary and outlook

The study of electron dynamics at surfaces using photoelectrons has made progress within the last decade. At the example of mainly Shockley states the relative contributions of Γ_{ee}, Γ_{ep} and Γ_{def} could be separated experimentally in several prototypical studies and the theoretical understanding of Γ_{ee} and Γ_{ep} may be considered excellent. Nevertheless, the attempts to "tailor" dynamic surface properties are still in their infancy. The experimental challenge for the near future will be to study excitation and decay processes in more complex material systems like quantum well states confined both normal to a substrate surface and laterally. Some promising attempts have been reported already. As a few examples

we mention the phonon-induced decay of a quantum well hole within a monolayer of Na on Cu(1 1 1) [65,320], the modification of the quasiparticle dynamics in a surface state at Ag(1 1 1) by an adsorbed xenon layer [330], studies of linewidths and electron–phonon coupling in quantum well states within uniform films of Ag on Fe(1 0 0) [131,152,331] and within ultrathin Ag films on Cu(1 1 1) [332] as well as on V(1 0 0) [153,161,333], and the linewidths of adsorbate-induced photoemission peaks [334,335]. A particular challenge may be the study of laterally confined surface states. While they have been identified clearly, e.g. on vicinal noble-metal surfaces both clean [336,337] and step-decorated [338], little is known about their dynamical properties [206,235]. The theoretical challenge for the future will be the extension of many-body calculations of quasiparticle dynamics to more complex systems such as quantum states in semimetals and their surfaces [339–343], quantum well states confined to a substrate surface [57,320], adatom- and molecule-induced states on metal substrates [344,345], spin-dependent quantum states on clean ferromagnetic surfaces [195,196,313–317] and these surfaces covered with molecules. This extension should be accompanied by analysis of the role of different approximations used in the theory, for instance, the role of non-linear effects in screening [346–350], the importance of vertex corrections in many-body calculations of the electron–electron contribution [16], and the role of short-range strong correlations [351] in quasiparticle dynamics. One can expect more first-principles calculations for electron and hole dynamics in surface states on metals. In conclusion, so much remains to be done in a very active research field.

Acknowledgements

References

[1] H.L. Dai, W. Ho (Eds.), Laser Spectroscopy and Photochemistry on Metal Surfaces, World Scientific, Singapore, 1995.
[2] H. Nienhaus, Surf. Sci. Rep. 45 (2002) 1.
[3] R. Haight, Surf. Sci. Rep. 21 (1995) 275.
[4] Th. Fauster, W. Steinmann, in: P. Halevi (Ed.), Photonic Probes of Surfaces, vol. 2 of Electromagnetic Waves: Recent Developments in Research, North-Holland, Amsterdam, 1995, Chapter 8, p. 347.
[5] S.G. Davison, M. Stęślicka, Basic Theory of Surface States, Oxford University Press, Oxford, 1992.
[6] R.M. Osgood Jr., X.Y. Wang, in: H. Ehrenreich, F. Spaepen (Eds.), Solid State Physics, vol. 51, Academic Press, San Diego, 1997, p. 1.
[7] P.M. Echenique, J.B. Pendry, J. Phys. C 11 (1978) 2065.

[8] P.M. Echenique, J.B. Pendry, Prog. Surf. Sci. 32 (1989) 111.
[9] I.E. Tamm, Z. Phys. 76 (1932) 849.
[10] I.E. Tamm, Phys. Z. Sowjet 1 (1932) 733.
[11] W. Shockley, Phys. Rev. 56 (1939) 317.
[12] P.O. Gartland, B.J. Slagsvold, Phys. Rev. B 12 (1975) 4047.
[13] L. Hedin, S. Lundqvist, Solid State Phys. 23 (1969) 1.
[14] G.D. Mahan, Comments Cond. Mater. Phys. 16 (1994) 333.
[15] F. Aryasetiawan, O. Gunnarsson, Rep. Prog. Phys. 61 (1998) 237.
[16] P.M. Echenique, J.M. Pitarke, E.V. Chulkov, A. Rubio, Chem. Phys. 251 (2000) 1.
[17] G.M. Eliashberg, Zh. Eksp. Teor. Fiz. 38 (1960) 966 [Sov. Phys. JETP 11 (1960) 696].
[18] G.M. Eliashberg, Zh. Eksp. Teor. Fiz. 43 (1962) 1005 [Sov. Phys. JETP 16 (1963) 780].
[19] G. Grimvall, in: E. Wohlfarth (Ed.), The Electron–Phonon Interaction in Metals, Selected Topics in Solid State Physics,
     North-Holland, New York, 1981.
[20] A.G. Borisov, A.K. Kazansky, J.P. Gauyacq, Phys. Rev. B 59 (1999) 10935.
[21] A.G. Borisov, J.P. Gauyacq, A.K. Kazansky, Surf. Sci. 505 (2002) 260.
[22] A.G. Borisov, A.K. Kazansky, J.P. Gauyacq, Surf. Sci. 526 (2003) 72.
[23] A.G. Borisov, J.P. Gauyacq, A.K. Kazansky, Surf. Sci. 540 (2003) 407.
[24] S.D. Kevan (Ed.), Angle-resolved Photoemission, vol. 74 of Studies in Surface Science and Catalysis, Elsevier,
     Amsterdam, 1992.
[25] S. Hüfner, Photoelectron Spectroscopy—Principles and Applications, vol. 82 of Springer Series in Solid-state Science,
     Springer, Berlin, 1995.
[26] W. Schattke, M.A. Van Hove, Solid-state Photoemission and Related Methods, Wiley/VCH, Weinheim, 2003.
[27] R. Matzdorf, Surf. Sci. Rep. 30 (1998) 153.
[28] V. Dose, Surf. Sci. Rep. 5 (1985) 337.
[29] N.V. Smith, Rep. Prog. Phys. 51 (1988) 1227.
[30] M. Donath, Surf. Sci. Rep. 20 (1994) 251.
[31] G. Binnig, H. Rohrer, Rev. Mod. Phys. 59 (1987) 615.
[32] J.A. Stroscio, W.J. Kaiser (Eds.), Scanning Tunneling Microscopy, Academic Press, San Diego, 1993.
[33] H.-J. Güntherodt, R. Wiesendanger (Eds.), Scanning Tunneling Microscopy, Springer, Berlin, 1994–1996.
[34] K. Giesen, F. Hage, F.J. Himpsel, H.J. Riess, W. Steinmann, Phys. Rev. Lett. 55 (1985) 300.
[35] R.W. Schoenlein, J.G. Fujimoto, G.L. Eesley, T.W. Capehart, Phys. Rev. Lett. 61 (1988) 2596.
[36] U. Höfer, I.L. Shumay, Ch. Reuß, U. Thomann, W. Wallauer, Th. Fauster, Science 277 (1997) 1480.
[37] J.P. Gauyacq, A.G. Borisov, A.K. Kazansky, Appl. Phys. A 78 (2004) 141.
[38] N.D. Lang, W. Kohn, Phys. Rev. B 7 (1973) 3541.
[39] P.M. Echenique, J.B. Pendry, Surf. Sci. 166 (1986) 69.
[40] F.J. García de Abajo, P.M. Echenique, Phys. Rev. B 45 (1992) 8771.
[41] M. Jonson, Solid State Commun. 33 (1980) 743.
[42] P.M. Echenique, A. Gras-Marti, J.R. Manson, R.H. Ritchie, Phys. Rev. B 35 (1987) 7357.
[43] I.D. White, R.W. Godby, M.M. Rieger, R.J. Needs, Phys. Rev. Lett. 80 (1998) 4265.
[44] E.V. Chulkov, V.M. Silkin, P.M. Echenique, Surf. Sci. 391 (1997) L1217.
[45] E.V. Chulkov, V.M. Silkin, P.M. Echenique, Surf. Sci. 437 (1999) 330.
[46] P. García-González, J.E. Alvarellos, E. Chacón, P. Tarazona, Int. J. Quant. Chem. 91 (2003) 139.
[47] B. Gumhalter, H. Petek, Surf. Sci. 445 (2000) 195.
[48] B. Gumhalter, Surf. Sci. 518 (2002) 81.
[49] M. Sakaue, T. Munakata, H. Kasai, A. Okiji, Surf. Sci. 507–510 (2002) 742.
[50] M. Sakaue, T. Munakata, H. Kasai, A. Okiji, Phys. Rev. B 66 (2002) 094302.
[51] M. Sakaue, T. Munakata, H. Kasai, A. Okiji, Phys. Rev. B 68 (2003) 205421.
[52] J. Kliewer, R. Berndt, E.V. Chulkov, V.M. Silkin, P.M. Echenique, S. Crampin, Science 288 (2000) 1399.
[53] E.V. Chulkov, V.M. Silkin, P.M. Echenique, Surf. Sci. 454–456 (2000) 458.
[54] V.M. Silkin, E.V. Chulkov, Fiz. Tverd. Tela 42 (2000) 1334 [Sov. Phys. Solid State 42 (2000) 1373].
[55] E.V. Chulkov, V.M. Silkin, M. Machado, Surf. Sci. 482–485 (2001) 693.

[56] P.M. Echenique, J. Osma, M. Machado, V.M. Silkin, E.V. Chulkov, J.M. Pitarke, Prog. Surf. Sci. 67 (2001) 271.
[57] E.V. Chulkov, J. Kliewer, R. Berndt, V.M. Silkin, B. Hellsing, S. Crampin, P.M. Echenique, Phys. Rev. B 68 (2003) 195422.
[58] S.G. Louie, Phys. Rev. Lett. 40 (1978) 1525.
[59] L. Ley, G.P. Kerker, N. Mårtensson, Phys. Rev. B 23 (1981) 2710.
[60] E.V. Chulkov, V.M. Silkin, E.N. Shirykalov, Surf. Sci. 188 (1987) 287.
[61] J. Inglesfield, G.A. Benesh, Phys. Rev. B 37 (1988) 6682.
[62] E.V. Chulkov, V.M. Silkin, Surf. Sci. 215 (1989) 385.
[63] G.A. Benesh, J.R. Hester, Surf. Sci. 194 (1988) 567.
[64] C. Stampfl, K. Kambe, R. Fasel, P. Aebi, M. Scheffler, Phys. Rev. B 57 (1998) 15251.
[65] J.M. Carlsson, B. Hellsing, Phys. Rev. B 61 (2000) 13973.
[66] V.M. Silkin, E.V. Chulkov, P.M. Echenique, Phys. Rev. B 64 (2001) 172512.
[67] E.T. Goodwin, Proc. Camb. Phil. Soc. 35 (1939) 205.
[68] S. Link, H.A. Dürr, G. Bihlmayer, S. Blügel, W. Eberhardt, E.V. Chulkov, V.M. Silkin, P.M. Echenique, Phys. Rev. B 63 (2001) 115420.
[69] I. Sarría, J. Osma, E.V. Chulkov, J.M. Pitarke, P.M. Echenique, Phys. Rev. B 60 (1999) 11795.
[70] M. García Vergniory, Ph.D. Thesis, University of the Basque Country, 2003.
[71] J.J. Quinn, R.A. Ferrell, Phys. Rev. 112 (1958) 812.
[72] R.H. Ritchie, Phys. Rev. 114 (1959) 644.
[73] J. Lindhard, K. Dan. Vidensk. Selsk. Mat. Phys. Medd. 28 (1954) 1.
[74] J.J. Quinn, Appl. Phys. Lett. 2 (1963) 167.
[75] A. García-Lekue, J.M. Pitarke, E.V. Chulkov, A. Liebsch, P.M. Echenique, Phys. Rev. B 68 (2003) 045103.
[76] J.J. Quinn, Phys. Rev. 126 (1962) 1453.
[77] A. Liebsch, Electronic Excitations at Metal Surfaces, Plenum Press, New York, 1997.
[78] C. López-Bastidas, J.A. Maytorena, A. Liebsch, Phys. Rev. B 65 (2001) 035417.
[79] A. García-Lekue, J.M. Pitarke, E.V. Chulkov, A. Liebsch, P.M. Echenique, Phys. Rev. Lett. 89 (2002) 096401.
[80] M.C. Payne, M.P. Teter, D.C. Allan, T.A. Arias, J.D. Joannopoulos, Rev. Mod. Phys. 64 (1992) 1045.
[81] N.W. Ashcroft, N.D. Mermin, Solid State Physics, Saunders College, Philadelphia, 1976.
[82] R.H. Ritchie, A.L. Marusak, Surf. Sci. 4 (1966) 234.
[83] P.M. Echenique, F.J. García de Abajo, V.H. Ponce, M.E. Uranga, Nucl. Instrum. Meth. Phys. Res. B 96 (1995) 583.
[84] E.V. Chulkov, M. Machado, V.M. Silkin, Vacuum 61 (2001) 95.
[85] P.M. Echenique, J. Osma, V.M. Silkin, E.V. Chulkov, J.M. Pitarke, Appl. Phys. A 71 (2000) 503.
[86] F. Theilmann, R. Matzdorf, G. Meister, A. Goldmann, Phys. Rev. B 56 (1997) 3632.
[87] B. Hellsing, A. Eiguren, E.V. Chulkov, J. Phys.: Condens. Matter 14 (2002) 5959.
[88] E.G. Maksimov, D.Yu. Savrasov, S.Yu. Savrasov, Phys. Usp. 40 (1997) 337.
[89] A. Eiguren, S. deGironcoli, E.V. Chulkov, P.M. Echenique, E. Tosatti, Phys. Rev. Lett. 91 (2003) 166803.
[90] W. Kress, F.W. de Wette (Eds.), Surface Phonons, vol. 21 of Springer Series in Surface Sciences, Springer, Berlin, 1991.
[91] J.S. Nelson, E.C. Sowa, M.S. Daw, Phys. Rev. Lett. 61 (1988) 1977.
[92] T.S. Rahman, J.D. Spangler, A. Al-Rawi, Surf. Sci. 502–503 (2002) 429.
[93] I.Yu. Sklyadneva, G.G. Rusina, E.V. Chulkov, Surf. Sci. 416 (1998) 17.
[94] N.W. Ashcroft, Phys. Lett. 23 (1966) 48.
[95] A. Eiguren, B. Hellsing, F. Reinert, G. Nicolay, E.V. Chulkov, V.M. Silkin, S. Hüfner, P.M. Echenique, Phys. Rev. Lett. 88 (2002) 066805.
[96] A. Eiguren, B. Hellsing, E.V. Chulkov, P.M. Echenique, Phys. Rev. B 67 (2003) 235423.
[97] B. Hellsing, A. Eiguren, F. Reinert, G. Nicolay, E.V. Chulkov, V.M. Silkin, S. Hüfner, P.M. Echenique, J. Electron Spectrosc. Relat. Phenom. 129 (2003) 97.
[98] V.N. Kostur, B. Mitrović, Phys. Rev. B 48 (1993) 16388.
[99] B.A. McDougall, T. Balasubramanian, E. Jensen, Phys. Rev. B 51 (1995) 13891.
[100] F. Reinert, G. Nicolay, S. Schmidt, D. Ehm, S. Hüfner, Phys. Rev. B 63 (2001) 115415.
[101] A. Eiguren, B. Hellsing, E.V. Chulkov, P.M. Echenique, J. Electron Spectrosc. Relat. Phenom. 129 (2003) 111.

[102] E.D. Hansen, T. Miller, T.-C. Chiang, Phys. Rev. Lett. 80 (1998) 1766.
[103] T.-C. Chiang, Chem. Phys. 251 (2000) 133.
[104] T. Michalke, A. Gerlach, K. Berge, R. Matzdorf, A. Goldmann, Phys. Rev. B 62 (2000) 10544.
[105] P.O. Nilsson, N. Dahlbäck, Solid State Commun. 29 (1979) 303.
[106] F.J. Himpsel, W. Eberhardt, Solid State Commun. 31 (1979) 747.
[107] B.J. Slagsvold, J.K. Grepstadt, P.O. Gartland, Physica Scripta T 4 (1983) 65.
[108] J.K. Grepstadt, B.J. Slagsvold, I. Bartos, J. Phys. F 12 (1982) 1679.
[109] N.V. Smith, P. Thiry, Y. Petroff, Phys. Rev. B 47 (1993) 15476.
[110] H.I. Starnberg, H.E. Brauer, P.O. Nilsson, Phys. Rev. B 48 (1993) 621.
[111] R. Matzdorf, A. Goldmann, J. Braun, G. Borstel, Solid State Commun. 91 (1994) 163.
[112] A. Goldmann, W. Altmann, V. Dose, Solid State Commun. 79 (1991) 511.
[113] K. Berge, A. Gerlach, G. Meister, A. Goldmann, J. Braun, Surf. Sci. 498 (2002) 1.
[114] S.D. Kevan, Phys. Rev. Lett. 50 (1983) 526.
[115] J. Tersoff, S.D. Kevan, Phys. Rev. B 28 (1983) 4267.
[116] R. Paniago, R. Matzdorf, G. Meister, A. Goldmann, Surf. Sci. 336 (1995) 113.
[117] Th. Fauster, Ch. Reuß, I.L. Shumay, M. Weinelt, F. Theilmann, A. Goldmann, Phys. Rev. B 61 (2000) 16168.
[118] F. Theilmann, R. Matzdorf, A. Goldmann, Surf. Sci. 420 (1999) 33.
[119] A. Beckmann, K. Meinel, M. Heiler, Ch. Ammer, H. Neddermeyer, Phys. Stat. Sol. b 198 (1996) 665.
[120] A. Beckmann, K. Meinel, Ch. Ammer, M. Heiler, H. Neddermeyer, Surf. Sci. 375 (1997) L363.
[121] G. Nicolay, F. Reinert, S. Schmidt, D. Ehm, P. Steiner, S. Hüfner, Phys. Rev. B 62 (2000) 1631.
[122] G. Nicolay, F. Reinert, S. Hüfner, P. Blaha, Phys. Rev. B 65 (2002) 033407.
[123] P. Heimann, H. Neddermeyer, H.F. Roloff, J. Phys. C 10 (1977) L17.
[124] S.D. Kevan, R.H. Gaylord, Phys. Rev. B 36 (1987) 5809.
[125] M. Pivetta, F. Silly, F. Patthey, J.P. Pelz, W.-D. Schneider, Phys. Rev. B 67 (2003) 193402.
[126] S. LaShell, E. Jensen, T. Balasubramanian, Phys. Rev. B 61 (2000) 2371.
[127] P. Straube, F. Pforte, T. Michalke, K. Berge, A. Gerlach, A. Goldmann, Phys. Rev. B 61 (2000) 14072.
[128] Landolt-Börnstein, New Series, Group III, vol. 24b, Springer, Heidelberg, 1994.
[129] R. Matzdorf, G. Meister, A. Goldmann, Phys. Rev. B 54 (1996) 14807.
[130] D. Purdie, M. Hengsberger, M. Garnier, Y. Baer, Surf. Sci. 407 (1998) L671.
[131] D.-A. Luh, J.J. Paggel, T. Miller, T.-C. Chiang, Phys. Rev. Lett. 84 (2000) 3410.
[132] H. Petek, H. Nagano, S. Ogawa, Phys. Rev. Lett. 83 (1999) 832.
[133] H. Petek, H. Nagano, S. Ogawa, Appl. Phys. B 68 (1999) 369.
[134] A. Gerlach, K. Berge, A. Goldmann, I. Campillo, A. Rubio, J.M. Pitarke, P.M. Echenique, Phys. Rev. B 64 (2001) 085423.
[135] A. Gerlach, K. Berge, T. Michalke, A. Goldmann, R. Müller, C. Janowitz, Surf. Sci. 497 (2002) 311.
[136] I. Campillo, A. Rubio, J.M. Pitarke, A. Goldmann, P.M. Echenique, Phys. Rev. Lett. 85 (2000) 3241.
[137] V.P. Zhukov, F. Aryasetiawan, E.V. Chulkov, I.G. d Gurtubay, P.M. Echenique, Phys. Rev. B 64 (2001) 195122.
[138] T. Valla, A.V. Fedorov, P.D. Johnson, S.L. Hulbert, Phys. Rev. Lett. 83 (1999) 2085.
[139] F. Reinert, B. Eltner, G. Nicolay, D. Ehm, S. Schmidt, S. Hüfner, Phys. Rev. Lett. 91 (2003) 186406.
[140] T. Balasubramanian, E. Jensen, X.L. Wu, S.L. Hulbert, Phys. Rev. B 57 (1998) R6866.
[141] M. Hengsberger, D. Purdie, P. Segovia, M. Garnier, Y. Baer, Phys. Rev. Lett. 83 (1999) 592.
[142] M. Hengsberger, R. Frésard, D. Purdie, P. Segovia, Y. Baer, Phys. Rev. B 60 (1999) 10796.
[143] V.M. Silkin, T. Balasubramanian, E.V. Chulkov, A. Rubio, P.M. Echenique, Phys. Rev. B 64 (2001) 085334.
[144] U.O. Karlsson, S.A. Flödstrom, R. Engelhardt, W. Gädecke, E.E. Koch, Solid State Commun. 49 (1984) 711.
[145] R.A. Bartynski, E. Jensen, T. Gustafsson, E.W. Plummer, Phys. Rev. B 32 (1985) 1921.
[146] T. Balasubramanian, L.I. Johansson, P.-A. Glans, C. Virojanadara, V.M. Silkin, E.V. Chulkov, P.M. Echenique, Phys. Rev. B 64 (2001) 205401.
[147] S.-J. Tang, Ismail, P.T. Sprunger, E.W. Plummer, Phys. Rev. B 65 (2002) 235428.
[148] H.J. Levinson, F. Greuter, E.W. Plummer, Phys. Rev. B 27 (1983) 727.
[149] S.D. Kevan, N.G. Stoffel, N.V. Smith, Phys. Rev. B 31 (1985) 1788.
[150] R.A. Bartynski, R.H. Gaylord, T. Gustafsson, E.W. Plummer, Phys. Rev. B 33 (1986) 3644.

[151] A. Carlsson, B. Hellsing, S.Å. Lindgren, L. Walldén, Phys. Rev. B 56 (1997) 1593.
[152] T.-C. Chiang, Surf. Sci. Rep. 39 (2000) 181.
[153] M. Milun, P. Pervan, D.P. Woodruff, Rep. Prog. Phys. 65 (2001) 99.
[154] R.C. Jaklevic, J. Lambe, M. Mikor, W. Vassel, Phys. Rev. Lett. 26 (1971) 88.
[155] S.Å. Lindgren, L. Walldén, Solid State Commun. 34 (1980) 671.
[156] S.Å. Lindgren, L. Walldén, Phys. Rev. Lett. 59 (1987) 3003.
[157] S.Å. Lindgren, L. Walldén, Phys. Rev. B 45 (1992) 6345.
[158] J.J. Paggel, T. Miller, T.-C. Chiang, Phys. Rev. Lett. 81 (1998) 5632.
[159] J.J. Paggel, T. Miller, T.-C. Chiang, Phys. Rev. Lett. 83 (1999) 1415.
[160] M. Milun, P. Pervan, B. Gumhalter, D.P. Woodruff, Phys. Rev. B 59 (1999) 5170.
[161] M. Kralj, A. Šiber, P. Pervan, M. Milun, T. Valla, P.D. Johnson, D.P. Woodruff, Phys. Rev. B 64 (2001) 085411.
[162] W. Jacob, E. Bertel, V. Dose, Phys. Rev. B 35 (1987) 5910.
[163] D. Heskett, K.-H. Frank, E.E. Koch, H.-J. Freund, Phys. Rev. B 36 (1987) 1276.
[164] K.-H. Frank, H.-J. Sagner, D. Heskett, Phys. Rev. B 40 (1989) 2767.
[165] D. Tang, K.H. Frank, B. Reihl, Phys. Rev. B 41 (1990) 4897.
[166] R. Dudde, L.S.O. Johansson, B. Reihl, Phys. Rev. B 44 (1991) 1198.
[167] N. Memmel, G. Rangelov, E. Bertel, V. Dose, Phys. Rev. B 43 (1991) 6938.
[168] E. Bertel, Appl. Phys. A 53 (1991) 356.
[169] R. Dudde, B. Reihl, Surf. Sci. 287–288 (1993) 614.
[170] D. Tang, C. Su, D. Heskett, Surf. Sci. 295 (1993) 427.
[171] N. Memmel, G. Rangelov, E. Bertel, Surf. Sci. 285 (1993) 109.
[172] N. Fischer, S. Schuppler, R. Fischer, Th. Fauster, W. Steinmann, Phys. Rev. B 43 (1991) 14722.
[173] N. Fischer, S. Schuppler, R. Fischer, Th. Fauster, W. Steinmann, Phys. Rev. B 47 (1993) 4705.
[174] N. Fischer, S. Schuppler, Th. Fauster, W. Steinmann, Surf. Sci. 314 (1994) 89.
[175] S. Ogawa, H. Nagano, H. Petek, Phys. Rev. Lett. 88 (2002) 116801.
[176] L.C. Davis, M.P. Everson, R.C. Jaklevic, W. Shen, Phys. Rev. B 43 (1991) 3821.
[177] Y. Hasegawa, P. Avouris, Phys. Rev. Lett. 71 (1993) 1071.
[178] M.F. Crommie, C.P. Lutz, D.M. Eigler, Nature 363 (1993) 524.
[179] M.F. Crommie, C.P. Lutz, D.M. Eigler, Science 262 (1993) 218.
[180] J. Li, W.-D. Schneider, R. Berndt, S. Crampin, Phys. Rev. Lett. 80 (1998) 3332.
[181] J. Kliewer, R. Berndt, Phys. Rev. B 65 (2002) 035412.
[182] N.D. Lang, Phys. Rev. Lett. 58 (1987) 45.
[183] E.N. Economou, Green's Functions for Quantum Physics, Springer-Verlag, Berlin, 1983.
[184] P. Avouris, I.-W. Lyo, R.E. Walkup, Y. Hasegawa, J. Vac. Sci. Technol. B 12 (1994) 1447.
[185] N.D. Lang, Phys. Rev. B 34 (1986) 5947.
[186] J. Li, W.-D. Schneider, R. Berndt, Phys. Rev. B 56 (1997) 7656.
[187] J. Li, W.-D. Schneider, R. Berndt, O.R. Bryant, S. Crampin, Phys. Rev. Lett. 81 (1998) 4464.
[188] A. Zawadowski, Phys. Rev. 163 (1967) 341.
[189] J.A. Appelbaum, W.F. Brinkman, Phys. Rev. 186 (1969) 464.
[190] G. Hörmandinger, Phys. Rev. B 49 (1994) 13897.
[191] S. Crampin, J. Phys.: Condens. Matter 5 (1993) 4647.
[192] L. Vitali, P. Wahl, M.A. Schneider, K. Kern, V.M. Silkin, E.V. Chulkov, P.M. Echenique, Surf. Sci. 523 (2003) L47.
[193] J. Klein, A. Léger, M. Belin, D. Défourneau, M.J.L. Sangster, Phys. Rev. B 7 (1973) 2336.
[194] L. Limot, T. Maroutian, P. Johansson, R. Berndt, Phys. Rev. Lett. 91 (2003) 196801.
[195] A. Bauer, A. Mühlig, D. Wegner, G. Kaindl, Phys. Rev. B 65 (2002) 075421.
[196] A. Rehbein, D. Wegner, G. Kaindl, A. Bauer, Phys. Rev. B 67 (2003) 033403.
[197] J. Kliewer, Ph.D. Thesis, RWTH, Aachen, Germany, 2000.
[198] J. Kliewer, R. Berndt, S. Crampin, New J. Phys. 3 (2001) 22.
[199] E.J. Heller, M.F. Crommie, C.P. Lutz, D.M. Eigler, Nature 369 (1994) 464.
[200] S. Crampin, M.H. Boon, J.E. Inglesfield, Phys. Rev. Lett. 73 (1994) 1015.
[201] S. Crampin, O.R. Bryant, Phys. Rev. B 54 (1996) R17367.

[202] L. Bürgi, O. Jeandupeux, H. Brune, K. Kern, Phys. Rev. Lett. 82 (1999) 4516.
[203] O. Jeandupeux, L. Bürgi, A. Hirstein, H. Brune, K. Kern, Phys. Rev. B 59 (1999) 15926.
[204] D. Pines, P. Nozieres, The Theory of Quantum Liquids, Benjamin, New York, 1969.
[205] P. Wahl, M.A. Schneider, L. Diekhöner, R. Vogelgesang, K. Kern, Phys. Rev. Lett. 91 (2003) 106802.
[206] M. Roth, M. Weinelt, Th. Fauster, P. Wahl, M.A. Schneider, L. Diekhöner, K. Kern, Appl. Phys. A 78 (2004) 155.
[207] K.-F. Braun, K.-H. Rieder, Phys. Rev. Lett. 88 (2002) 096801.
[208] K.-F. Braun, Private communication (unpublished).
[209] C.-P. Huang, M.T. Asaki, S. Backus, M.M. Murnane, H.C. Kapteyn, H. Nathel, Opt. Lett. 17 (1992) 1289.
[210] A. Baltuška, Z. Wei, M.S. Pshenichnikov, D.A. Wiersma, Opt. Lett. 22 (1997) 102.
[211] L. Xu, G. Tempea, A. Poppe, M. Lenzner, C. Spielmann, F. Krausz, A. Stingl, K. Ferencz, Appl. Phys. B 65 (1997) 151.
[212] S. Ogawa, H. Nagano, H. Petek, A.P. Heberle, Phys. Rev. Lett. 78 (1997) 1339.
[213] R.W. Schoenlein, J.G. Fujimoto, G.L. Eesley, T.W. Capehart, Phys. Rev. B 41 (1990) 5436.
[214] R.W. Schoenlein, J.G. Fujimoto, G.L. Eesley, T.W. Capehart, Phys. Rev. B 43 (1991) 4688.
[215] D.F. Padowitz, W.R. Merry, R.E. Jordan, C.B. Harris, Phys. Rev. Lett. 69 (1992) 3583.
[216] S. Schuppler, N. Fischer, Th. Fauster, W. Steinmann, Appl. Phys. A 51 (1990) 322.
[217] T. Hertel, E. Knoesel, M. Wolf, G. Ertl, Phys. Rev. Lett. 76 (1996) 535.
[218] I.L. Shumay, U. Höfer, Ch. Reuß, U. Thomann, W. Wallauer, Th. Fauster, Phys. Rev. B 58 (1998) 13974.
[219] Th. Fauster, Surf. Sci. 507–510 (2002) 256.
[220] Th. Fauster, in: W. Schattke, M.A. Van Hove (Eds.), Solid-state Photoemission and Related Methods, Wiley/VCH, Weinheim, 2003, Chapter 8, p. 247.
[221] E. Knoesel, A. Hotzel, M. Wolf, J. Electron Spectrosc. Relat. Phenom. 88–91 (1998) 577.
[222] K. Boger, M. Weinelt, Th. Fauster, Phys. Rev. Lett. 92 (2004) 126803.
[223] T. Hertel, E. Knoesel, A. Hotzel, M. Wolf, G. Ertl, J. Vac. Sci. Technol. A 15 (1997) 1503.
[224] Ch. Reuß, I.L. Shumay, U. Thomann, M. Kutschera, M. Weinelt, Th. Fauster, U. Höfer, Phys. Rev. Lett. 82 (1999) 153.
[225] A. Schäfer, I.L. Shumay, M. Wiets, M. Weinelt, Th. Fauster, E.V. Chulkov, V.M. Silkin, P.M. Echenique, Phys. Rev. B 61 (2000) 13159.
[226] Ch. Reuß, W. Wallauer, Th. Fauster, Surf. Rev. Lett. 3 (1996) 1547.
[227] W. Wallauer, Th. Fauster, Surf. Sci. 374 (1997) 44.
[228] H. Petek, S. Ogawa, Prog. Surf. Sci. 56 (1997) 239.
[229] S.L. Hulbert, P.D. Johnson, M. Weinert, Phys. Rev. B 34 (1986) 3670.
[230] R. Fischer, S. Schuppler, N. Fischer, Th. Fauster, W. Steinmann, Phys. Rev. Lett. 70 (1993) 654.
[231] W. Berthold, U. Höfer, P. Feulner, E.V. Chulkov, V.M. Silkin, P.M. Echenique, Phys. Rev. Lett. 88 (2002) 056805.
[232] W. Berthold, J. Güdde, P. Feulner, U. Höfer, Appl. Phys. B 73 (2001) 865.
[233] K. Boger, M. Weinelt, J. Wang, Th. Fauster, Appl. Phys. A 78 (2004) 161.
[234] M. Roth, M. Pickel, J. Wang, M. Weinelt, Th. Fauster, Phys. Rev. Lett. 88 (2002) 096802.
[235] M. Roth, M. Pickel, M. Weinelt, Th. Fauster, Appl. Phys. A 78 (2004) 149.
[236] T. Klamroth, P. Saalfrank, U. Höfer, Phys. Rev. B 64 (2001) 035420.
[237] E.W. Plummer, Science 277 (1997) 1447.
[238] U. Höfer, Appl. Phys. B 68 (1999) 383.
[239] Th. Fauster, Ch. Reuß, I.L. Shumay, M. Weinelt, Chem. Phys. 251 (2000) 111.
[240] K. Blum, Density Matrix Theory and Applications, Plenum Press, New York, 1983.
[241] R. Loudon, The Quantum Theory of Light, Oxford University Press, New York, 1983.
[242] K. Boger, M. Roth, M. Weinelt, Th. Fauster, P.-G. Reinhard, Phys. Rev. B 65 (2002) 075104.
[243] M. Wolf, A. Hotzel, E. Knoesel, D. Velic, Phys. Rev. B 59 (1999) 5926.
[244] M. Weinelt, J. Phys.: Condens. Matter 14 (2002) R1099.
[245] S. Schuppler, N. Fischer, Th. Fauster, W. Steinmann, Phys. Rev. B 46 (1992) 13539 (Erratum: Phys. Rev. B 47 (1993) 10058).
[246] W. Wallauer, R. Fischer, Th. Fauster, Surf. Sci. 364 (1996) 297.
[247] M. Weinelt, Ch. Reuß, M. Kutschera, U. Thomann, I.L. Shumay, Th. Fauster, U. Höfer, F. Theilmann, A. Goldmann, Appl. Phys. B 68 (1999) 377.
[248] M. Roth, M. Pickel, J. Wang, M. Weinelt, Th. Fauster, Appl. Phys. B 74 (2002) 661.

[249] R. Fischer, Th. Fauster, Phys. Rev. B 51 (1995) 7112.

[250] N.-H. Ge, C.M. Wong, R.L. Lingle Jr., J.D. McNeill, K.J. Gaffney, C.B. Harris, Science 279 (1998) 202.

[251] U. Höfer, Science 279 (1998) 190.

[252] A.D. Miller, I. Bezel, K.J. Gaffney, S. Garrett-Roe, S.H. Liu, P. Szymanski, C.B. Harris, Science 297 (2002) 1163.

[253] S.H. Liu, A.D. Miller, K.J. Gaffney, P. Szymanski, S. Garrett-Roe, I. Bezel, C.B. Harris, J. Phys. Chem. B 106 (2002) 12908.

[254] C. Gahl, U. Bovensiepen, C. Frischkorn, M. Wolf, Phys. Rev. Lett. 89 (2002) 107402.

[255] U. Höfer, M.J. Breitschafter, E. Umbach, Phys. Rev. Lett. 64 (1990) 3050.

[256] M. Bertolo, W. Hansen, K. Jacobi, Phys. Rev. Lett. 67 (1991) 1898.

[257] C. Keller, M. Stichler, G. Comelli, F. Esch, S. Lizzit, Z.W. Gortel, W. Wurth, D. Menzel, Phys. Rev. B 60 (1999) 16143.

[258] C.B. Harris, J.D. McNeill, N.-H. Ge, R.E. Jordan, R.L. Lingle Jr., C.M. Wong, in: P.F. Barbara (Ed.), Ultrafast Phenomena X, Springer, Berlin, 1996, p. 445.

[259] C.M. Wong, J.D. McNeill, K.J. Gaffney, N.-H. Ge, A.D. Miller, S.H. Liu, C.B. Harris, J. Phys. Chem. B 103 (1999) 282.

[260] R.L. Lingle Jr., N.-H. Ge, R.E. Jordan, J.D. McNeill, C.B. Harris, Chem. Phys. 205 (1996) 191.

[261] N.-H. Ge, C.M. Wong, C.B. Harris, Acc. Chem. Res. 33 (2000) 111.

[262] M. Wolf, E. Knoesel, T. Hertel, Phys. Rev. B 54 (1996) R5295.

[263] A. Hotzel, G. Moos, K. Ishioka, M. Wolf, G. Ertl, Appl. Phys. B 68 (1999) 615.

[264] A. Hotzel, K. Ishioka, E. Knoesel, M. Wolf, G. Ertl, Chem. Phys. Lett. 285 (1998) 271.

[265] H. Wang, G. Dutton, X.-Y. Zhu, J. Phys. Chem. B 104 (2000) 10332.

[266] W. Berthold, I.L. Shumay, P. Feulner, U. Höfer, in: T. Elsaesser, J.G. Fujimoto, D.A. Wiersma, W. Zinth (Eds.), Ultrafast Phenomena XI, Springer, Berlin, 1998, p. 330.

[267] W. Berthold, U. Höfer, P. Feulner, D. Menzel, Chem. Phys. 251 (2000) 123.

[268] W. Berthold, P. Feulner, U. Höfer, Chem. Phys. Lett. 358 (2002) 502.

[269] D.C. Marinica, C. Ramseyer, A.G. Borisov, D. Teillet-Billy, J. Gauyacq, W. Berthold, P. Feulner, U. Höfer, Phys. Rev. Lett. 89 (2002) 046802.

[270] C.B. Harris, N.-H. Ge, R.L. Lingle Jr., J.D. McNeill, C.M. Wong, Annu. Rev. Phys. Chem. 48 (1997) 711.

[271] M.W. Cole, Phys. Rev. B 3 (1971) 4418.

[272] J.D. McNeill, R.L. Lingle Jr., N.-H. Ge, C.M. Wong, R.E. Jordan, C.B. Harris, Phys. Rev. Lett. 79 (1997) 4645.

[273] W. Berthold, F. Rebentrost, P. Feulner, U. Höfer, Appl. Phys. A 78 (2004) 131.

[274] D.C. Marinica, C. Ramseyer, A.G. Borisov, D. Teillet-Billy, J. Gauyacq, Surf. Sci. 528 (2003) 78.

[275] D.C. Marinica, C. Ramseyer, A.G. Borisov, D. Teillet-Billy, J. Gauyacq, Surf. Sci. 540 (2003) 457.

[276] M. Machado, E.V. Chulkov, V.M. Silkin, U. Höfer, P. Echenique, Prog. Surf. Sci. 74 (2003) 219.

[277] J.P. Gauyacq, A.G. Borisov, G. Raşeev, Surf. Sci. 490 (2001) 99.

[278] P. Feulner, D. Menzel, in: H.-L. Dai, W. Ho (Eds.), Laser Spectroscopy and Photochemistry on Metal Surfaces, World Scientific, Singapore, 1995, p. 627.

[279] W. Wurth, D. Menzel, Chem. Phys. 251 (2000) 141.

[280] L. Bartels, G. Meyer, K.-H. Rieder, D. Velic, E. Knoesel, A. Hotzel, M. Wolf, G. Ertl, Phys. Rev. Lett. 80 (1998) 2004.

[281] S. Ogawa, H. Nagano, H. Petek, Phys. Rev. Lett. 82 (1999) 1931.

[282] M. Bauer, S. Pawlik, M. Aeschlimann, Phys. Rev. B 55 (1997) 10040.

[283] M. Bauer, S. Pawlik, M. Aeschlimann, Phys. Rev. B 60 (1999) 5016.

[284] H. Petek, M.J. Weida, H. Nagano, S. Ogawa, Surf. Sci. 451 (2000) 22.

[285] H. Petek, S. Ogawa, Annu. Rev. Phys. Chem. 53 (2002) 507.

[286] A.G. Borisov, J.P. Gauyacq, A.K. Kazansky, E.V. Chulkov, V.M. Silkin, P.M. Echenique, Phys. Rev. Lett. 86 (2001) 488.

[287] H. Petek, M.J. Weida, H. Nagano, S. Ogawa, Science 288 (2000) 1402.

[288] H. Petek, H. Nagano, M.J. Weida, S. Ogawa, J. Phys. Chem. B 105 (2001) 6767.

[289] C. Gahl, K. Ishioka, Q. Zhong, A. Hotzel, M. Wolf, Faraday Discuss. 117 (2000) 191.

[290] T. Vondrak, X.-Y. Zhu, J. Phys. Chem. B 103 (1999) 3449.

[291] D. Velic, A. Hotzel, M. Wolf, G. Ertl, J. Chem. Phys. 109 (1998) 9155.

[292] T. Munakata, Surf. Sci. 454–456 (2000) 118.

[293] K.J. Gaffney, C.M. Wong, S.H. Liu, A.D. Miller, J.D. McNeill, C.B. Harris, Chem. Phys. 251 (2000) 99.
[294] X.Y. Zhu, Annu. Rev. Phys. Chem. 53 (2002) 221.
[295] R. Keyling, W.D. Schöne, W. Ekardt, Chem. Phys. Lett. 354 (2002) 376.
[296] A.V. Chaplik, Z. Eksp. Teor. Fiz. 60 (1971) 1845 [Sov. Phys. JETP 33 (1971) 997].
[297] G.F. Giuliani, J.J. Quinn, Phys. Rev. B 26 (1982) 4421.
[298] P.M. Echenique, F. Flores, F. Sols, Phys. Rev. Lett. 55 (1985) 2348.
[299] P.L. de Andrés, P.M. Echenique, F. Flores, Phys. Rev. B 35 (1987) 4529.
[300] P.L. de Andrés, P.M. Echenique, F. Flores, Phys. Rev. B 39 (1989) 10356.
[301] E.V. Chulkov, I. Sarría, V.M. Silkin, J.M. Pitarke, P.M. Echenique, Phys. Rev. Lett. 80 (1998) 4947.
[302] J. Osma, I. Sarría, E.V. Chulkov, J.M. Pitarke, P.M. Echenique, Phys. Rev. B 59 (1999) 10591.
[303] J. Lehmann, M. Merschdorf, A. Thon, S. Voll, W. Pfeiffer, Phys. Rev. B 60 (1999) 17037.
[304] S. Link, J. Sievers, H.A. Dürr, W. Eberhardt, J. Electron Spectrosc. Relat. Phenom. 114–116 (2001) 351.
[305] X.J. Shen, H. Kwak, A.M. Radojevic, S. Smadici, D. Mocuta, R.M. Osgood Jr., Chem. Phys. Lett. 351 (2002) 1.
[306] M. Wolf, Private communication (unpublished).
[307] E.V. Chulkov, J. Osma, I. Sarría, V.M. Silkin, J.M. Pitarke, Surf. Sci. 433–435 (1999) 882.
[308] H.-S. Rhie, S. Link, H.A. Dürr, W. Eberhardt, N.V. Smith, Phys. Rev. B 68 (2003) 033410.
[309] A. Liebsch, Phys. Rev. Lett. 71 (1993) 145.
[310] G. Ferrini, C. Giannetti, D. Fausti, G. Galimberti, M. Peloi, G. Banfi, F. Parmigiani, Phys. Rev. B 67 (2003) 235407.
[311] F. Passek, M. Donath, K. Ertl, V. Dose, Phys. Rev. Lett. 75 (1995) 2746.
[312] U. Thomann, Ch. Reuß, Th. Fauster, F. Passek, M. Donath, Phys. Rev. B 61 (2000) 16163.
[313] U. Thomann, I.L. Shumay, M. Weinelt, Th. Fauster, Appl. Phys. B 68 (1999) 531.
[314] W. Wallauer, Th. Fauster, Phys. Rev. B 54 (1996) 5086.
[315] A.V. Fedorov, T. Valla, F. Liu, P.D. Johnson, M. Weinert, P.B. Allen, Phys. Rev. B 65 (2002) 212409.
[316] M. Donath, B. Gubanka, F. Passek, Phys. Rev. Lett. 77 (1996) 5138.
[317] P.B. Allen, Phys. Rev. B 63 (2001) 214410.
[318] A. Hotzel, M. Wolf, J.P. Gauyacq, J. Phys. Chem. B 104 (2000) 8438.
[319] G. Benedek, J. Ellis, A. Reichmuth, P. Ruggerone, H. Schief, J.P. Toennies, Phys. Rev. Lett. 69 (1992) 2951.
[320] B. Hellsing, J. Carlsson, L. Walldén, S.Å. Lindgren, Phys. Rev. B 61 (2000) 2343.
[321] N.D. Lang, A.R. Williams, Phys. Rev. B 18 (1978) 616.
[322] P. Nordlander, J.C. Tully, Phys. Rev. B 42 (1990) 5564.
[323] A.G. Borisov, D. Teillet-Billy, J.P. Gauyacq, H. Winter, G. Dierkes, Phys. Rev. B 54 (1996) 17166.
[324] J.P. Gauyacq, A.G. Borisov, G. Raşeev, A.K. Kazansky, Faraday Discuss. 117 (2000) 15.
[325] A.G. Borisov, A.K. Kazansky, J.P. Gauyacq, Phys. Rev. B 64 (2001) 201105.
[326] A.G. Borisov, A.K. Kazansky, J.P. Gauyacq, Phys. Rev. Lett. 80 (1998) 1996.
[327] A.G. Borisov, A.K. Kazansky, J.P. Gauyacq, Surf. Sci. 430 (1999) 165.
[328] A.G. Borisov, J.P. Gauyacq, E.V. Chulkov, V.M. Silkin, P.M. Echenique, Phys. Rev. B 65 (2002) 235434.
[329] D. Sánchez Portal, in: Proceedings of the Symposium on Surface Science 3S03, La Plagne, Centre UCPA-Savoie, France, 2003.
[330] H. Hövel, B. Grimm, B. Reihl, Surf. Sci. 477 (2001) 43.
[331] D.-A. Luh, T. Miller, J.J. Paggel, T.-C. Chiang, Phys. Rev. Lett. 88 (2002) 256802.
[332] K. Takahashi, A. Tanaka, M. Hatano, H. Sasaki, S. Suzuki, S. Sato, Surf. Sci. 433–435 (1999) 873.
[333] T. Valla, M. Kralj, A. Šiber, M. Milun, P. Pervan, P.D. Johnson, D.P. Woodruff, J. Phys.: Condens. Matter 12 (2000) L477.
[334] R.A. DiDio, E.W. Plummer, W.R. Graham, Phys. Rev. Lett. 52 (1984) 683.
[335] R. Matzdorf, A. Goldmann, Surf. Sci. 412–413 (1998) 61.
[336] J.E. Ortega, A. Mugarza, V. Repain, S. Rousset, V. Pérez-Dieste, A. Mascaraque, Phys. Rev. B 65 (2002) 165413.
[337] A. Mugarza, A. Mascaraque, V. Repain, S. Rousset, K.N. Altmann, F.J. Himpsel, Y.M. Koroteev, E.V. Chulkov, F.J. García de Abajo, J.E. Ortega, Phys. Rev. B 66 (2002) 245419.
[338] F. Baumberger, T. Greber, B. Delley, J. Osterwalder, Phys. Rev. Lett. 88 (2002) 237601.
[339] S. Agergaard, C. Søndergaard, H. Li, M.B. Nielsen, S.V. Hoffmann, Z. Li, P. Hofmann, New J. Phys. 3 (2001) 15.
[340] C.R. Ast, H. Höchst, Phys. Rev. Lett. 87 (2001) 177602.

[341] C.D. Spataru, M.A. Cazalilla, A. Rubio, L.X. Benedict, P.M. Echenique, S.L. Louie, Phys. Rev. Lett. 87 (2001) 246405.

[342] G. Moos, C. Gahl, R. Fasel, M. Wolf, T. Hertel, Phys. Rev. Lett. 87 (2001) 267402.

[343] J.E. Gayone, S.V. Hoffmann, Z. Li, P. Hofmann, Phys. Rev. Lett. 91 (2003) 127601.

[344] A.G. Borisov, A.K. Kazansky, J.P. Gauyacq, Phys. Rev. B 65 (2002) 205414.

[345] A.K. Kazansky, A.G. Borisov, J.P. Gauyacq, Surf. Sci. 544 (2003) 309.

[346] A. Fukui, H. Kasai, A. Okiji, Surf. Sci. 493 (2001) 671.

[347] A. Fukui, H. Kasai, H. Nakanishi, A. Okiji, J. Phys. Soc. Jpn. 70 (2001) 29.

[348] I. Nagy, J.I. Juaristi, P.M. Echenique, Phys. Rev. B 63 (2000) 035102.

[349] I. Nagy, M. Alducin, J.I. Juaristi, P.M. Echenique, Phys. Rev. B 64 (2001) 075101.

[350] J.I. Juaristi, M. Alducin, I. Nagy, J. Phys.: Condens. Matter 15 (2003) 7859.

[351] A. Georges, G. Kotliar, W. Krauth, M. Rozenberg, Rev. Mod. Phys. 68 (1996) 13.